

A time-series analysis software package (Acycle) for paleoclimate research and education

Mingsong Li¹, Linda Hinnov², and Lee Kump¹

¹Penn State University

²George Mason University

November 24, 2022

Abstract

A comprehensive, but simple-to-use software package for analysis of time-series has been developed for paleoclimate research and education. Acycle runs either in the MATLAB environment or as a stand-alone application on Windows and Macintosh OS X, and is available free of charge. Acycle provides prewhitening procedures with multiple options available to track or remove secular trends, and integrates various power spectral analysis approaches for detection and tracking of periodic signals. Acycle also provides a toolbox that evaluates astronomical signals in paleoclimate series, and estimates the most likely sedimentation rate by maximizing the correlation coefficient between power spectra of an astronomical solution and a paleoclimate series. Sedimentary noise models for sea-level variations are also included. Many of the functions are specific to cyclostratigraphy and astrochronology, and are not found in standard, statistical packages. For a demonstration, Acycle is applied to a paleoclimate series (iron content) from Core BH9/05 in the Paleogene Central Basin of Svalbard that samples the Paleocene-Eocene Thermal Maximum (PETM). Acycle detects significant astronomical forcing of the iron series and demonstrates a relatively stable sedimentation rate during and after the PETM event.

A time-series analysis software package (*Acycle*) for paleoclimate research and education



Mingsong Li¹, Linda Hinnov², Lee Kump¹
 mu450@psu.edu, lhinnov@gmu.edu, lrk4@psu.edu



1. Department of Geosciences, The Pennsylvania State University, University Park, Pennsylvania 16802, USA; 2. Department of Atmospheric, Oceanic and Earth Sciences, George Mason University, Fairfax, VA 22030, USA

1. Highlights

- We develop a software package for cyclostratigraphic research and education
- Many of the functions are powerful and specific to astrochronology
- It includes models of sedimentary noise and variable sedimentation rate estimation
- It is easy to use with a fully implemented graphical user interface (GUI)
- *Acycle* is open-source and available free of charge

2. Introduction

Three reasons motivated development of the *Acycle* time series analysis program.
 (1) to broaden and encourage the experience of time series analysis
 (2) to speed the process for time-consuming iterative procedures
 (3) to provide objective methods for astrochronology as reproducibility becomes a major challenge

This software package* integrates visualization and analysis of time-series and printing graphics using the MATLAB programming language.

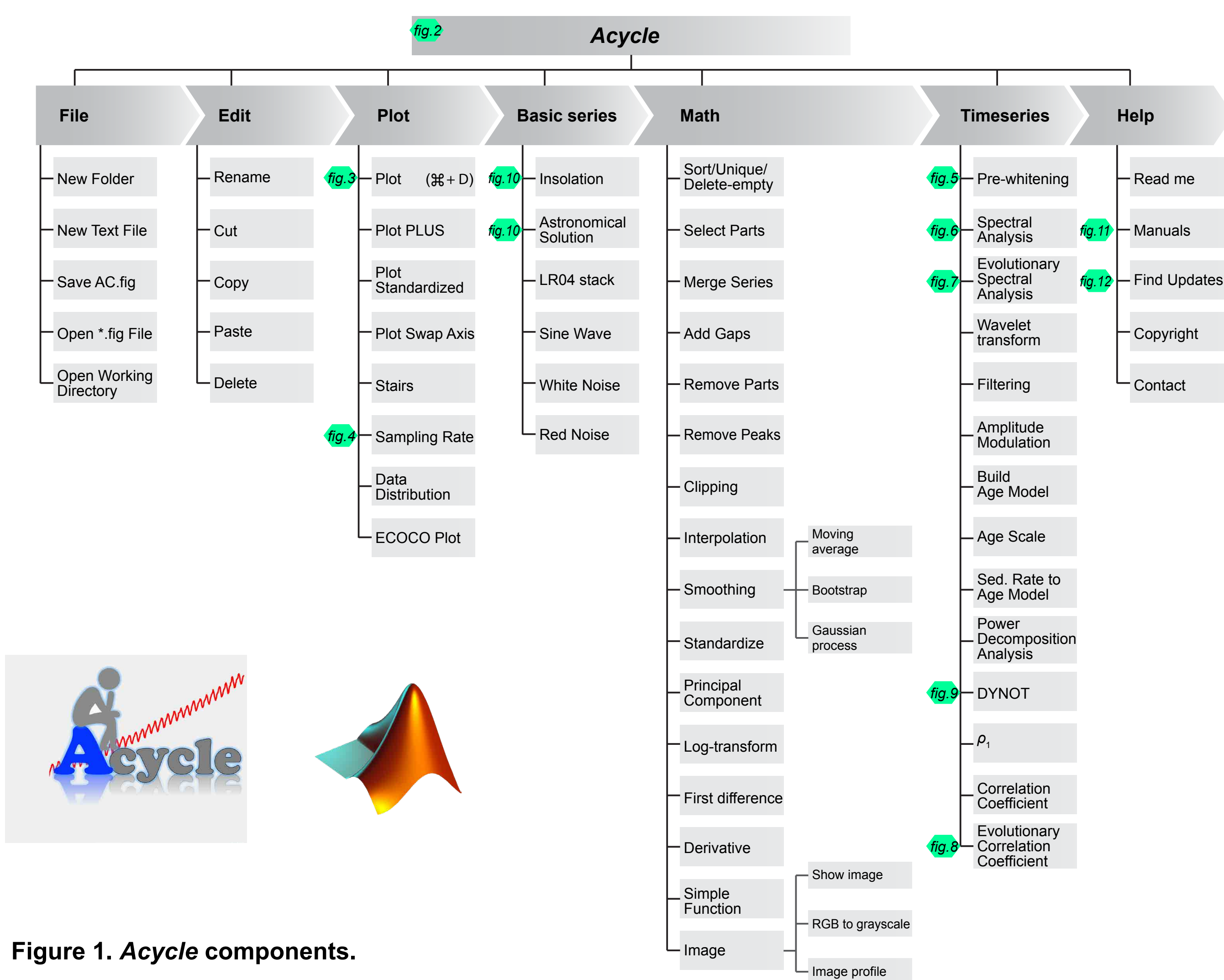


Figure 1. *Acycle* components.

3. The demonstration time series

The paleoclimate time series used to demonstrate *Acycle* is the XRF generated iron (Fe) content of Core BH9/05 from the Paleocene-Eocene Frysjaodden Basin of Spitsbergen, Svalbard. The full iron series of the Paleocene-Eocene Frysjaodden Formation was studied for the construction of an astrochronology for the global carbon cycle perturbation associated with the Paleocene-Eocene thermal maximum (PETM) (Cui et al., 2011).

* There is no specific requirement for hardware. Operating systems include Windows XP or later and Mac OS X 10.6 or later. This software is developed in MATLAB version 2015b. MATLAB is essential for the MATLAB version of the *Acycle* package. The size of *Acycle* is 47.5 M.

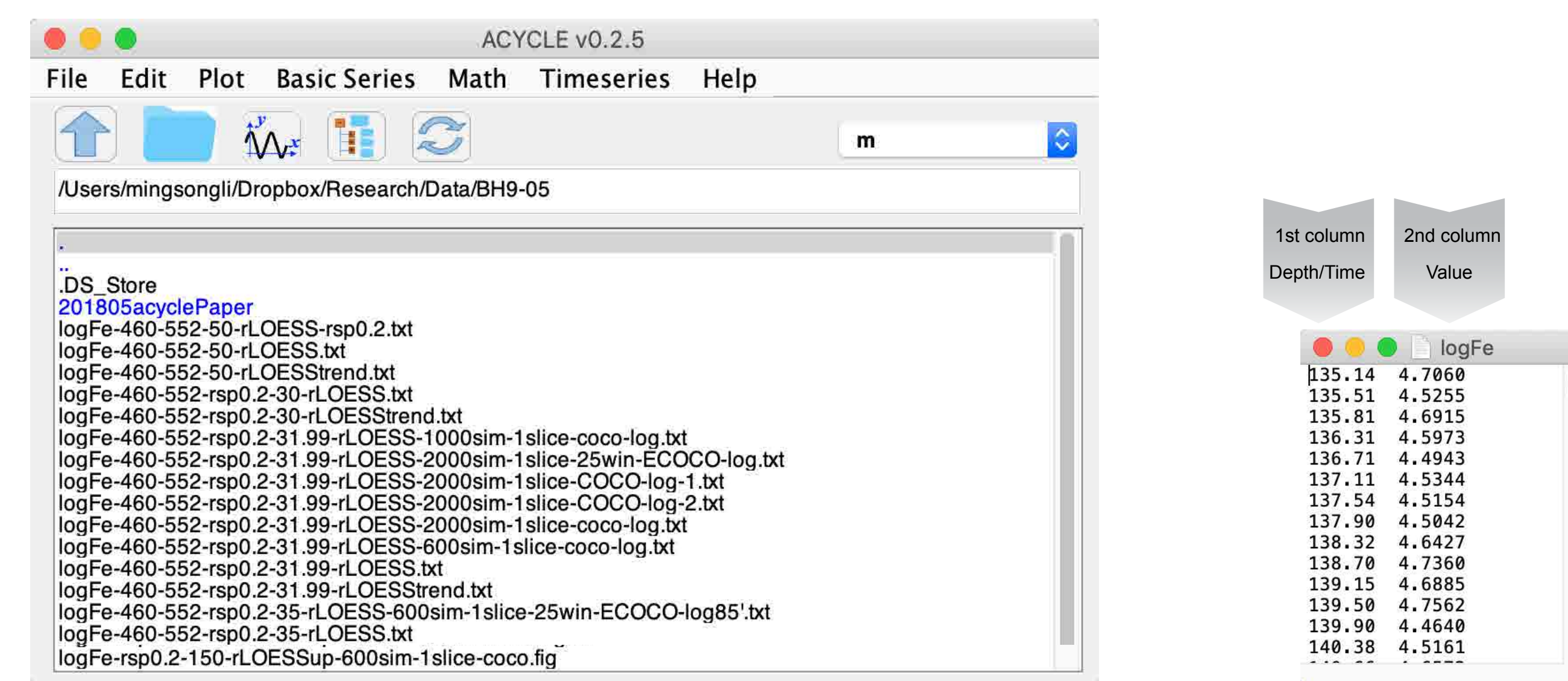


Figure 2. The *Acycle*. Left panel: GUI (see Fig. 4 for more details). Right panel: the data file format.

3.1. Data preparation

Acycle includes several toolboxes to facilitate the data preparation processes. The program allows users to sort data in ascending or descending order. Two or more values for the same time (or depth) may be averaged with the "Unique" function. Other useful tools include the moving average function and a first-difference function (Fig. 1).

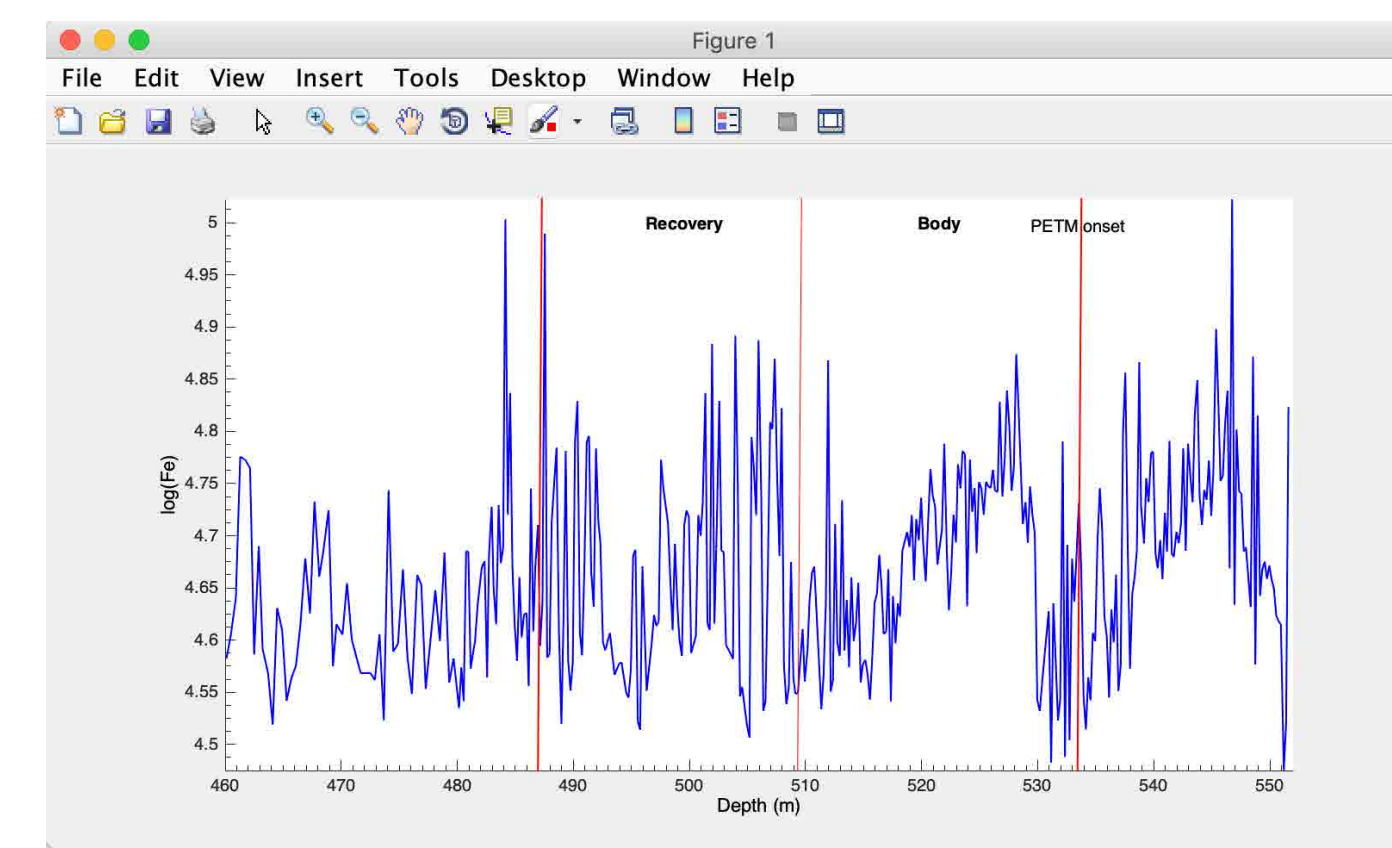


Figure 3. Log-transformed Fe paleoclimate series from 552 m to 460 m at Core BH9/05 in the Paleocene Central Basin of Svalbard. The Fe series is shown with PETM event onset and "body" interval of a prominent negative carbon isotope excursion, followed by a gradual recovery stages (Cui et al., 2011).

3.2. Sampling rate and interpolation

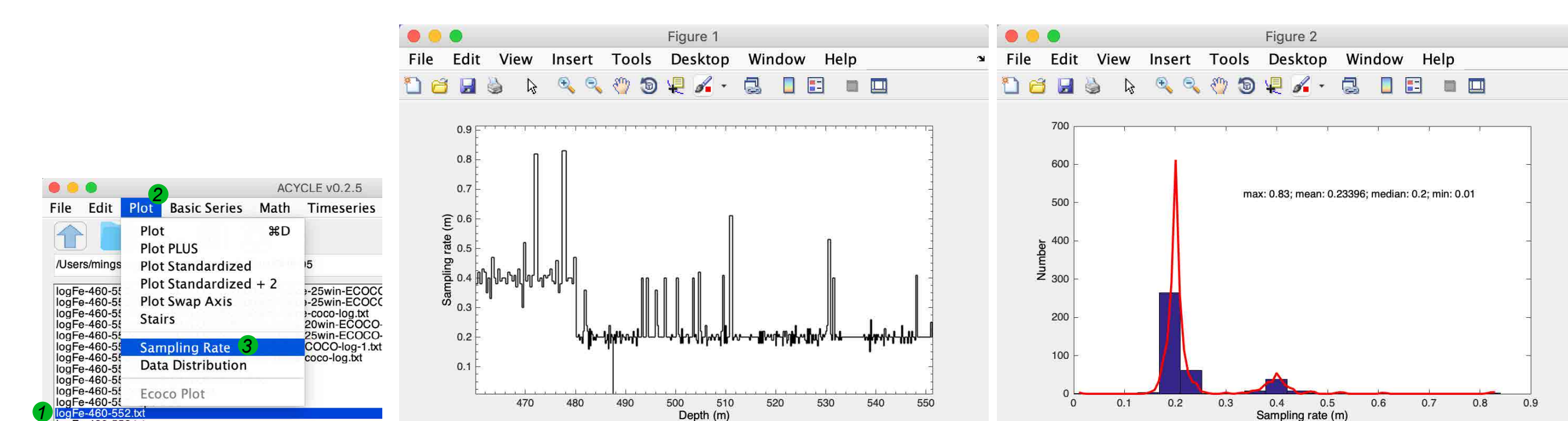


Figure 4. Left panel: *Acycle* GUI. Middle panel: Sampling rate of the Log(Fe) series at Core BH9/05 in the Paleocene Central Basin of Svalbard. Right panel: Histogram and the "kernel" fit of the sampling rates. Two peaks are centered at 0.2 and 0.4, respectively. These plots are generated using the "Sampling Rate" function in the "Plot" menu (Fig. 1).

3.3. Prewhitening

The log(Fe) series were pre-whitened using "Pre-whitening" function by subtracting a long-term trend.

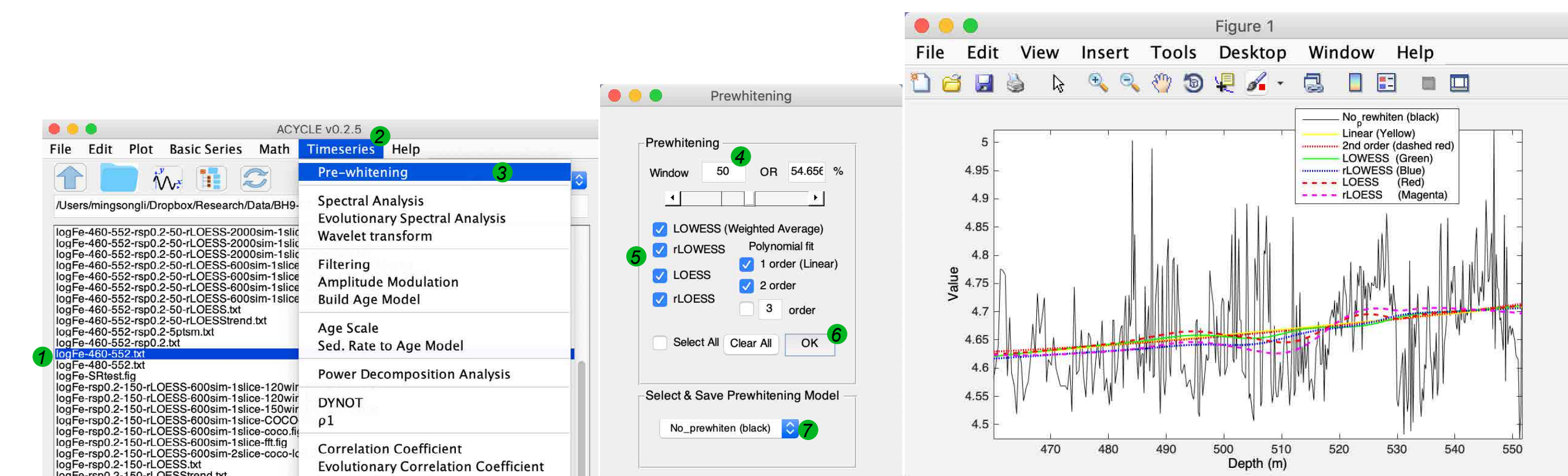


Figure 5. Left panel: *Acycle* GUI. Middle panel: The "Prewhitening" GUI. Right panel: The log(Fe) series at Core BH9/05 is shown with the linear trend, second order polynomial fit, and various 50-m secular trend using MatLab's "lowess", "rlowess", "loess", and "rloess" methods.

3.4. Power spectral analysis

Power spectra of the Log(Fe) series were examined for frequency peaks using the "Spectral Analysis" function.

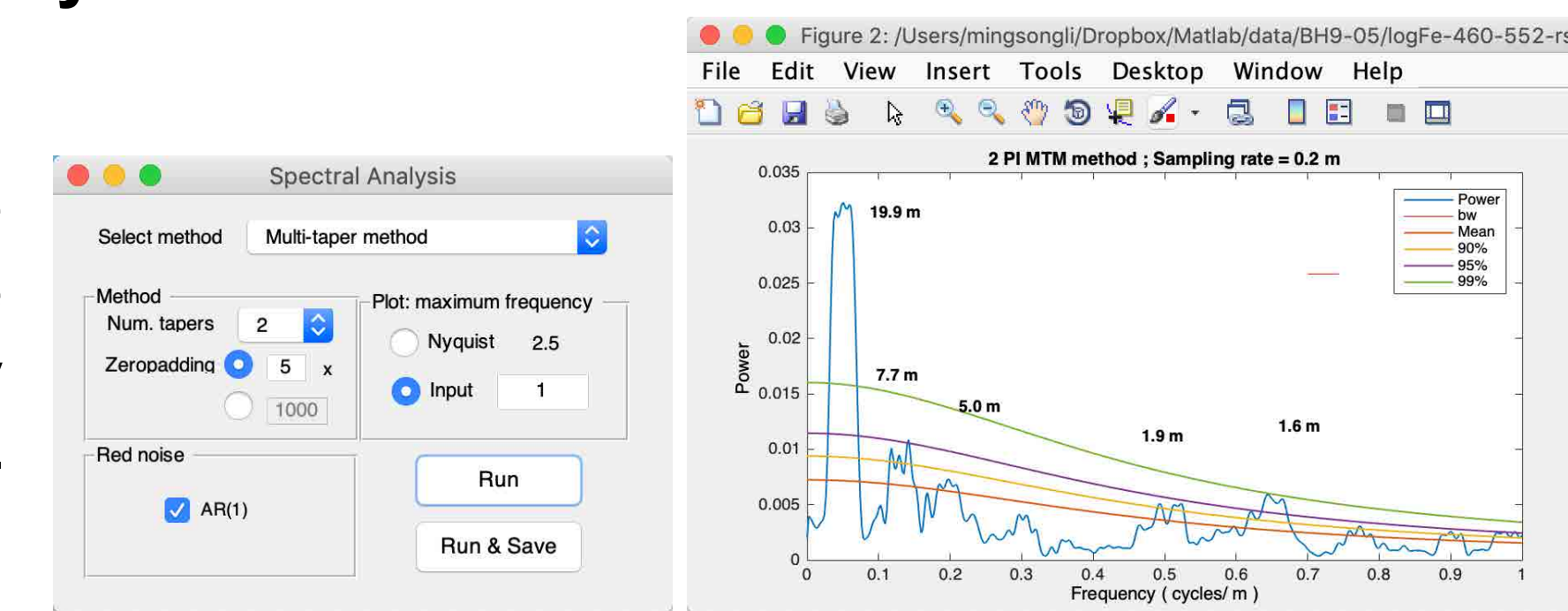


Figure 6. Left panel: The "Spectral Analysis" GUI. Right panel: 2π multitaper (MTM) power spectral analysis of the Log(Fe) series at Core BH9/05 after removing the 50 m "rloess" trend and interpolation of 0.2 m sampling rate. Cycle wavelengths are marked at top of the peaks. bw: bandwidth.

3.5. Evolutionary power spectral analysis

Evolutionary fast Fourier transform (FFT) spectrograms for inspecting stratigraphic frequencies and trends of the time series were computed using the "Evolutionary Spectral Analysis" function.

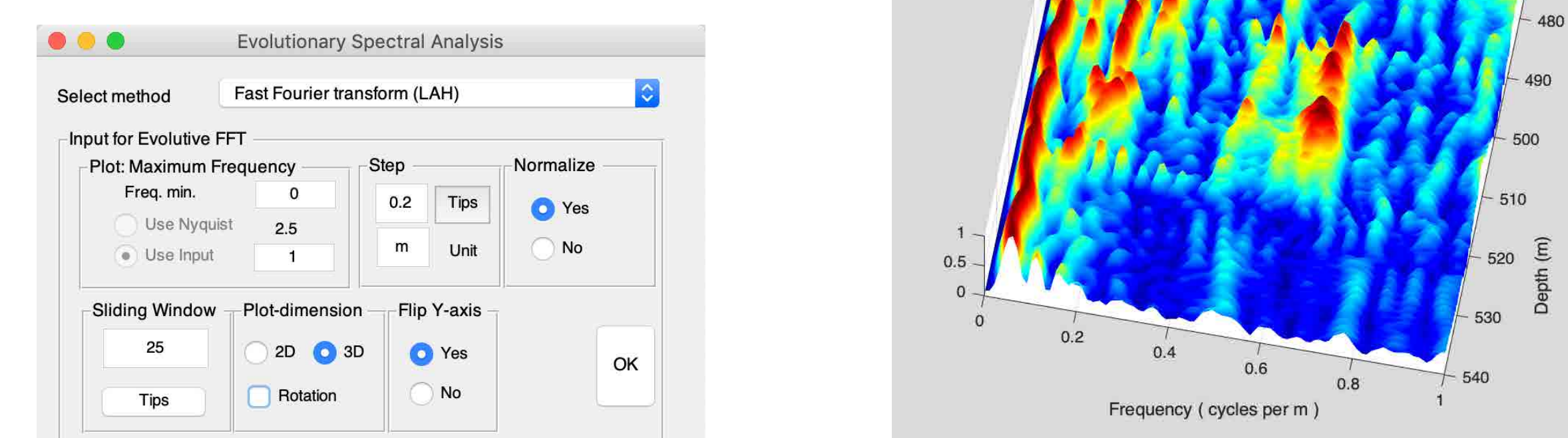


Figure 7. Left panel: Evolutionary Power Spectral Analysis GUI. Right panel: 3D evolutionary FFT spectrum of the log(Fe) series after removing 50 m "rloess" trend using a running window length of 25 m and a sliding step of 0.2 m.

3.6 Evolutionary correlation coefficient (ECOCO)

ECOCO (Li et al., 2018 *EPSL*) was calculated to track variable sedimentation rate and test astronomical origin of stratigraphic oscillations.

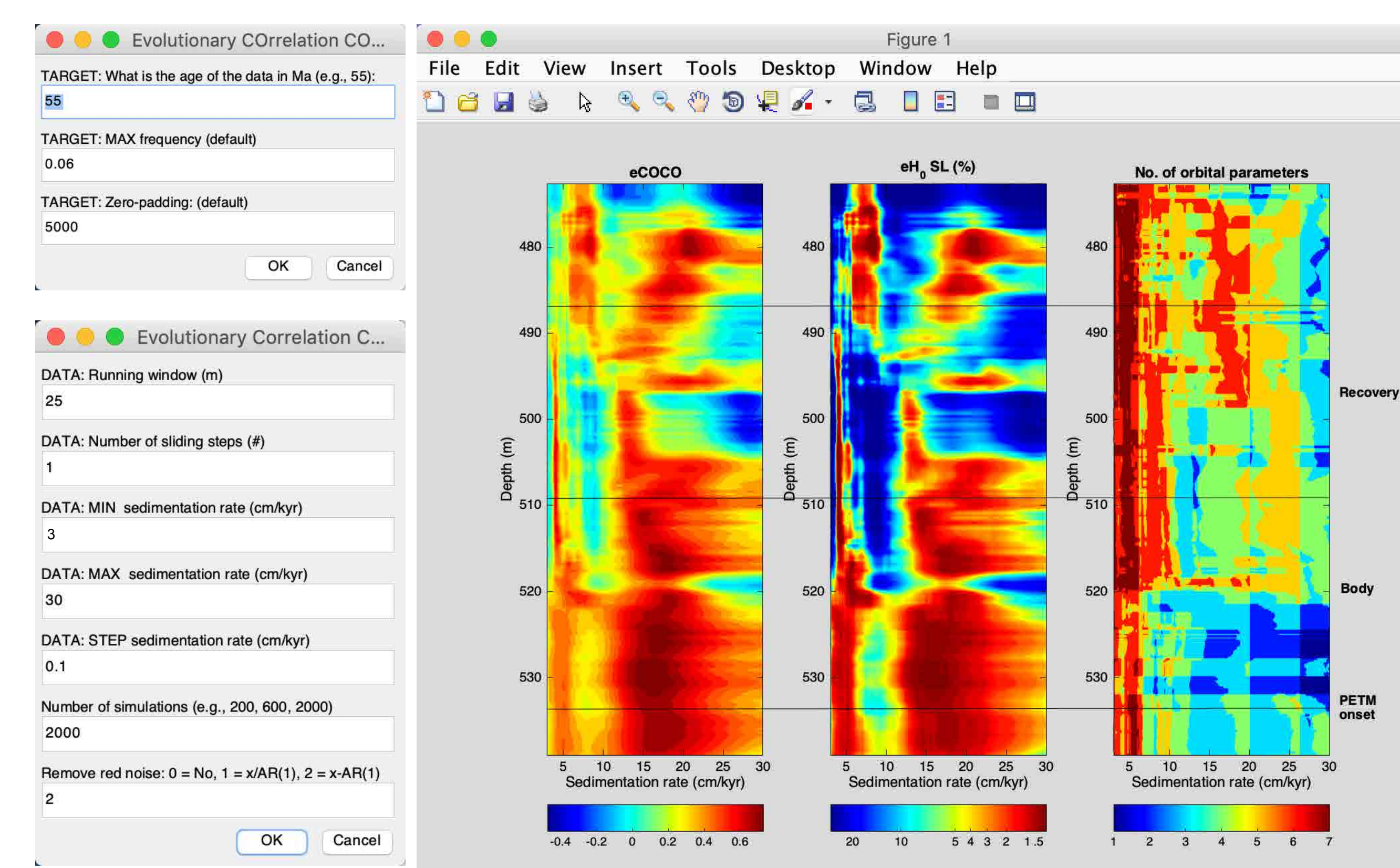


Figure 8. eCOCO GUI and eCOCO results of the Fe series at Core BH9/05. Left panel: Evolutionary correlation coefficient. Middle panel: Evolutionary H_0 significance level. Right panel: Evolutionary number of contributing astronomical parameters. The sliding window size is 25 m; the sliding window step is 0.2 m. All periodogram removes the AR(1) red noise model. The number of Monte Carlo simulations is 2000. Sedimentation rates range from 3 to 30 cm/kyr with a step of 0.1 cm/kyr.

3.7 Sedimentary noise model

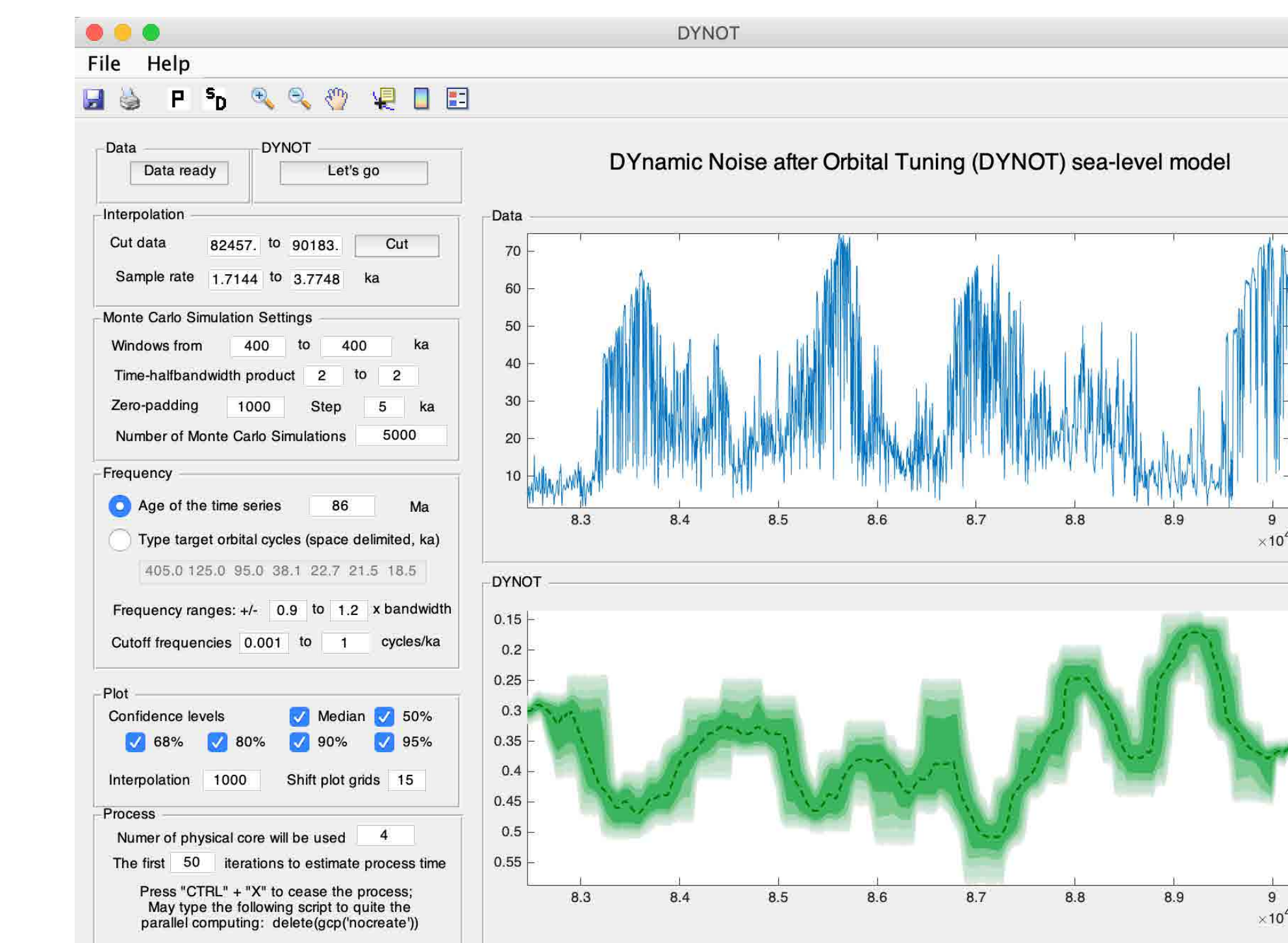


Figure 9. DYNOT GUI. (Data not discussed.)

A sedimentary noise model has been recently developed for the reconstruction of past sea-level changes from astronomically forced marginal marine stratigraphy (Li et al., 2018 *Nature Commun.*). The noise model includes two complementary approaches: lag-1 autocorrelation coefficient (ρ) and dynamic noise after orbital tuning (DYNOT). Both approaches are included in *Acycle*.

4. Toolboxes and supporting documents

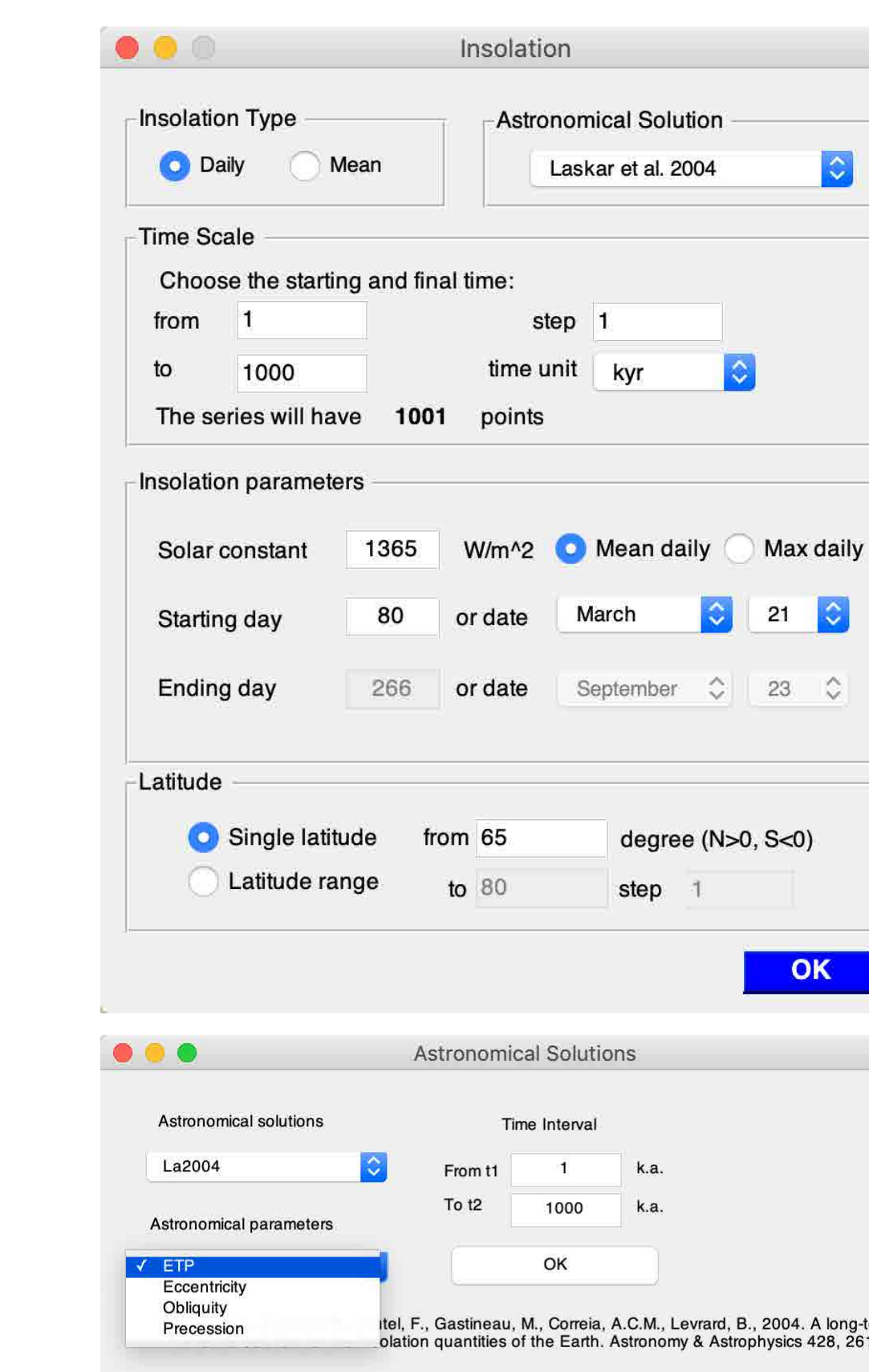


Figure 10. Solar insolation calculator (top panel) and a toolbox generating astronomical solutions (bottom panel).

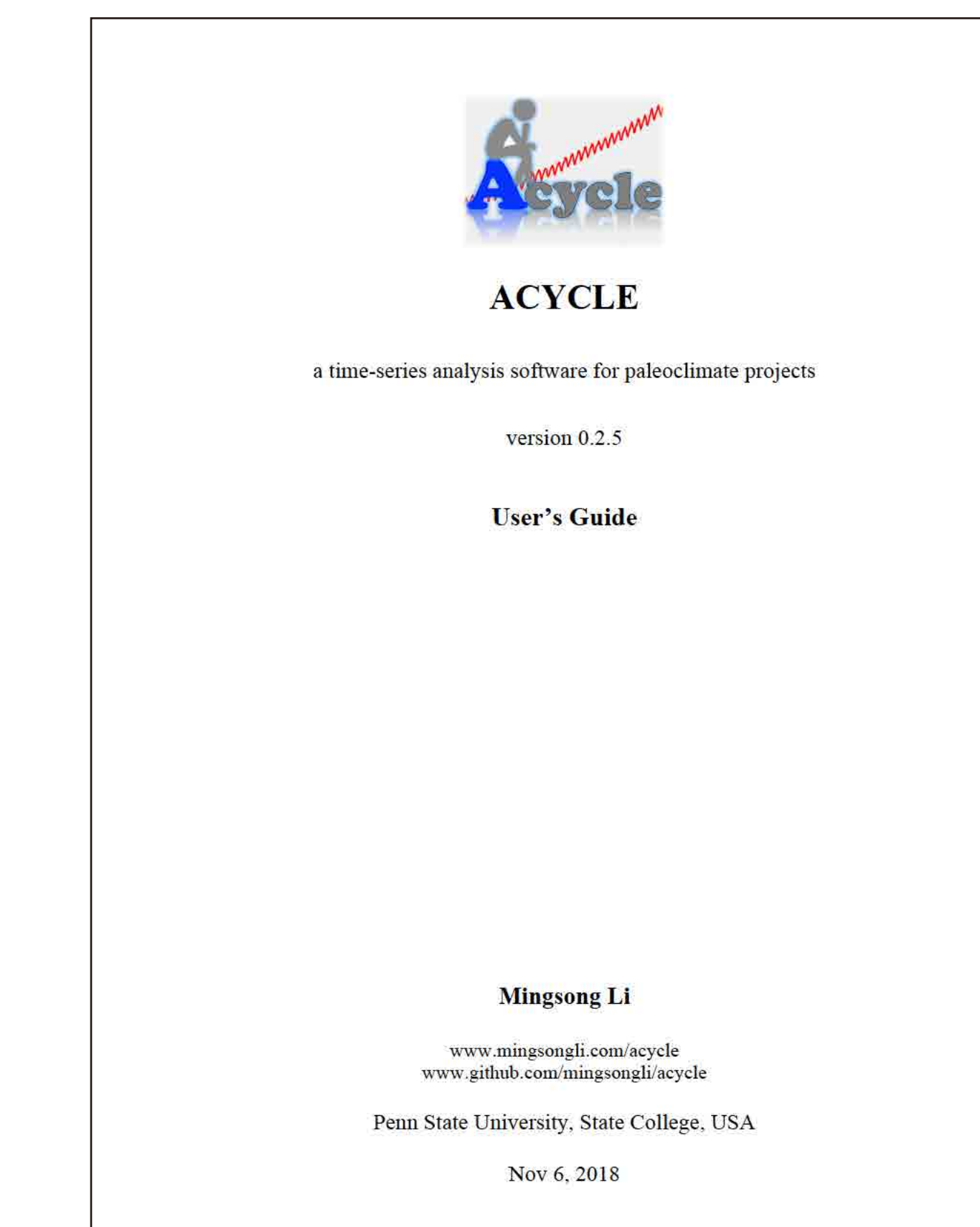


Figure 11. *Acycle* User's Guide. https://github.com/mingsongli/acycle/blob/master/doc/AC_User's_Guide.pdf

Website for *Acycle*:

mingsongli.com/acycle

Link to the code:

github.com/mingsongli/acycle

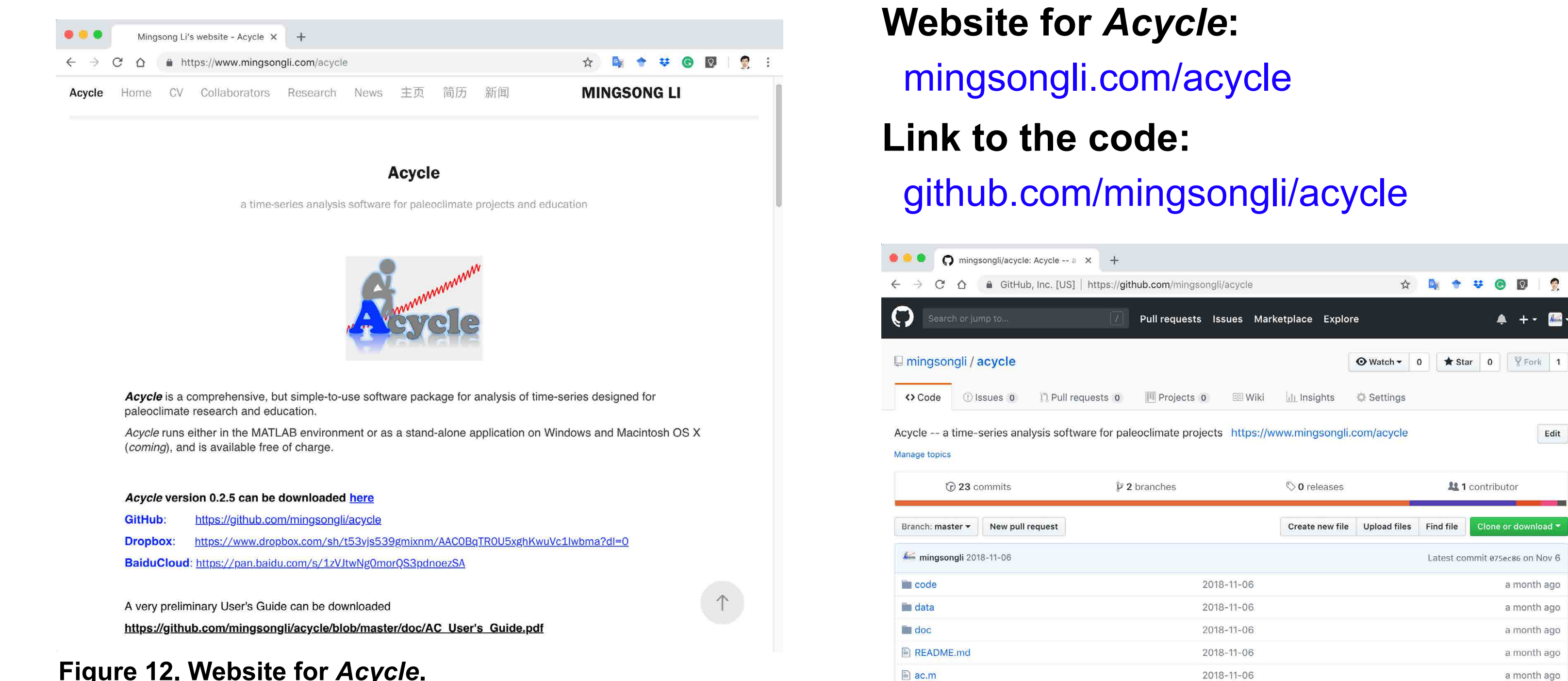


Figure 12. Website for *Acycle*.

ARTICLE

DOI: 10.1038/s41467-018-03454-y

OPEN

Sedimentary noise and sea levels linked to land-ocean water exchange and obliquity forcing

Mingsong Li ^{1,2,3}, Linda A. Hinnov^{2,1}, Chunju Huang^{1,4} & James G. Ogg^{5,1}

In ancient hothouses lacking ice sheets, the origins of large, million-year (myr)-scale sea-level oscillations remain a mystery, challenging current models of sea-level change. To address this mystery, we develop a sedimentary noise model for sea-level changes that simultaneously estimates geologic time and sea level from astronomically forced marginal marine stratigraphy. The noise model involves two complementary approaches: dynamic noise after orbital tuning (DYNOT) and lag-1 autocorrelation coefficient (ρ_1). Noise modeling of Lower Triassic marine slope stratigraphy in South China reveal evidence for global sea-level variations in the Early Triassic hothouse that are anti-phased with continental water storage variations in the Germanic Basin. This supports the hypothesis that long-period (1-2 myr) astronomically forced water mass exchange between land and ocean reservoirs is a missing link for reconciling geological records and models for sea-level change during non-glacial periods.

¹State Key Laboratory of Biogeology and Environmental Geology, School of Earth Sciences, China University of Geosciences, Wuhan 430074 Hubei, China. ²Department of Atmospheric, Oceanic, and Earth Sciences, George Mason University, Fairfax, Virginia 22030, USA. ³Department of Geosciences, Pennsylvania State University, University Park, PA 16802, USA. ⁴Laboratory of Critical Zone Evolution, School of Earth Sciences, China University of Geosciences, Wuhan 430074 Hubei, China. ⁵Department of Earth, Atmospheric and Planetary Sciences, Purdue University, West Lafayette, IN 47907, USA. Correspondence and requests for materials should be addressed to M.L. (email: limingsonglms@gmail.com) or to C.H. (email: huangcj@cug.edu.cn)

The Earth's stratigraphic record of past sea-level variations provides fundamental insights into the dynamics of present-day global sea-level change. Global sea-level variations result from changes in ocean basin capacity and seawater volume¹. Ocean basin capacity changes are dominated by low-frequency ($<10^{-6}$ per year) variations in sea-floor spreading rate². Higher frequency ($>10^{-6}$ per year) variations in seawater volume, i.e., eustasy are associated with the astronomically forced growth and decay of continental ice sheets that produce

high-amplitude eustatic changes (up to 200 m)². Other processes that pace seawater volume also occur at high-frequency but with low-amplitudes (5–10 m): variations in continental groundwater and lake storage, and thermal expansion and contraction of seawater^{3,4}. The causes of million-year (myr) scale, high-amplitude (>75 m) sea-level oscillations under hothouse conditions in the absence of continental ice sheets, e.g., during the early Triassic Period, remain unknown^{1,5–7}.

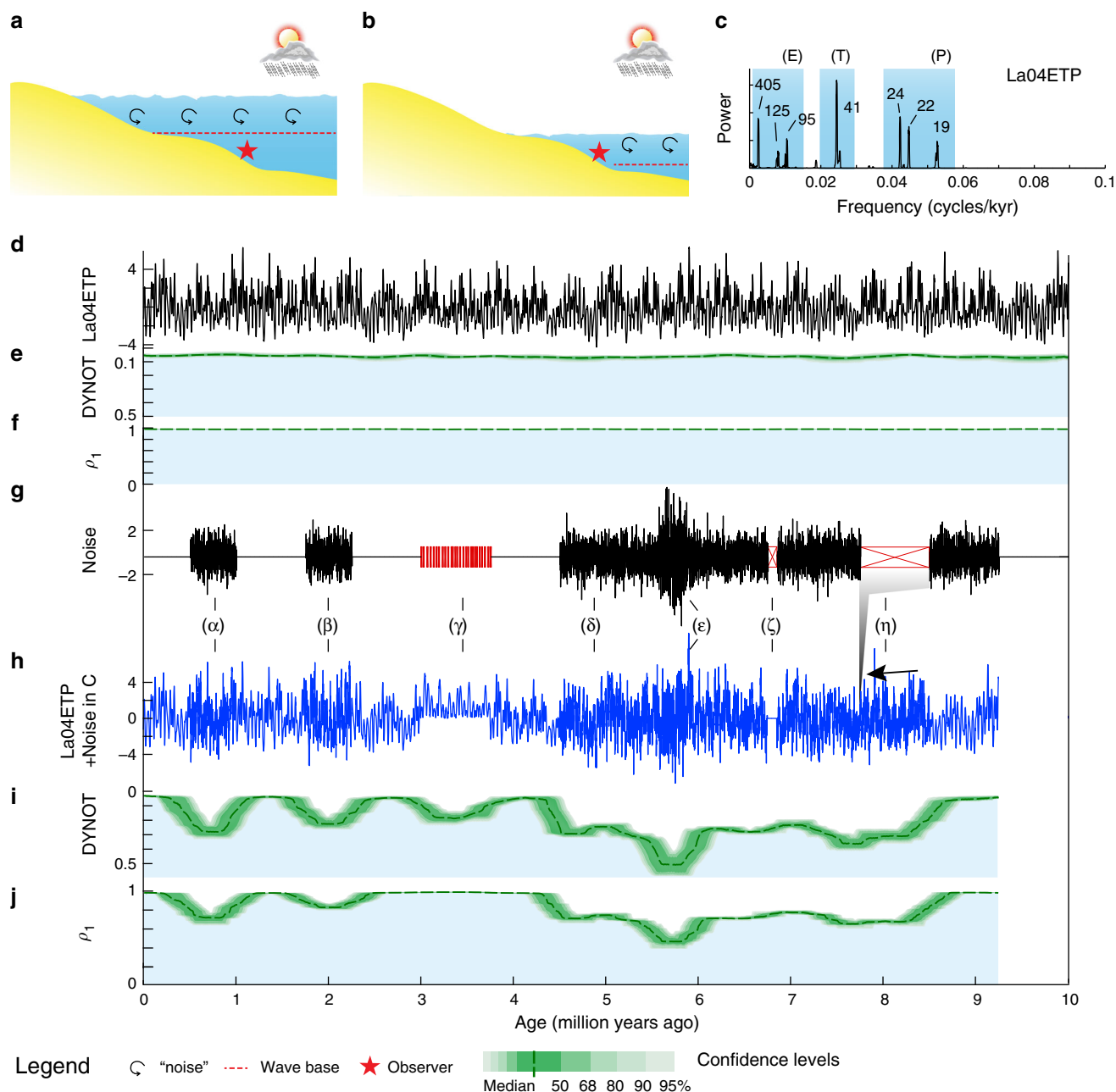


Fig. 1 Synthetic stratigraphic noise model of sea-level variations. **a** High sea-level and wave base with less water depth-related 'noise' at location of observer. **b** Low sea-level and wave base with more depth-related 'noise' and/or gaps at location of observer. **c** 2π multitaper power spectrum of Laskar2004 nominal astronomical solution (La04ETP, sum of standardized eccentricity (E), obliquity, or tilt (T), and precession (P)) of 0–10 Ma plotted against the united E, T and P bands (blue shading). **d** La04ETP from 0 to 10 Ma. **e** DYNOT model of La04ETP. **f** ρ_1 model of La04ETP. **g** Seven intervals with different types of noise (black) and gaps (red): (α) 500 kyr white Gaussian noise, (β) 500 kyr red noise with a $\rho_1 = 0.3$, (γ) multiple intermittent, brief gaps, (δ) 4.75-myrr white Gaussian noise with (ϵ) additional 500 kyr white Gaussian noise, (ζ) a 100 kyr gap, and (η) a 750-kyr gap. **h** Sum of La04ETP in **d** and the noise in **g**. ETP series expanded for 'unrecognized' gaps (γ) or zero during the 'recognized' gap (ζ) in **g** or missing during the 'unrecognized' gap (η). **i, j** DYNOT and ρ_1 models of the series in **h**, curve minima correspond to noise in **g** and multiple gaps (γ) are not revealed in **j**. Confidence levels are estimated by a Monte Carlo analysis with 5,000 iterations and a running window of 400 kyr

The geologic history of sea-level has been reconstructed from seawater volume proxies and marginal marine depositional sequences. Different proxies in sedimentary sections lead to diverse interpretations^{1,2}. The magnitude of sea-level estimates for the past 100 million years rely heavily on foraminiferal calcite oxygen isotopes ($\delta^{18}\text{O}$), which are influenced by temperature, evaporation and precipitation, and diagenesis². Sequence stratigraphy addresses stratal stacking patterns and changes thereof in a chronological framework⁸. Developments in sequence stratigraphy have greatly clarified the origin of genetically related sedimentary packages related to sea-level change, and have facilitated the reconstruction of sea level through geologic time^{2,5,6,9}. However, problems in sequence stratigraphy persist with confusing and even conflicting terminology, multiple depositional models, difficulties in recognition and correlation of sequence stratigraphic surfaces, and subjective assessment of sequence hierarchical order⁸. For example, sedimentary features representing sea-level fall in depositional sequences are often marked by unconformable surfaces in basin margins. Toward the basin center these unconformable surfaces may be subtle and even ‘conformable’ thus difficult or even impossible to identify. These problems together with limited accuracy in the geologic timescale hinder the reconstruction of global sea-level and understanding the origins of sea-level change.

Here we present stratigraphic evidence that elucidates the causes of high frequency, high-amplitude sea-level changes that occurred during the ice-free Early Triassic hothouse. We develop a dynamic noise after orbital tuning, or DYNOT model for the recognition of sea-level variations based on the dynamic non-orbital signal in climate proxy records after subtracting orbital, i.e., astronomically forced climate signal. The DYNOT model is supplemented by a second, independent lag-1 autocorrelation coefficient, or ρ_1 model, which forms the basis of a well-established statistical method for red noise estimation of time series^{10–12}. DYNOT and ρ_1 modeling applied to a marine slope gamma ray record from the past 1.4 myr correlate with sea-level changes reconstructed from benthic foraminiferal $\delta^{18}\text{O}$. This verification indicates that the sedimentary noise model is a useful method for sea-level reconstruction. These two approaches for modeling sedimentary noise applied together with an astronomical timescale for the Early Triassic^{13,14} enable correlation among time series of global sea-level, continental water storage and astronomical climate forcing.

Results

Modeling dynamic sedimentary noise. Climate and sea-level proxy variations consist of long-term trends, 10^6 year-scale orbital (eccentricity and inclination) modulation cycles, 10^3 to 10^5 year-scale astronomical (orbital eccentricity, obliquity and precession) cycles, 10^0 to 10^3 year-scale climate variability, and abrupt geological events. Importantly, an abundance of ‘noise’ is also embedded in the originating climate signals. Sources of noise that affect climate and sea-level proxies can be classified as follows: water-depth related noise such as storms, tides, bioturbation, and unsteady depositional rate; proxy-related noise including proxy sensitivity, measurement error, non-linear climate response, and dating error¹¹; and other factors such as tectonics, volcanism and post-depositional diagenesis¹⁵. Among these, measurement error and proxy sensitivity can be assessed from replicate proxy data sampled across a single stratigraphic interval, and dating errors and depositional rate by generating an age model, e.g., astrochronology. Variations in the water-depth related noise at a fixed location in the marginal marine environment are related to relative sea-level changes (Fig. 1). When sea level is relatively high, water-depth related noise at a fixed slope

location in the marginal marine environment is weaker than the noise in a time of relatively low sea-level, and vice versa.

DYNOT sea-level model. The DYNOT model is designed to measure noise in climate and sea-level proxies. If proxy-related noise and other factors (see above) are minor, the variance of the noise can be an indicator for relative sea-level changes. For a 10^3 to 10^6 year-band in the power spectra of proxy series, we evaluate the ratio of non-orbital signal variance to the total variance, which is calculated along a sliding time window (Methods). When sea-level is relatively high, the DYNOT ratio is weaker than the ratio in a time of relatively low sea-level, and vice versa.

ρ_1 sea-level model. Climate change tends to incorporate previous values over a range of timescales; this is termed autocorrelation or persistence^{10,11}. The simplest and most widely adopted persistence model is based on the lag-1 autocorrelation coefficient^{10,11,16}. The ρ_1 model is tested as a second, independent noise indicator for relative sea-level change (Methods). As demonstrated below, increased noise leads to a decreased ρ_1 value, and vice versa.

Applications and restrictions. The sedimentary noise model is expected to apply to proxies that are sensitive to water-depth-related noise. In this application, the model is assumed to be valid for slope and basin environments at water depths of several meters to several hundred meters that are near or just below storm-wave base, where storms, tides, bioturbation, and unsteady depositional rate are expected to exert measurable influence (noise) in sedimentary records.

Other factors may contribute to sedimentary noise related to sea-level change. For example, basin-scale tectonic activity may affect 10^6 year-scale relative sea-level changes². Short-term tectonic activity such as earthquake-induced downslope movements may affect sea-level change by imposing sudden (and random) jumps or spikes leading to elevated noise at all frequencies. Non-linear responses of sea-level change to orbital forcing may generate spectral sidebands or combination tones¹⁷ that cannot be removed by the model. Simulation of non-linear accumulation and bioturbation effects on precession-forced basinal carbonate cycles demonstrate that variance can be transferred from the precession into the eccentricity band¹⁸, generating ‘redder’, i.e., higher ρ_1 values. Sub-Milankovitch scale climate oscillations captured in very high-resolution proxy records will not be removed by DYNOT modeling. Geological events such as volcanism may lead to hydrological changes and proxy records with extended perturbations with increased low-frequency non-orbital noise, thus impacting both approaches. Changes in the Earth’s climate state may generate additional noise and affect the climate persistence, contributing to noise in deep ocean records¹⁰. However, the model verification study presented below does not show evidence of this type of influence in a Quaternary marginal marine environment. Interpolation of irregularly spaced data can also affect the model, for example, upsampling to increase sampling rate leads to artificially high ρ_1 values (Methods). Finally, post-depositional diagenesis of calcareous bedding may enhance and/or distort orbital-scale variations. These factors are discussed in detail in the Supplementary Note 1. DYNOT and ρ_1 modeling of sedimentary noise is nonetheless powerful for sea-level reconstruction as demonstrated below.

Testing the sedimentary noise model. The efficacy of DYNOT and ρ_1 modeling is demonstrated on the La2004 astronomical solution¹⁹ from 0 to 10 Ma with added synthetic noise and gaps (Fig. 1). The added noise simulates different environmental

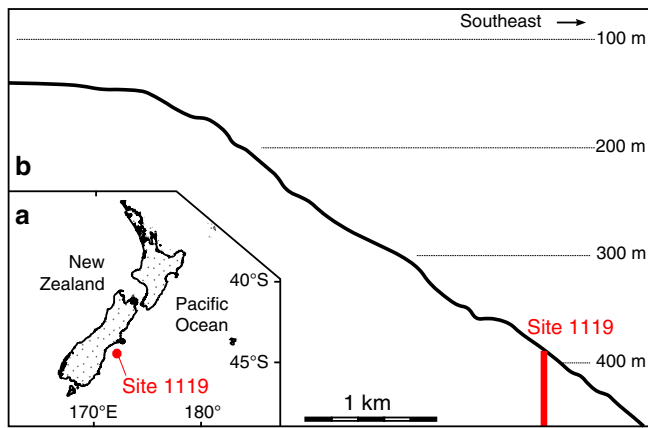


Fig. 2 Locality maps. **a** Locality map of ODP Site 1119²³. **b** Profile through Site 1119 showing present-day water depth²⁰

processes under a variety of sea-level conditions. Strong noise (low sea level) leads to elevated DYNOT and decreased ρ_1 values, and vice versa. Intermittent brief (10^3 year-scale or shorter) gaps, such as intervals undergoing erosion or with no deposition due to repeated exposure that are hard to recognize, lead to distortion of individual astronomical cycles and increased DYNOT values. These brief gaps, if not accompanied by noise, may not be detected in the ρ_1 model. Long-lived (10^5 year scale or longer) gaps simulating unrecognized sedimentary hiatus lead to a slight increase in DYNOT and decrease in ρ_1 ; the DYNOT and ρ_1 models cannot be used to identify hidden gaps (Fig. 1). Long-lived recognized gaps, such as those in drill cores, lead to an increase in DYNOT, decrease in ρ_1 , and even a discontinuity (Supplementary Fig. 1). Brief single recognized gaps are difficult to detect, hindering their recognition, but this also indicates that the sedimentary noise model tolerates single brief gaps.

Model verification in the late Quaternary. A sedimentary record that can provide an unambiguous verification of the sedimentary noise model has the following characteristics: contemporaneous sea-level reference data; the record is from a marginal-marine environment at a water-depth of several hundred meters (near storm-wave base); the record experienced minimal tectonic and volcanic activity with no gravity flows; high-resolution paleoclimate and sea-level proxies are accessible; and a reliable chronology has been established.

The record of global sea-level change over the past 1.4 million years² provides an opportunity to verify the DYNOT and ρ_1 models of sedimentary noise. Ocean Drilling Program (ODP) Site 1119 (Fig. 2) is located 96 km east of South Island in the Canterbury Basin, New Zealand, in 393 m water depth on the upper continental slope and 5 km seaward of the edge of the shelf²⁰. The minimum water depth of the site was ~250 m during Marine Isotope Stage 2²¹, which leads to an inference that paleoclimate proxy data at that site are susceptible to increased environmental noise during times of low sea level. The lithology at the site is strongly influenced by the terrigenous input from New Zealand. The drill core penetrated 514 m of silts and silty clays (glacial deposits) punctuated by muds and episodic 0.02–1.2 m thick terrigenous sands (interglacial deposits)²². Tectonic and volcanic activity was low in the Canterbury Basin over the past several million years²⁰; the sediments are devoid of diagenesis, and evidence for gravity flows is rare²².

At Site 1119 the gamma ray (GR) log has been interpreted as a proxy of fluctuations in clay content corresponding to variations in the rate of supply of glacial ‘rock flour’ from a waxing and

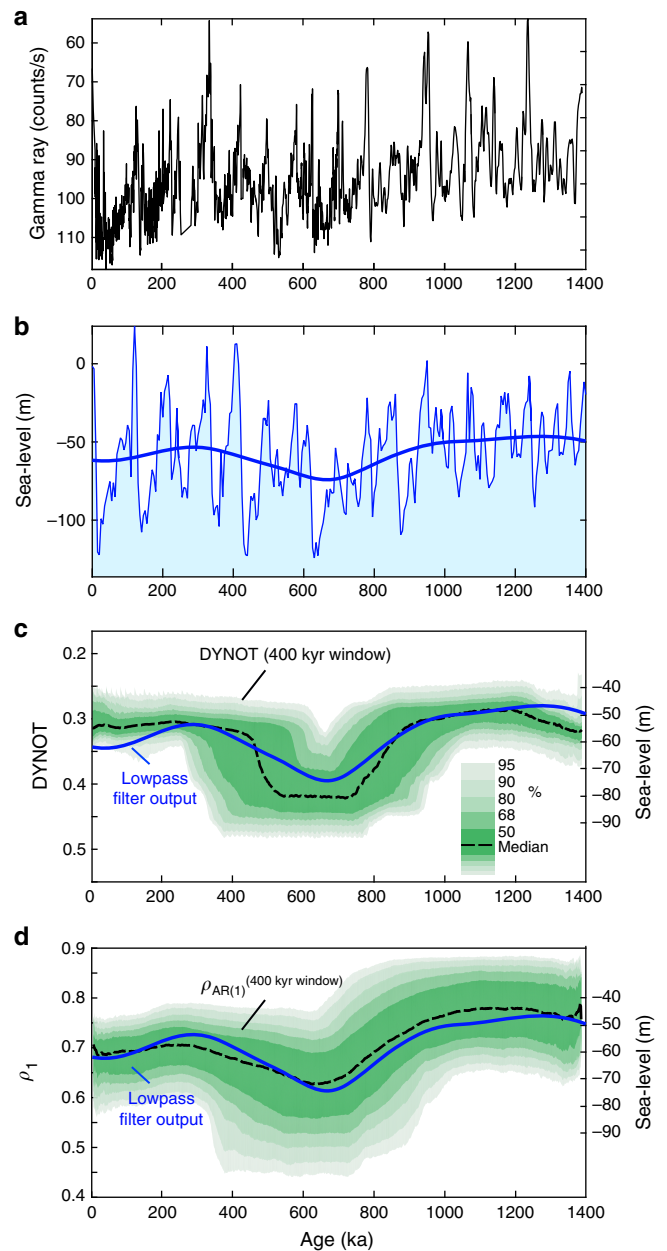


Fig. 3 Testing sedimentary noise models on the gamma ray log from ODP Site 1119. **a** Fine-tuned gamma ray series, with one outlier removed (see Supplementary Fig. 3). **b** Sea-level changes are estimated from benthic foraminiferal $\delta^{18}\text{O}$ ² shown with lowpass Gaussian filter output of sea-level changes (thick blue; cutoff frequency is $1/(400 \text{ kyr})$ using ‘gaussfilter.m’⁵⁰). **c** DYNOT models of interpolated, tuned time series in **a** using random sample rates of 0.22–2.04 kyr (Methods) with a running window of 400 kyr. **d** ρ_1 model using random sample rates of 2.04–3.06 kyr (Methods) with a running window of 400 kyr. The DYNOT and ρ_1 results are shown with lowpass filter output of sea-level changes in **b** (solid blue). Confidence intervals are estimated by Monte Carlo analysis with 5000 iterations

waning South Island ice cap²³. The age model is based on radiocarbon dates for the past 39 ka; prior to 39 ka, 38 selected GR peaks have been correlated with tuned $\delta^{18}\text{O}$ records from ODP Sites 758 and 1143 to provide a 3.9-Myr-long time scale^{21,23}. The mean chronological uncertainty is less than 22 kyr over 0–1.4 Ma²⁴. To reduce the dating error, fine-tuned GR log using

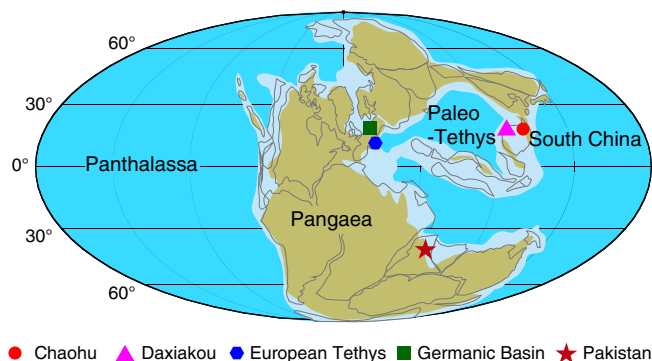


Fig. 4 Early Triassic global paleogeographic map. The map is modified from Christopher Scotese (<http://www.scotese.com>) with localities of data shown in Figs. 5 and 6

astrochronology (Methods) is employed for the noise model verification.

We apply the noise model on the Site 1119 GR from 0–1.4 Ma (Fig. 3, Supplementary Figs. 2–7). DYNOT and ρ_1 models with a 400 kyr running window correlate well with a lowpass-filtered sea-level curve (Fig. 3). The noise model of the original GR log is also presented in the Supplementary Fig. 5. Fine-tuning the GR series leads to little change in the DYNOT and ρ_1 models (Supplementary Figs. 4–5), indicating that both approaches tolerate dating errors when using a relatively large 400 kyr running window. Dynamic noise in the global sea-level curve may also be linked to changes in the Earth’s climate state as discussed above. DYNOT and ρ_1 spectra of the global sea-level curve using a 400 kyr running window show little similarity between sea-level change and dynamic noise in the sea-level curve itself (Supplementary Fig. 6), which suggests that the sources of noise at Site 1119 are different from those in global sea-level changes. For multi-million-year-long deep-time datasets from marginal marine environments, DYNOT and ρ_1 models can be used to provide an independent, high-resolution sea-level curve, and is demonstrated for the Early Triassic as follows.

Model application to the Early Triassic. Two marine sections from the South China Plate margin at Chaohu and Daxiakou (Fig. 4) provide a unique opportunity to assess a high-precision time scale conjoined with Early Triassic sea-level variations using the sedimentary noise model. The Upper Permian to Lower Triassic deep-marine successions at Chaohu and Daxiakou consist of cyclically bedded marine claystone and limestone. Sediments at both Chaohu and Daxiakou sections deposited in an offshore slope to basin setting in the early Early Triassic and the proximal ramp to outer shelf conditions in the late Early Triassic^{13,25}.

GR of these sedimentary rocks is affected by terrestrial clays and has been used as a proxy for continental runoff forced by climate change (Methods). The GR datasets from Chaohu and Daxiakou sections have been tuned to interpreted 405 kyr cycles¹³. A recently astronomically tuned magnetostratigraphy between South China and Germany provides an integrated time scale^{13,14} to precisely correlate the reconstructed sea-level oscillations from China with European sequence stratigraphy (Fig. 5).

At Chaohu, DYNOT and ρ_1 show similar patterns suggesting that significantly enhanced noise occurred in the late Changhsingian, middle Induan, earliest Smithian, late Smithian, early Spathian, and latest Spathian (Fig. 6d, e). The Daxiakou section is currently 700 km distant from Chaohu (similar distance in the Early Triassic), correlates to Chaohu section (compare Fig. 6b, c

for Daxiakou and Fig. 6d, e for Chaohu). Contributing factors to the sedimentary noise model of the studied sections are provided in Supplementary Note 1 and Supplementary Figs. 11–12. This sedimentary noise modeling sets a new framework for Early Triassic sea levels in South China.

The sea-level variations interpreted from the sedimentary noise models at Chaohu and Daxiakou are supported by field observations at the outcrop. For example, the sequence boundaries O11, O12, and O13 in Fig. 6g correspond to elevated noise values at Chaohu and Daxiakou. These sequence boundaries are consistent with major lithologic changes from thin-bedded clay-rich sediments to medium-thick carbonate beds (Supplementary Fig. 8) indicating sea-level falls during clay-rich, basinal and proximal ramp conditions. Moreover, sedimentary structures indicative of high-energy and shallow water conditions, e.g., ripples and cross stratification²⁵, correlate with increased noise levels indicative of shallow sea levels at Chaohu (Supplementary Figs. 9–10).

Early Triassic sequence boundaries are typically presented in relative time or with ages estimated by correlation to the geologic time scale^{5,7,9,26}. Here, DYNOT and ρ_1 modeling provides a high-resolution time frame for sea-level changes estimated directly from stratigraphy. A set of major sea-level falls during the Early Triassic have been proposed for the Boreal and Tethyan provinces in the European basins, Arctic Canada and other regions^{6,9,26}. The amplitudes of these sea-level falls have been interpreted to be as much as 75 m^{5,9} (although some estimates are more subdued⁷; see Supplementary Note 2 and Supplementary Fig. 13). The sedimentary noise models of sea-level change in South China correlate with these major eustatic changes (compare Fig. 6b–f), establishing the global nature and synchronicity of these 10⁶-year scale eustatic events.

Hypothesis of aquifer eustasy. In super-greenhouses or hot-houses with no known ice sheets, as during the Early Triassic or Late Cretaceous, ice-based models (i.e., ice sheet growth and decay) cannot explain high-amplitude sea-level variations. An alternative model that 10³ to 10⁶ year scale variations in continental water storage significantly changes the land–ocean water mass balance, led to the hypothesis of ‘groundwater-driven eustasy’, termed ‘aquifer eustasy’^{3,27–31} or ‘limno-eustasy’^{32,33}. However, this hypothesis currently has three complications: underestimation of continental water storage and its confusion with minor lake and river water volume with respect to sea-level change equivalent (<1 m)^{2,30,33}; lack of direct evidence of continental water storage from the geological record; and poorly understood mechanisms and timescales of aquifer eustasy^{27,28,31,32,34}.

However, our understanding of the volume of continental water storage improved substantially with the ‘pore space’ model of Hay and Leslie³⁰. According to this model, pore volume in Triassic terrestrial systems, if filled to capacity with meteoric water, could lower sea-level by more than 100 m after isostatic adjustment³⁰. During the Late Cretaceous terrestrial pore space was equivalent to a global sea-level change of 200 m³⁰. Compilations suggest that the present-day volume of groundwater storage is equivalent to a sea-level differential of ~320 m³⁵ to 330 ± 41 m³⁶. Even if only a proportion of a corresponding water volume contributes to sea-level change, this change is significant^{28,29,32,33}.

Based on the hypothesis of aquifer eustasy, there should be a positive correlation between filled continental aquifers (high groundwater tables) and relatively high lake levels^{32,33}. Consequently, non-marine sequences in the Cretaceous and Late Triassic have been proposed as a proxy for lake levels and

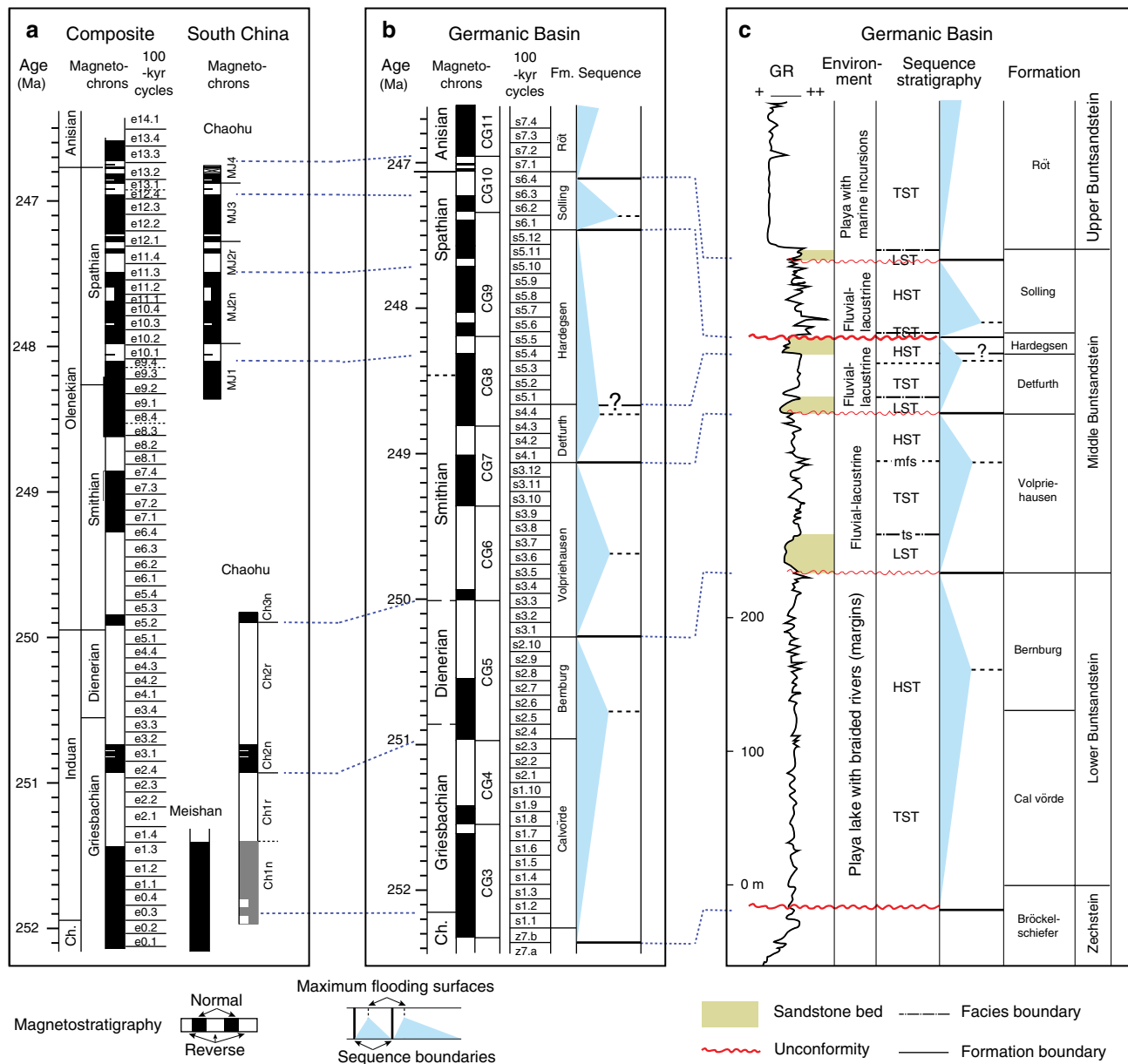


Fig. 5 Sequence stratigraphy of the Germanic Basin. **a** 405 kyr cycle-calibrated magnetostratigraphy in South China¹³. **b** 100 kyr cycle calibrated magnetostratigraphy of the Germanic Basin^{37,69,70} shown with calibrated Germanic sequences in **c**. **c** Sequence stratigraphy of the Germanic Basin^{40,41} plotted in the stratigraphic domain. Dashed blue lines indicate formation boundaries in the Germanic Basin. LST: lowstand systems tract. TST: transgressive systems tract. HST: highstand systems tract. ts: transgressive surface. Mfs: maximum flooding surface. Fm.: formation

continental aquifers, which moreover are out-of-phase with sea-level variations^{32,33}. However, correlations of terrestrial and marine sequences in the Cretaceous and Late Triassic that support the aquifer eustasy hypothesis³², while enlightening, suffer from a lack of reliable chronology. In this respect, the detailed astrochronology and magnetostratigraphy of the Early Triassic in South China and Germanic Basin^{13,37} provide a robust time framework for correlating non-marine sequences and global sea levels (Fig. 5).

Evidence for Triassic land–ocean water balance dynamics. The Germanic Basin is a restricted basin with a center in northern Germany during the Early Triassic^{38–40}. Groundwater tables and thus water storage variations can be inferred from sequences deposited in the lacustrine and fluvial environments of the basin.

A regressive tendency of the uppermost marginal-marine Zechstein (latest Permian) continued into the Lower Buntsandstein that was deposited in a playa-lake setting⁴⁰. A shale-rich interval in the middle of the Bernburg Formation represents a maximum flooding surface⁴¹. A regional unconformity at the base of the Volpriehausen Formation has been suggested as a sequence boundary^{37,40,41}. Fining-upward interbedded sandstones and shales and coarsening-upward strata of the Volpriehausen Formation were deposited in fluvial and lacustrine environments^{40,41}. The overlying Detfurth and Hardegsen formations were also deposited in fluvial to lacustrine settings⁴¹. The widely distributed ‘Hardegsen Sandstone’ at the base of the Hardegsen Formation is marked by an abrupt change in lithology^{37,40}, which indicates a possible sequence boundary. The succeeding Solling Formation is characterized by coarse-grained fluvial sandstones, lacustrine shales, and fluvial sandstones⁴⁰. The overlying Anisian

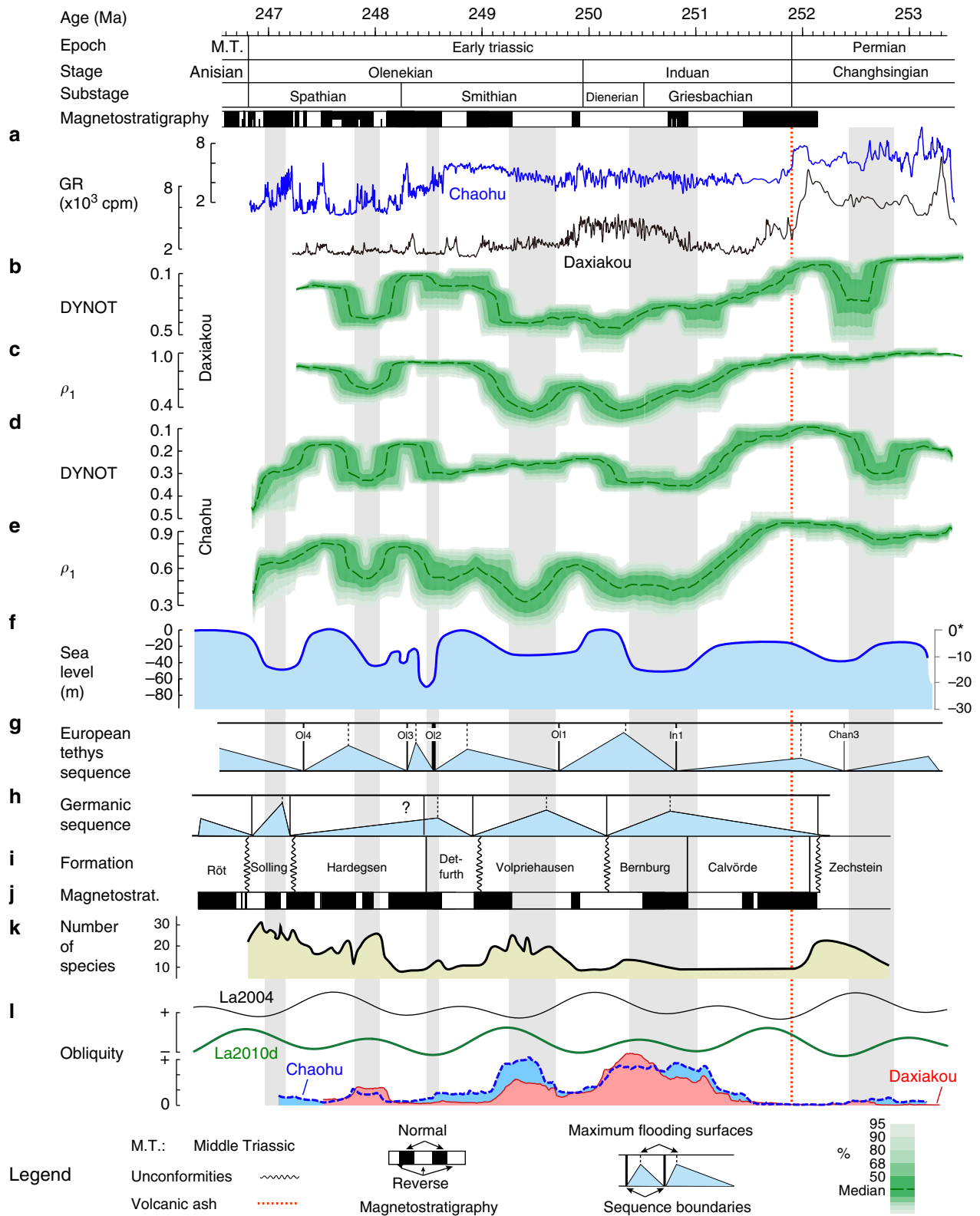


Fig. 6 Global sea level and continental groundwater dynamics during the Early Triassic. Time scale and magnetostratigraphy are from ref.13,14. **a** GR series at Daxiakou (black) and Chaohu (blue) are from ref.13. cpm: counts per minute. **b, c** DYNOT and ρ_1 models of the GR series at Daxiakou. **d, e** DYNOT and ρ_1 models of the GR series at Chaohu. The DYNOT and ρ_1 models were estimated using a running window of 400 kyr (see Supplementary Tab. 1 for sample rates for each spectrum). Confidence levels were estimated by a Monte Carlo analysis with 5000 iterations. **f, g** Sequence and sea-level variations of the European Tethys^{7,9} (*Supplementary Note 2 and Supplementary Fig. 13 for details). **h-j** Lithology, magnetostratigraphy, sequences in the continental Germanic Basin^{13,40} (Fig. 5 for details). **k** Spores and pollen diversity in Pakistan⁴⁷. **l** Earth's obliquity forcing intensity of La2004¹⁹, La2010d⁴⁹ and in South China³¹

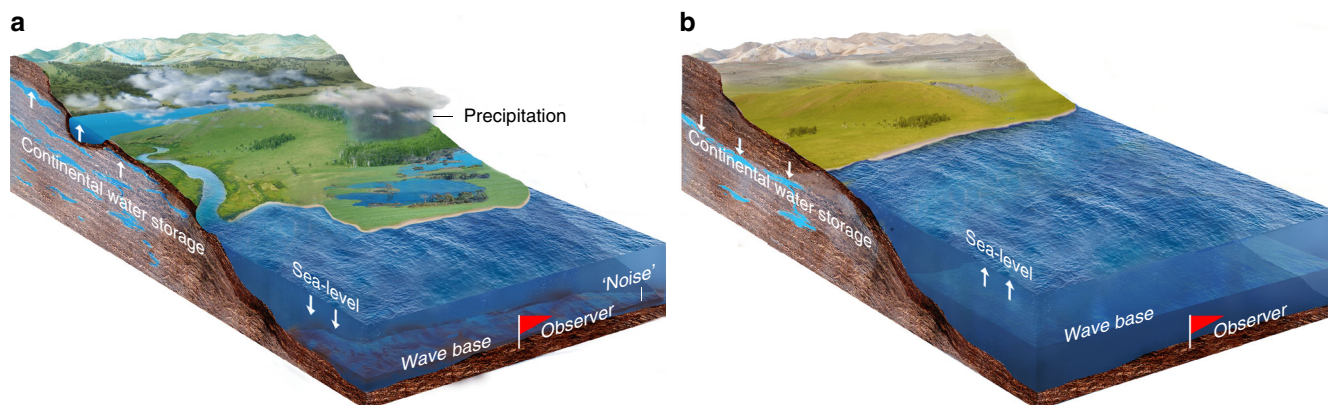


Fig. 7 Water exchange between continental water storage and the ocean forced by astronomically forced climate change leads to major sea-level variations. **a** More moisture transferred to the continent leads to recharging of groundwater and lakes, and a flourishing terrestrial ecosystem. This results in a lowering of sea-level and wave base and more environmental noise (e.g., increased sediment mixing) at the location of observer (red flag). **b** Less moisture transferred to the continent leads to depleted groundwater and lakes, and a rise in sea-level and wave base with less environmental noise at the location of the observer. Illustrations © Hewei Duan

Röt Formation consists of fluvial sandstones and shales interbedded with halite deposits, deposited in a playa-like environment with multiple marine incursions^{40,41}.

Stratigraphic unconformities indicative of sequence boundaries show that lake levels and groundwater tables decline in the uppermost Zechstein Group, the base of the Volpriehausen, Detfurth, Hardegsen (?), Solling and Röt formations (Fig. 5). Maximum flooding surfaces are recognized in the lower Bernburg, the upper Volpriehausen, top of the Detfurth, the lower part of the Solling and the middle-upper of the Röt formations^{40,41}. Orbitally tuned magnetostratigraphic correlation between South China and Germany^{13,37} provides an integrated time scale and reveals that major continental water-storage falls (sequence boundaries in the Germanic Basin) occurred during the latest Changhsingian, late Dienerian, middle Smithian, latest Smithian (?), late Spathian, and end-Spathian, and rapid increases (maximum flooding surfaces in the Germanic Basin) in the late Griesbachian, early Smithian, late Smithian, and late Spathian (Fig. 5). Among these, continental water-storage falls in the latest Changhsingian, late Dienerian, middle Smithian, and latest Smithian occurred in times of quick marine incursions. And fast increase in continental water-storage in the late Griesbachian, early Smithian and late Smithian occurred in times of sea-level falls. In other words, the ages and patterns of sequence boundaries and maximum flooding surfaces of global eustasy and Germanic terrestrial stratigraphy indicate that water masses ‘see-sawed’ between continental reservoirs and ocean throughout the Early Triassic hothouse (Figs. 6 and 7).

This ‘see-saw’ relationship becomes indistinct in the middle Spathian through the earliest Anisian (Fig. 6g, h). The interpretation is that regional tectonics may have contributed to the late Spathian unconformity between the Hardegsen and Solling formations in the Germanic Basin^{40,41}. The sequences of the Anisian Röt Formation reflects frequent marine incursions^{37,40}, which is expected to be in-phase with global sea-level change.

Marine transgressions and regressions were also considered to drive Early Triassic sequences in the Germanic Basin⁴⁰. However, the Germanic Basin is a land-locked terrestrial basin without connection to the open sea during the Early Triassic; marine incursions recurred only in the Anisian^{38,40}. This evidence of aquifer eustasy does not require a connection via straits between the Germanic Basin and the open ocean; rather, astronomically

forced million-year scale land–ocean water exchange represents an appealing interpretation.

Astronomical forcing of land–ocean water balance dynamics.

The mechanism for high-amplitude glacio-eustasy has been linked to astronomically forced ice sheet growth and decay^{2,42–44}. Paleoclimate studies indicate that the primary beat of the late Cenozoic ice sheets dynamics and high-amplitude sea-level variations is in the obliquity band⁴⁴. In ice-free worlds, eccentricity-precession signals dominate climate change^{44,45}. The evidence extends to the long-period modulations of the obliquity and eccentricity: 1.2 myr obliquity variation nodes (modulation minima) are associated with glaciation and third-order glacioeustatic sequences^{42,43}, while the 2.4 myr eccentricity modulations are associated with climate and sea-level oscillations in greenhouses⁴⁵.

The correlated magnetostratigraphy and cyclostratigraphy of the Early Triassic Germanic Basin and South China provides robust geological evidence that continental aquifer had a major impact on global sea level. Time-series analysis of the GR series and field observations in South China reveals 1.2 myr obliquity modulation cycles that are linked to Early Triassic sea levels and biodiversities³¹. Lower water storage in the Germanic Basin correlates with high sea level and decreased obliquity forcing in both South China and the La2010d astronomical solution (Fig. 6). Climate simulations and sedimentological evidence for alluvial plain and playa-lake deposits suggest that groundwater fluctuations in the Germanic Basin result from precipitation changes on the remnants of the Hercynian (Variscan)–Appalachian Mountains^{38,39}, i.e., a variable precipitation intensity drove changes in aquifer capacity in the Germanic Basin. This suggests the missing link between long-term obliquity forcing and million-year scale sea-level change: climate studies of the late Cenozoic icehouse have proposed that obliquity forcing dominated poleward flux of heat, moisture, and precipitation through the control of the meridional insolation gradient⁴⁶. This mechanism may be extended to deep time with no ice sheets and to the long-period obliquity modulations. The 1.2 myr obliquity nodes are associated with reduced transportation of heat, moisture, and precipitation; the 1.2 myr obliquity variation maxima are linked to re-invigorated heat and moisture transportation and intensified precipitation^{27–29,31} (Supplementary Note 3).

The time to significantly affect a groundwater reservoir after changes in global hydrologic cycle is estimated to be in the order of 10^4 – 10^5 years³⁰; this is sufficient to force 100 kyr to million-year scale variations in sea-level^{32,33}. The groundwater-driven eustasy is driven by dynamic balance between filling (via precipitation) and discharge (via evapotranspiration and runoff) of continental aquifers that influenced by the hydrologic cycle²⁸, which is ultimately driven by paleoclimate change^{3,33}. Consequently, obliquity-forced million-year scale variations in precipitation may have paced the recharging and drainage of the continental reservoirs. Recharging and drainage of groundwater and lakes indicates a significant water exchange between land and ocean, which may have paced the evolution of terrestrial ecosystems, e.g., spore and pollen diversity^{31,47} (Fig. 6k).

Evidence of million-year scale obliquity-forced land–ocean water balance dynamics is strongest during the Induan-middle Smithian interval. The relationship weakens during the middle Spathian-earliest Anisian, partly because of lower obliquity band variance (e.g., Fig. 6l), the late Spathian tectonics and the earliest Anisian marine incursions in the Germanic Basin (see above). Future climate modeling and documentation of groundwater variations in other Early Triassic climate zones will further clarify this hypothesis of anti-phasing between global sea level and continental water reservoir changes.

Discussion

Sea-level change reconstruction based on marginal marine depositional sequences is a difficult task that depends on subjective sedimentological interpretation. Monte Carlo simulations of a sedimentary noise model that links the intensity of sedimentary noise to sea-level change provides an independent method for simultaneously estimating geologic time and sea-level change from astronomically forced depositional successions. Two approaches are proposed for the sedimentary noise model, i.e., dynamic noise after orbital tuning (DYNOT) and the lag-1 autocorrelation coefficient (ρ_1). DYNOT and ρ_1 modeling of a GR series of ODP Site 1119 over the past 1.4 myr correlates with the classic low-passed $\delta^{18}\text{O}$ sea-level curve, demonstrating the efficacy of the sedimentary noise model.

Application of the sedimentary noise model to Early Triassic marine successions of South China reveals a multi-million-year history of sea-level change. The sea-level record of South China correlates with that observed in European Tethys, and these together are anti-phased with water storage variations inferred from sequence stratigraphy in the continental Germanic Basin. This geological evidence demonstrates long-term (1–2 myr) water mass exchange between the ocean and continental reservoirs (Fig. 7). The evidence suggests that obliquity-forced continental reservoir changes had a significant impact on global sea-level variations and terrestrial ecosystems during the Early Triassic and possibly throughout geologic time.

The mystery of large, million-year scale sea-level oscillations during non-glacial times challenges current knowledge of global sea-level change. Our evidence that water masses ‘see-sawed’ between continental reservoirs and ocean during the Early Triassic indicates that long-term obliquity-forced land–ocean water exchange is the missing link for reconciling geological records and models for sea-level change in ancient hothouses lacking ice sheets.

Sea-level rise is one of the most serious impacts of present-day climate change. In the Intergovernmental Panel on Climate Change (IPCC) assessment report, rising global sea level has been primarily linked to two factors related to global warming: land ice melting and the thermal expansion of sea-water⁴⁸. The importance of groundwater fluctuations may be underestimated in

long-term projections of global sea-level change due to lack of data or understanding of land–ocean water balance dynamics. The present-day volume of groundwater storage is equivalent to a sea-level differential of approximately 320–330 m^{35,36}. Thus, as present-day Earth continues toward both warmer climate and lower obliquity angles, changes in continental aquifers should be reassessed for their contribution to global sea-level variations in long-term future projections.

Methods

Dynamic noise after orbital tuning. DYNOT is assessed from the ratio of total orbital signal variance to total variance in a climate proxy time series. Time-dependent ratios of variance in the orbital band are obtained from 2π multiaper variance (power) spectra calculated along a sliding time window using the Matlab script ‘pda.m’³¹.

The noise after removal of orbital variance in a given time interval is:

$$R = 1 - \frac{P_{(e)} + P_{(o)} + P_{(p)}}{\sum_{i=f_{\min}}^{f_{\max}} P_{(i)}} \quad (1)$$

where f_{\min} and f_{\max} are cutoff frequencies for estimation of total variance between $f_{\min} = 0.001$ per kyr, and $f_{\max} = 1$ per kyr. $P_{(e)}$, $P_{(o)}$, and $P_{(p)}$ are the power of eccentricity, obliquity and precession signals as defined below:

$$P_{(e)} = \sum_{i=c1}^{c2} P_{(i)} + \sum_{i=c3}^{c4} P_{(i)} + \sum_{i=c5}^{c6} P_{(i)} \quad (2)$$

where $c1$, $c2$, $c3$, $c4$, $c5$ and $c6$ are cutoff frequencies (in per kyr) for eccentricity cycles of (405 per kyr), (125 per kyr), and (95 per kyr).

$$P_{(o)} = \sum_{i=c7}^{c8} P_{(i)} \quad (3)$$

where $c7$ and $c8$ are cutoff frequencies (in per kyr) for obliquity cycles, which is (40.9 per kyr) in the past 1.4 myr, and (33 per kyr) at 249 Ma^{19,31,49}.

$$P_{(p)} = \sum_{i=c9}^{c10} P_{(i)} + \sum_{i=c11}^{c12} P_{(i)} + \sum_{i=c13}^{c14} P_{(i)} \quad (4)$$

where $c9$, $c10$, $c11$, $c12$, $c13$ and $c14$ are cutoff frequencies (in per kyr) for precession cycles, which are (23.6 per kyr), (22.3 per kyr), and (19.1 per kyr) over the past 1.4 myr. This constitutes the DYNOT approach to sedimentary noise modeling. Proxy series in the stratigraphic domain should be first calibrated to the time domain to reduce effects of variable sedimentation rate, which can lead to frequency splitting in the orbital band. However, a variable sedimentation rate is tolerable, because the DYNOT model adopts a relatively wide passband for assessment of Milankovitch forcing signals.

Lag-1 autocorrelation coefficient. The lag-1 autocorrelation coefficient (ρ_1) is given by ref.12:

$$\rho_1 = \frac{\sum_{i=2}^n x_{(i)} * x_{(i-1)}}{\sum_{i=2}^n x_{(i)}^2} \quad (5)$$

where, x is the orbitally tuned stratigraphic proxy series. The advantage offered by ρ_1 is that it evaluates time series directly and is independent of frequency band selections.

Relationship between DYNOT and ρ_1 models. The DYNOT model removes interpreted orbital variance from what are typically the lower frequencies in cyclostratigraphic power spectra; the proportion of non-orbital variance in the power spectrum (equation (1)) is taken to represent uncorrelated noise. In comparison, the ρ_1 model is a simple measure of the distribution of variance across the power spectrum. The most renowned application of ρ_1 is for first order autoregressive modeling of red noise spectra¹¹. For lower values of ρ_1 , variance is more uniformly distributed across the power spectrum; for higher values of ρ_1 , variance occurs preferentially in the low frequencies (e.g., Fig. 4.18 in ref. 50). That is, ρ_1 measures the ‘redness’ of variance as a function of frequency: less red (lower ρ_1) values are taken to represent more uncorrelated noise; higher ρ_1 values are associated with ‘redder’ spectra, and to lower dynamic noise. It is therefore no accident that the DYNOT and ρ_1 models move in opposite directions to mark the presence of uncorrelated noise.

Uncertainty analysis of the sedimentary noise model. We use a Monte Carlo method to evaluate uncertainty of the DYNOT and ρ_1 models of stratigraphic noise. There are two uncertainties associated with the ρ_1 model, i.e., sampling rate

and running window size, and 16 uncertainties with the DYNOT model, e.g., sampling rate, running window size, and 14 bandpass cutoff frequencies for 7 target orbital frequencies (Supplementary Tab. 1). Median DYNOT and ρ_1 model values and their 50%, 68%, 80%, 90%, and 95% significance intervals for any given time are estimated by Monte Carlo simulation with 5000 to 10,000 iterations. The uncertainties and their ranges are discussed below.

Sampling rate is a complex issue for deep-time paleoclimate data with uncertain timescales, especially for data that have not been measured at a uniform sample spacing, or data that have been time-calibrated⁵⁰. This is the case for all data in this study (Supplementary Tab. 2).

For the DYNOT model, non-uniformly sampled paleoclimate time series can be interpolated to a uniform sampling rate to allow application of powerful time series methods for uniformly sampled time series, e.g., the multitaper (MTM) power spectrum⁵¹. Here, a Monte Carlo method of hypothesis testing using the MTM power spectral analysis is undertaken, and so resampling must be applied.

Sampling rates of proxy datasets in time are always greater than zero and so are non-normally distributed. Therefore we selected the Weibull distribution⁵² to represent sampling rate distributions for the uncertainty analysis of the DYNOT model. The Weibull probability plot⁵² of sampling rates of the gamma ray time series at Site 1119 is nearly linear, indicating that the sampling rates are reasonably fit by a Weibull distribution (Supplementary Fig. 2). To avoid ultralow or ultrahigh, unrealistic sampling rates we set the 5th and 95th percentiles of sampling rates as lower and upper limits of Monte Carlo-generated Weibull-distributed sampling rates.

Based on definition of the ρ_1 model (equation 5), upsampling to increase sampling rate leads to artificially high ρ_1 values. In comparison, downsampling to decrease sampling rate results in relatively low ρ_1 values. To address this problem, we apply the uniform distribution to represent sampling rates for the uncertainty analysis of the ρ_1 model. To avoid ultralow and ultrahigh, inappropriate sampling rates we set the 95th percentiles of sampling rates (sr_1) as the lower limit of Monte Carlo-generated uniformly distributed sampling rates and 1.5–2.0 times sr_1 as the upper limit (Supplementary Tab. 2).

The dynamic stratigraphic noise spectrum is calculated with a running time window across a uniformly sampled climate proxy series. Different windows can affect DYNOT and ρ_1 results in two ways:

First, a large window will shorten the number of calculated model values, and a small window will generate more calculated model values, $N_r = N_{\text{data}} - N_{\text{win}} + 1$, where N_r is total number of model values for a given simulation, N_{data} is total number of interpolated data points, and N_{win} is number of points in the running window. Thus, smaller N_r compared to N_{data} leads to a ‘no data’ effect at the beginning and end of the noise output. To avoid this problem, the dynamic noise model randomly shifts and plots simulation results of a single iteration at the same time scale of the dataset, although this generates relatively smoothed dynamic noise spectra when a gap is shorter than $2 \times N_{\text{win}}$ (e.g., the gap η in Supplementary Fig. 1).

Secondly, modeling with a small running window generates higher frequency results (Supplementary Fig. 7), however, the variance of low-frequency cycles and total variance diminish simultaneously, which leads to increased uncertainty. A small running window also increases the MTM power spectrum bandwidth (i.e., reduces frequency resolution) in the DYNOT model.

The expected sea-level variations of interest in the Early Triassic are 10^4 to 10^6 year scale, i.e., the fifth to third-order scale^{2,5,45}, therefore a comparable or shorter time window (e.g., 300–500 kyr, or shorter) should be adopted for the modeling. A running window of 400 kyr and randomized windows within a 300–500 kyr range show small differences (Supplementary Figs. 1 and 3), indicating that both window settings are appropriate. A small running window of 100 kyr for the ODP Site 1119 generates higher frequency results in the past 1.4 myr (Supplementary Fig. 7), although shortcomings is presented above.

Uncertainties derived from different filter cutoff frequencies apply to the DYNOT model only. For the definition of the noise for orbital tuning (R) in equations (1–4), cutoff frequencies and bandwidths are crucial for variance estimation of eccentricity, obliquity and precession signals. In some circumstances, such as absence of sediment at maximum flooding surfaces and/or short-lived exposure related to brief sea-level fall, the paleoclimate proxy might be known well enough for hiatuses to be detectable⁵³. Multiple hiatuses at random spacing can lead to broadened and shifted frequencies⁵³. The effects of a variable sedimentation rate can also lead to frequency splitting in the astronomical bands. Therefore, definition of cutoff frequencies can introduce uncertainties to the DYNOT model.

Target astronomical frequencies can be estimated from the power spectrum of an astronomical solution, e.g., La2004¹⁹ for given time interval (Fig. 1). During the past several million years, astronomical cycles are dominated by 405 kyr, 125 kyr, and 95 kyr eccentricity cycles, 40.9 kyr obliquity cycles, and 23.6 kyr, 22.3 kyr, and 19.1 kyr precession cycles^{19,49}. During the Early Triassic, Milankovitch cycles were dominated by 405 kyr, 125 kyr, and 95 kyr eccentricity cycles, 33 kyr obliquity cycles, and 21 kyr, 20 kyr, and 17 kyr precession cycles^{19,31,49}.

In equations (1–4), c_1 to c_{14} are cutoff frequencies for 3 eccentricity cycles, 1 obliquity cycle, and 3 precession index cycles. One could set cutoff frequency ranges to a minimum of $\pm 20\%$ of the target frequencies. For example, the obliquity cycles for the past 1.4 myr have a frequency of 0.0244 ± 0.0049 per kyr. However, the MTM power spectrum bandwidth resolution of a single computation in the DYNOT model can be much wider than the above set frequency ranges if the

running window is relatively short. We vary each cutoff frequency assuming a uniform distribution with cutoff frequency ranges at $\pm 90\%$ to $\pm 120\%$ bandwidth (Supplementary Tab. 1). Here the bandwidth (bw) equals nw/N_{win} , where nw is time-bandwidth product of discrete prolate spheroidal sequences used in the multitapers, and N_{win} is length (in data points) of the running window.

Stratigraphy of the Chaohu section. The Chaohu section near Chaohu City, Anhui Province exposes an Upper Devonian to Middle Triassic sedimentary succession. Chaohu is located on the north margin of the South China plate⁵⁴. Depositional environments range from deep basin to base of slope/lower slope facies during the latest Permian to Early Triassic⁵⁴. During the latest Permian to early-middle Early Triassic Epoch, the Chaohu area was in a deep basinal environment with deep-water ammonoid and conodont species^{54,55}. The Changhsingian (latest Permian) Dalong Formation is composed of grayish-black cherty beds and cherty mudstone with deep-water assemblages including the bivalve *Humanopecten* sp., ammonoid *Pseudotiroilites* sp. and radiolarian *Flustrella* sp.⁵⁶. The Lower Triassic Yinkeng, Helongshan and Nanlinghu formations comprise cyclic beds of marine mudstone (or shale) and marlstone. The clay content decreases and carbonate content increases significantly up section, supporting the hypothesis that the Lower Yangtze sedimentary province was shallowing during the late Early Triassic^{54,57} due to the collision of the North China and South China plates in the Middle-Late Triassic⁵⁸.

Sedimentology of the Chaohu section indicates significant sea-level changes throughout the Early Triassic. Li et al.⁵⁷ interpreted a maximum flooding surface in the upper of the Induan Stage at Chaohu. Increased medium-bedded limestone and hummocky cross-stratification near the Induan-Olenekian boundary (Supplementary Figs. 8–10) are interpreted as indicating a relative sea-level fall in the middle Yinkeng Formation. The 20 m thick Helongshan Formation consists of limestone interbedded with green shale and micrite limestone⁵⁴. Thick-bedded limestone with hummocky cross-stratification at the base of the Helongshan Formation indicates a relatively high-energy depositional settings⁵⁷. The abrupt change in lithology from mud-rich sediments at the top of the Yinkeng Formation to thick-bedded limestone in the overlying Helongshan Formation is interpreted as a response to a drop in sea-level. The top of the Helongshan Formation is dominated by dark gray medium-bedded micritic limestone interbedded with black shale and calcareous shale. These characteristics, together with a prominent gamma ray maximum suggest that the top of the Helongshan Formation represents a maximum flooding surface.

The overlying Spathian Nanlinghu Formation is comprised of relatively thick-bedded carbonates. The base of the Nanlinghu Formation has cross-bedding indicative of current ripples, wavy cross bedding and abundant trace fossils, such as *Planolites*, *Palaeophycus*, *Arenicolites*, *Diplocraterion*, *Chondrites*, *Thalassinoides*, and *Monocraterion*²⁵. This evidence, together with absence of pyrite (Supplementary Figs. 9–10), suggests an oxidized⁵⁹, high-energy depositional environment during the sea-level drop in the earliest Spathian. Li et al.⁵⁷ also interpreted a maximum flooding surface in the lower-middle Nanlinghu Formation, which is characterized by thin-bedded limestone, horizontal stratification and high gamma ray values (Supplementary Figs. 9–10).

The Nanlinghu Formation is overlain by the lower Anisian Dong Ma’anshan Formation of a basal brecciated (karstic?) limestone, indicating a relative sea-level fall in the late Spathian (see also ref. 57). This sea-level fall at the northern margin of the South China platform appears to be confirmed by the coeval Guandao section in the Nanpanjiang Basin of South China¹⁴. The late Spathian at Guandao is also characterized by presence of breccia and thick limestone and relatively low gamma ray responses^{13,14}, likely associated with sea-level fall. The Dong Ma’anshan Formation is succeeded by Middle Triassic evaporites and non-marine terrestrial deposits and Late Triassic fluvial-lacustrine deposits in the Lower Yangtze region⁶⁰.

Stratigraphy of the Daxiakou section. The Daxiakou section is located at 6 km east of Xiakou town of Kingshan County, Hubei Province. The lithology at the Daxiakou section is similar to that of the Chaohu section, but with thinner limestone beds and fewer mudstone beds¹³. The latest Permian Dalong Formation is composed of black shale and mudstone interbedded with multiple volcanic ash layers. The Induan-Olenekian Daye Formation is dominated by grayish thin-bedded limestone rhythmically interbedded with marls and mudstone in the lower part, and with thin-bedded limestone in the middle and upper parts^{13,61}. The overlying Middle Triassic Jialingjiang Formation consists of gray limestone, taupé argillaceous dolomite and dark gray dolomitic limestone⁶².

Gamma-ray as paleoclimate proxy. Gamma ray (GR) in sedimentary rocks is a proxy for terrestrial input into the marine depositional environments of our studied sections^{13,31}. GR of sediments is dominated by potassium (K), uranium (U) and thorium (Th)⁶³. K is common in many minerals such as clays, feldspar, mica, and chloride salts. U and Th are concentrated in a number of sedimentary host minerals including clays, feldspar, heavy minerals, and phosphate, and U is often concentrated in organic matter⁶³. At ODP Site 1119 the GR has been interpreted as a proxy of fluctuations in clay content corresponding to variations in the rate of supply of glacial ‘rock flour’ from a waxing and waning South Island ice cap²³. In the Early Triassic, high GR values of post-extinction interval sedimentary rocks are

attributed to clay-rich sediments, while low GR values are linked with coarser-grained rocks and carbonates. Variable clay content can be related to climate change from Milankovitch forcing, e.g., during high eccentricity hotter summers relative to winters may have resulted in intensified weathering and stronger monsoonal climate. More frequent rainfall and runoff would result in greater clay influx into the marine depositional environment, high GR and U, and vice versa^{13,31}. Deep weathering of outcrops can result in leaching of K and U⁶⁴, however, due to the use in the present study of new road-cut sections at Daxiakou and Chaohu dissolution from weathering is minimized.

Astrochronology of gamma ray series at ODP Site 1119. To decipher the impact of dating error to the sedimentary noise model, we applied two age models at ODP Site 1119 in this study: the original chronology from refs. 21,23 and astrochronology based on fine-tuning to monotonic 40.9 kyr obliquity cycles. The original age model at Site 1119 is based on radiocarbon dates for the past 39 ka; prior to 39 ka, 38 selected gamma ray peaks were correlated with tuned $\delta^{18}\text{O}$ records from ODP Sites 758 and 1143 to provide a 3.9-myrr-long time scale^{21,23}. The mean chronological uncertainty is less than 22 kyr over 0–1.4 Ma²⁴. The chronology at ODP Site 1119 has elevated uncertainties (up to 100 kyr) at ca. 0.25, 0.38, 0.57–0.78, and 1.19–1.45 Ma²⁴. We thus elected to fine-tune the original gamma-ray series in refs.21,23 using filtered obliquity cycles.

The 40.9 kyr obliquity cycles are predominant from 900 ka to 1400 ka in the gamma-ray variations at ODP Site 1119; they also occur in the gamma-ray series from 0 to 900 ka (Supplementary Fig. 4). Therefore, we filtered the obliquity cycles from the gamma-ray time series in refs. 21,23 and constructed an age model based on the filtered 40.9 kyr obliquity cycles (Supplementary Tab. 3). This age model was used for the fine-tuning of the original gamma-ray series. We then applied the sedimentary noise model to the fine-tuned gamma-ray series (Fig. 3 and Supplementary Figs. 3, 5 and 7).

Astrochronology methods. The identification of the obliquity signal in the gamma ray logs proceeded as follows: The gamma-ray series were pre-whitened using Matlab script ‘smooth.m’ to estimate and subtract an 800-kyr long-term LOWESS curve⁶⁵. Evolutionary fast Fourier transform (FFT) spectrograms for inspecting stratigraphic frequencies and patterns of the untuned and tuned series were computed using ‘evoffm’⁵⁰. The gamma ray logs were analyzed with the multitaper method (MTM) spectral estimator⁵¹ using Matlab’s ‘pmtm.m’. Conventional red noise models of the time series were estimated using the Matlab script ‘redconf.m’⁶⁶. Based on the inferred wavelengths of prominent cycles, Gaussian bandpass filtering was applied in Matlab to isolate potential orbital parameters using ‘gaussfilter.m’⁵⁰. The original series was fine-tuned using ‘depthtotime.m’ Matlab script⁵⁰ based on the 40.9 kyr obliquity cycles identified by filtering.

Astronomical solutions. La2004¹⁹ and La2010⁴⁹ are astronomical solutions of Earth’s eccentricity, obliquity, and precession index for the 0–250 Ma. Solutions La2010a, b and c are based on the INPOP08 ephemeris while La2010d is based on INPOP06⁴⁹. INPOP06 was later found to be more precise than INPOP08⁶⁷, (INPOP = Intégration Numérique Planétaire de l’Observatoire de Paris). While a strictly accurate astronomical solution is not available for times before 50–60 Ma⁴⁹, the 1.2 myr obliquity modulation persists in both La2004 and La2010d solutions through 249 Ma³¹. La2010d obliquity modulations were obtained using the procedure in refs.^{31,68}.

Code availability. The software (*Acycle v0.1.3*) that supports the findings of this study is available from the corresponding author M.L. on request.

Data availability. The gamma ray data at Chaohu, Daxiakou sections and ODP Site 1119 can be found at <https://doi.org/10.1016/j.epsl.2016.02.017> and <https://doi.org/10.1126/science.1093726>.

Received: 22 August 2017 Accepted: 15 February 2018

Published online: 08 March 2018

References

- Haq, B. U. Cretaceous eustasy revisited. *Glob. Planet. Change* **113**, 44–58 (2014).
- Miller, K. G. et al. The Phanerozoic record of global sea-level change. *Science* **310**, 1293–1298 (2005).
- Jacobs, D. K. & Sahagian, D. L. Climate-induced fluctuations in sea level during non-glacial times. *Nature* **361**, 710–712 (1993).
- Hinnov, L. & Park, J. J. Strategies for assessing early-middle (Pliensbachian–Aalenian) Jurassic cyclochronologies. *Philos. Trans. R. Soc.* **357**, 1831–1859 (1999).
- Haq, B. U. & Schutter, S. R. A chronology of Paleozoic sea-level changes. *Science* **322**, 64–68 (2008).
- Haq, B. U., Hardenbol, J. & Vail, P. R. Chronology of fluctuating sea levels since the Triassic. *Science* **235**, 1156–1167 (1987).
- Snedden, J. & Liu, C. A compilation of Phanerozoic sea-level change, coastal onlaps and recommended sequence designations. *AAPG Search and Discovery Article* **40594**, http://www.searchanddiscovery.com/pdfz/documents/2010/40594snedden/ndx_snedden.pdf.html (2010).
- Catuneanu, O. et al. Towards the standardization of sequence stratigraphy. *Earth Sci. Rev.* **92**, 1–33 (2009).
- Hardenbol, J. et al. Mesozoic and Cenozoic sequence chronostratigraphic framework of European basins. *Mesozoic and Cenozoic Sequence Stratigraphy of European Basins*, **60**, 3–13 (Soc. Sediment. Geol. Spec. Publ., 1998).
- Meyers, S. R. & Hinnov, L. A. Northern Hemisphere glaciation and the evolution of Plio-Pleistocene climate noise. *Paleoceanography* **25**, PA3207, <https://doi.org/10.1029/2009PA001834> (2010).
- Mudelsee, M. *Climate Time Series Analysis*, 454 (Springer, 2010).
- Mudelsee, M. TAUEST: A computer program for estimating persistence in unevenly spaced weather/climate time series. *Comput. Geosci.* **28**, 69–72 (2002).
- Li, M. et al. Astronomical-cycle scaling of the end-Permian extinction and the Early Triassic Epoch of South China and Germany. *Earth. Planet. Sci. Lett.* **441**, 10–25 (2016).
- Li, M. et al. Astrochronology of the Anisian stage (Middle Triassic) at the Guandao reference section, South China. *Earth. Planet. Sci. Lett.* **482**, 591–606 (2018).
- Hinnov, L. A. Cyclostratigraphy and its revolutionizing applications in the earth and planetary sciences. *Geol. Soc. Am. Bull.* **125**, 1703–1734 (2013).
- Mudelsee, M., Bickert, T., Lear, C. H. & Lohmann, G. Cenozoic climate changes: A review based on time series analysis of marine benthic $\delta^{18}\text{O}$ records. *Rev. Geophys.* **52**, 333–374 (2014).
- Rial, J. A. & Anaclerio, C. Understanding nonlinear responses of the climate system to orbital forcing. *Quat. Sci. Rev.* **19**, 1709–1722 (2000).
- Ripepe, M. & Fischer, A. G. Stratigraphic rhythms synthesized from orbital variations. *J. Sediment. Petrol.* **63**, 335–344 (1991).
- Laskar, J. et al. A long-term numerical solution for the insolation quantities of the Earth. *Astron. Astrophys.* **428**, 261–285 (2004).
- Shipboard Scientific Party. Site 1119: Drift accretion on Canterbury slope. *Proc. Ocean Drill Prog. Initial Rep.* Vol. 181 (eds. Carter, R. M. et al.) (College Station, TX, 1999).
- Carter, R. M., Gammon, P. R. & Millwood, L. Glacial–interglacial (MIS 1–10) migrations of the Subtropical Front across ODP Site 1119, Canterbury Bight, Southwest Pacific Ocean. *Mar. Geol.* **205**, 29–58 (2004).
- Carter, R., Fulthorpe, C. & Lu, H. Canterbury drifts at Ocean Drilling Program Site 1119, New Zealand: climatic modulation of southwest Pacific intermediate water flows since 3.9 Ma. *Geology* **32**, 1005–1008 (2004).
- Carter, R. M. & Gammon, P. New Zealand Maritime Glaciation: Millennial-scale southern climate change since 3.9 Ma. *Science* **304**, 1659–1662 (2004).
- Carter, R. M. A New Zealand climatic template back to c. 3.9 Ma: ODP Site 1119, Canterbury Bight, south-west Pacific Ocean, and its relationship to onland successions. *J. R. Soc. N. Z.* **35**, 9–42 (2005).
- Chen, Z.-Q., Tong, J. & Fraiser, M. L. Trace fossil evidence for restoration of marine ecosystems following the end-Permian mass extinction in the Lower Yangtze region, South China. *Palaeogeogr. Palaeoclimatol. Palaeoecol.* **299**, 449–474 (2011).
- Embry, A. F. Global sequence boundaries of the Triassic and their identification in the Western Canada Sedimentary Basin. *Bull. Can. Pet. Geol.* **45**, 415–433 (1997).
- Wendler, J. E., Meyers, S. R., Wendler, I. & Kuss, J. A million-year-scale astronomical control on Late Cretaceous sea-level. *Newsl. Stratigr.* **47**, 1–19 (2014).
- Wendler, J. E. & Wendler, I. What drove sea-level fluctuations during the mid-Cretaceous greenhouse climate? *Palaeogeogr. Palaeoclimatol. Palaeoecol.* **441**, 412–419 (2016).
- Wendler, J. E., Wendler, I., Vogt, C. & Kuss, J. Link between cyclic eustatic sea-level change and continental weathering: Evidence for aquifer-eustasy in the Cretaceous. *Palaeogeogr. Palaeoclimatol. Palaeoecol.* **441**, 430–437 (2016).
- Hay, W. W. & Leslie, M. A. Could possible changes in global groundwater reservoir cause eustatic sea-level fluctuations. *Sea-Level Change* 161–170 (National Academies Science, Washington D.C., 1990).
- Li, M. et al. Obliquity-forced climate during the Early Triassic hothouse in China. *Geology* **44**, 623–626 (2016).
- Wagreich, M., Lein, R. & Sames, B. Eustasy, its controlling factors and the Limno-eustatic hypothesis—concepts inspired by Eduard Suess. *Aust. J. Earth Sci.* **107**, 115–131 (2014).
- Sames, B. et al. Review: Short-term sea-level changes in a greenhouse world – a view from the Cretaceous. *Palaeogeogr. Palaeoclimatol. Palaeoecol.* **441**, 393–411 (2016).
- Haq, B. U. & Huber, B. T. Anatomy of a eustatic event during the Turonian (Late Cretaceous) hot greenhouse climate. *Sci. China Earth Sci.* **60**, 20–29 (2017).

35. Southam, J. & Hay, W. Global sedimentary mass balance and sea level changes. in *The sea*, Vol. 7 (ed. Emiliani, C.) 1617–1684 (Harvard Univ. Press, Cambridge, 1981).
36. Peters, S. & Husson, J. Phanerozoic growth of the epicontinental sedimentary reservoir: implications for long-term sea level change. *AGU Fall Meeting* (San Francisco, CA, 2015).
37. Szurlies, M. Latest Permian to Middle Triassic cyclo-magnetostratigraphy from the Central European Basin, Germany: Implications for the geomagnetic polarity timescale. *Earth Planet. Sci. Lett.* **261**, 602–619 (2007).
38. Bourquin, S., Guillocheau, F. & Péron, S. Braided rivers within an arid alluvial plain (example from the Lower Triassic, western German Basin): recognition criteria and expression of stratigraphic cycles. *Sedimentology* **56**, 2235–2264 (2009).
39. Péron, S., Bourquin, S., Fluteau, F. & Guillocheau, F. Paleoenvironment reconstructions and climate simulations of the Early Triassic: impact of the water and sediment supply on the preservation of fluvial systems. *Geodin. Acta* **18**, 431–446 (2005).
40. Aigner, T. & Bachmann, G. H. Sequence-stratigraphic framework of the German Triassic. *Sediment. Geol.* **80**, 115–135 (1992).
41. Bourquin, S., Durand, M., Diez, J., Broutin, J. & Fluteau, F. The Permian-Triassic boundary and Early Triassic sedimentation in Western European basins: an overview. *J. Iber. Geol.* **33**, 221–236 (2007).
42. Lourens, L. J. & Hilgen, F. J. Long-periodic variations in the earth's obliquity and their relation to third-order eustatic cycles and late Neogene glaciations. *Quat. Int.* **40**, 43–52 (1997).
43. Pälike, H. et al. The heartbeat of the Oligocene climate system. *Science* **314**, 1894–1898 (2006).
44. Zachos, J., Pagani, M., Sloan, L., Thomas, E. & Billups, K. Trends, rhythms, and aberrations in global climate 65 Ma to present. *Science* **292**, 686–693 (2001).
45. Bouilila, S. et al. On the origin of Cenozoic and Mesozoic “third-order” eustatic sequences. *Earth Sci. Rev.* **109**, 94–112 (2011).
46. Raymo, M. E. & Nisancioglu, K. The 41 kyr world: Milankovitch's other unsolved mystery. *Paleoceanography* **18**, 1011, <https://doi.org/10.1029/2002PA000791> (2003).
47. Hermann, E., Hochuli, P. A., Bucher, H. & Roohi, G. Uppermost Permian to Middle Triassic palynology of the Salt Range and Surghar Range, Pakistan. *Rev. Palaeobot. Palynol.* **169**, 61–95 (2012).
48. Stocker, T. F. et al. *Climate change 2013: The physical science basis.* (Cambridge University Press, 2014).
49. Laskar, J., Fienga, A., Gastineau, M. & Manche, H. La2010: a new orbital solution for the long-term motion of the Earth. *Astron. Astrophys.* **532**, A89, <https://doi.org/10.1051/0004-6361/201116836> (2011).
50. Kodama, K. P. & Hinnov, L. *Rock Magnetic Cyclostratigraphy*, 176 (Wiley-Blackwell, 2015).
51. Thomson, D. J. Spectrum estimation and harmonic analysis. *Proc. IEEE* **70**, 1055–1096 (1982).
52. Nelson, W. B. *Applied Life Data Analysis* (Addison-Wesley, 1982).
53. Weedon, G. P. *Time Series Analysis And Cyclostratigraphy: Examining Stratigraphic Records Of Environmental Cycles*, 259 (Cambridge University Press, 2003).
54. Tong, J., Zhao, L., Zuo, J., Hansen, H. & Zakharov, Y. An intergrated Lower Triassic sequence in Chaohu, Anhui Province. *Earth Sci.* **30**, 40–46 (2005).
55. Zhao, L. et al. Lower Triassic conodont sequence in Chaohu, Anhui Province, China and its global correlation. *Palaeogeogr. Palaeoclimatol. Palaeoecol.* **252**, 24–38 (2007).
56. Yin, H. et al. *Dongwuan-Indosinian (Late Permian–Middle Triassic) ecostratigraphy of the Yangtze region and its margins* (Science Press, Beijing, 1995).
57. Li, S., Tong, J., Liu, K., Wang, F. & Huo, Y. The Lower Triassic cyclic deposition in Chaohu, Anhui Province, China. *Palaeogeogr. Palaeoclimatol. Palaeoecol.* **252**, 188–199 (2007).
58. Anhui Bureau of Geology and Mineral Resources. *Regional Geology of Anhui Province*, (Geol. Publ. House, Beijing, 1987).
59. Huang, Y., Chen, Z.-Q., Wignall, P. B. & Zhao, L. Latest Permian to Middle Triassic redox condition variations in ramp settings, South China: Pyrite framboid evidence. *Geol. Soc. Am. Bull.* **129**, 229–243 (2017).
60. Li, Y. & Jiang, L. *Stratigraphy (Lithostratic) of Anhui Province*, 271 (China University of Geosciences Press, 1997).
61. Wu, H. et al. Milankovitch and sub-Milankovitch cycles of the early Triassic Daye Formation, South China and their geochronological and paleoclimatic implications. *Gondwana Res.* **22**, 748–759 (2012).
62. Zhu, G., Zhang, S., Liang, Y., Zhou, G. & Wang, Z. Formation mechanism and controlling factors of natural gas reservoirs of the Jialingjiang Formation in the East Sichuan Basin. *Acta Geol. Sin. Engl.* **81**, 805–817 (2007).
63. Schnyder, J., Ruffell, A., Deconinck, J.-F. & Baudin, F. Conjointive use of spectral gamma-ray logs and clay mineralogy in defining late Jurassic–early Cretaceous palaeoclimate change (Dorset, U.K.). *Palaeogeogr. Palaeoclimatol. Palaeoecol.* **229**, 303–320 (2006).
64. Osmond, J. & Ivanovich, M. Uranium-series mobilization and surface hydrology. *Uranium-Series Disequilibrium: Application to Earth, Marine, and Environmental Sciences*, Oxford Sciences Publications, Oxford, 259–289 (1992).
65. Cleveland, W. S. & Devlin, S. J. Locally weighted regression: an approach to regression analysis by local fitting. *J. Am. Stat. Assoc.* **83**, 596–610 (1988).
66. Husson, D. MathWorks File Exchange: RedNoise_ConfidenceLevels. (http://www.mathworks.com/matlabcentral/fileexchange/45539-rednoise-confidencelevels/content/RedNoise_ConfidenceLevels/RedConf.m, 2014).
67. Fienga, A. et al. The INPOP10a planetary ephemeris and its applications in fundamental physics. *Celest. Mech. Dyn. Astr.* **111**, 363–385 (2011).
68. Wu, H. et al. Astrochronology of the Early Turonian–Early Campanian terrestrial succession in the Songliao Basin, northeastern China and its implication for long-period behavior of the Solar System. *Palaeogeogr. Palaeoclimatol. Palaeoecol.* **385**, 55–70 (2013).
69. Szurlies, M. Magnetostratigraphy: the key to a global correlation of the classic Germanic Trias-case study Volpriehausen Formation (Middle Buntsandstein), Central Germany. *Earth. Planet. Sci. Lett.* **227**, 395–410 (2004).
70. Ogg, J. G. Chapter 25: Triassic. in *The Geological Time Scale 2012* (eds. Gradstein, F., Ogg, J., Schmitz, M. & Ogg, G.) 681–730 (Elsevier, 2012).

Acknowledgements

We thank Yang Zhang, Zuoyan Zou, Zhong-Qiang Chen for field assistances. We thank the referees for their detailed comments and instructive suggestions. The Triassic sea-level change and uncertainty analyses benefitted from discussions with Bilal Haq and Zhu Liu. This study was supported by the National Natural Science Foundation of China (No. 41772029, 41322013), Natural Science Foundation for Distinguished Young Scholars of Hubei Province of China (2016CFA051), and 111 Projects (B14031 and B08030). M.L. acknowledges support from the China Scholarship Council (201406410029) for Ph. D. work at Johns Hopkins University.

Author contributions

M.L. and C.H. designed research. M.L. developed the DYNOT and ρ_1 models with contributions from L.H. M.L. analyzed data. The paper was written by M.L. and L.H. with contributions from C.H. and J.O.

Additional information

Supplementary Information accompanies this paper at <https://doi.org/10.1038/s41467-018-03454-y>.

Competing interests: The authors declare no competing interests.

Reprints and permission information is available online at <http://npg.nature.com/reprintsandpermissions/>

Publisher's note: Springer Nature remains neutral with regard to jurisdictional claims in published maps and institutional affiliations.

 **Open Access** This article is licensed under a Creative Commons Attribution 4.0 International License, which permits use, sharing, adaptation, distribution and reproduction in any medium or format, as long as you give appropriate credit to the original author(s) and the source, provide a link to the Creative Commons license, and indicate if changes were made. The images or other third party material in this article are included in the article's Creative Commons license, unless indicated otherwise in a credit line to the material. If material is not included in the article's Creative Commons license and your intended use is not permitted by statutory regulation or exceeds the permitted use, you will need to obtain permission directly from the copyright holder. To view a copy of this license, visit <http://creativecommons.org/licenses/by/4.0/>.

© The Author(s) 2018



Tracking variable sedimentation rates and astronomical forcing in Phanerozoic paleoclimate proxy series with evolutionary correlation coefficients and hypothesis testing

Mingsong Li^{a,*}, Lee R. Kump^a, Linda A. Hinnov^b, Michael E. Mann^a

^a Department of Geosciences, The Pennsylvania State University, University Park, PA 16802, USA

^b Department of Atmospheric, Oceanic, and Earth Sciences, George Mason University, Fairfax, VA 22030, USA

ARTICLE INFO

Article history:

Received 18 April 2018

Received in revised form 19 August 2018

Accepted 23 August 2018

Available online xxxx

Editor: D. Vance

Keywords:

sedimentation rate

astronomical forcing

Paleocene–Eocene Thermal Maximum

Late Triassic

Devonian

ABSTRACT

This paper addresses two fundamental issues in cyclostratigraphy and paleoclimatology: identification of astronomical forcing in sequences of stratigraphic cycles, and accurate evaluation of variable sedimentation rates. The technique presented here considers these issues part of an inverse problem and estimates the product-moment correlation coefficient between the power spectra of astronomical solutions and paleoclimate proxy series across a range of test sedimentation rates. The number of contributing astronomical parameters in the estimate is also considered. Our estimation procedure tests the hypothesis that astronomical forcing had a significant impact on proxy records. The null hypothesis of no astronomical forcing is evaluated using a Monte Carlo simulation approach. The test is applied using a sliding stratigraphic window to track variable sedimentation rates along the paleoclimate proxy series, in a procedure termed “eCOCO” (evolutionary correlation coefficient) analysis. Representative models with constant and variable sedimentation rates, and pure noise and mixed signal and noise series are evaluated to demonstrate the robustness of the approach. The method is then applied to Cenozoic, Mesozoic and Paleozoic paleoclimate series. The Cenozoic case study focuses on a high-resolution Paleocene–Eocene iron concentration series from ODP Site 1262 (Leg 208) covering the Paleocene–Eocene Thermal Maximum and Eocene Thermal Maximum 2 events. The eCOCO time-calibrated iron series confirms previous findings of a role for long-term astronomical forcing of these Eocene events. The Mesozoic case study applies eCOCO to the classic Late Triassic Newark depth rank series of eastern North America. The estimated high-resolution sedimentation rate map in this case demonstrates a causal link between variations in depositional environment and sedimentation rate. Finally, the Paleozoic case study supports the cyclostratigraphic interpretation of a Devonian magnetic susceptibility series at La Thure, Belgium and provides new insights into changes of the depositional setting at this location. Taken together, eCOCO is a powerful tool for simultaneously evaluating sedimentation rates and astronomical forcing for paleoclimate series throughout the Phanerozoic.

© 2018 Elsevier B.V. All rights reserved.

1. Introduction

Construction of the geological time scale includes multiple sources and methods, radioisotopic dating, biostratigraphy, magnetostratigraphy, chemostratigraphy, cyclostratigraphy, and mathematical modeling. Among these techniques, the cyclostratigraphic analysis of Milankovitch cycles is the only method that can provide continuous, high-resolution age models (Gradstein et al., 2012). Numerous sedimentary records are evidently impacted by Milankovitch forcing at timescales of tens to hundreds of thousands

of years (Hinnov, 2013). The leading present-day astronomical parameters include long orbital eccentricity (405 kyr), short orbital eccentricity (128 kyr and 95 kyr), obliquity (41 kyr), and precession (23 kyr and 19 kyr) cycles (Berger et al., 1992; Laskar et al., 2004, 2011). These parameters affect the timing and geographic distribution of insolation thus acting as a long-term paleoclimatic forcing. Geologists read these cycles using paleoclimate proxy records and link the recognized sedimentary oscillations to the astronomical cycles (Hinnov and Hilgen, 2012). However, this involves multiple ongoing scientific challenges: the uncertain nature of linkages between astronomical forcing and paleoclimate proxies (Hinnov, 2013; Weedon, 2003), potentially low signal to noise ratios in paleoclimate proxy series (Kemp, 2016; Meyers, 2012; Mann and Lees, 1996), confirmation of an astronomical origin in

* Corresponding author.

E-mail address: mul450@psu.edu (M. Li).

successions of stratigraphic oscillations (Malinverno et al., 2010; Meyers, 2015; Meyers and Sageman, 2007), distortion of the astronomical signal due to variable sedimentation rates (Sinnaes et al., 2016; Lin et al., 2014; Weedon, 2003; Yu and Ding, 1998), and integration of cyclostratigraphy with other dating tools (Kuiper et al., 2008; Westerhold et al., 2012), among others.

Here we jointly test the astronomical origin of stratigraphic cycles as measured by paleoclimate proxy data, and estimate the evolution of sedimentation rates along a stratigraphic succession. Our approach employs the correlation coefficient between the power spectra of a proxy series and that of an associated astronomical forcing series, converting the proxy series to time for a range of “test” sedimentation rates. The number of astronomical parameters contributing to the estimated sedimentation rates is taken into account. The null hypothesis of no astronomical forcing is tested using a Monte Carlo simulation approach. A sliding window is applied to the proxy series in order to track changes in sedimentation rate along the stratigraphic succession; thus, we call this the “eCOCO” (evolutionary correlation coefficient) method. The eCOCO method is inspired by the average spectral misfit (ASM) method of Meyers and Sageman (2007), the Bayesian Monte Carlo method of Malinverno et al. (2010) and the TimeOpt method of Meyers (2015); similarities and differences among these methods are discussed below.

The eCOCO method is demonstrated using three synthetic series, and three Phanerozoic paleoclimate proxy series. The transition of the late Paleocene through the early Eocene is characterized by a sequence of significant climate events, including the Paleocene–Eocene Thermal Maximum (PETM) and the Eocene Thermal Maximum 2 (ETM2) events. Cyclostratigraphy of ODP Site 1262 (Leg 208) at Walvis Ridge, South Atlantic Ocean has led to the hypothesis of astronomically forced pacing of the PETM and ETM2 events (Lourens et al., 2005), although this hypothesis has been shown to be complicated in follow-on cyclostratigraphic studies by others (Meyers, 2015; Westerhold et al., 2007, 2008). Differing sedimentation rates for the late Paleocene–early Eocene interval have been proposed (Westerhold et al., 2007, 2008) and only an average sedimentation rate for the PETM–ETM2 interval at Site 1262 has been independently tested (Meyers, 2015). An astronomically tuned time scale of the depth-rank series of continental deposits in the Newark Basin, eastern North America, provides the fundamental basis for the age model of the current Late Triassic time scale (Gradstein et al., 2012; Kent et al., 2017). The late Norian–Rhaetian part of the Newark time scale has been recently supported by the global correlation between cycle calibrated magnetic polarity patterns from the Late Triassic Xujiahe Formation and those from the Newark Supergroup (Li et al., 2017). Cyclostratigraphic study of the Givetian–Frasnian magnetic susceptibility series from the La Thure section of Belgium provides a high-resolution astronomical time scale for the Givetian of the Middle Devonian (De Vleeschouwer et al., 2015). The interpretation of astronomical cycles has been further corroborated by Martinez et al. (2016).

In all three of these Phanerozoic cases, eCOCO-derived high-resolution sedimentation rate results provide new insight into the associated paleoclimatic and paleoenvironmental changes. The eCOCO analysis of our three case studies confirms published sedimentation rates at a high degree of confidence (exceeding 99% significance, i.e., rejection of the null hypothesis at levels of $p < 0.01$). Application of eCOCO in cyclostratigraphy thus has the potential more generally to enhance the reproducibility of astrochronological timescales and contribute to establishing more robust geological age models throughout Earth history.

2. Evolutionary correlation coefficient (eCOCO)

2.1. Correlation coefficient

The correlation coefficient used here is the Pearson product-moment correlation coefficient (Mudelsee, 2014), calculated in MATLAB™ (<https://www.mathworks.com/help/matlab/ref/corrcoef.html>) as

$$\rho(T, D) = \frac{1}{N-1} \sum_{i=1}^N \left(\frac{T_i - \mu_T}{\sigma_T} \right) \left(\frac{D_i - \mu_D}{\sigma_D} \right) \quad (1)$$

where N is a number of observations of the target (T) or data (D) time series, μ_T and σ_T are the mean and standard deviation of the target, and μ_D and σ_D are the mean and standard deviation of the data series. The correlation coefficient measures the linear correlation between the target (T) and data (D) series, where the target series is the power spectrum of the astronomical solution, and the data series is the power spectrum of proxy time series at a given sedimentation rate. The periodogram is a useful metric of agreement because the associated spectral estimates have a narrow resolution bandwidth compared to common procedures such periodogram smoothing or Multi-Taper Method (MTM) spectral estimation (Thomson, 1982). The periodograms of both astronomical target series and data time series are calculated using MATLAB function *periodogram.m* with a zero padded length of 10,000. The red noise background of the data series is modeled using an AR(1) autoregressive fit to the series using MATLAB function *RedConf.m* by Husson (2014) and is employed so as to only retain spectral features that exceed the estimated red noise background; if the spectral amplitude is less than the estimated mean red noise background at a given frequency f , it is set to 0. The range of ρ is between -1 and $+1$, where 1 is a perfect positive correlation, 0 is no correlation, and -1 is a perfect negative correlation.

The highest frequency Milankovitch cycle during the past 249 Ma corresponds to the precession index term at $1/(17 \text{ kyr})$ (Laskar et al., 2004), thus we estimate the correlation coefficient of the periodograms of the target and data series over the frequency range 0 to 0.06 cycles/kyr for Cenozoic and Mesozoic series. The highest frequency of the precession index is $1/(16.4 \text{ kyr})$ at 440 Ma according to Berger and Loutre (1994), and so for the Devonian case study ($\sim 384 \text{ Ma}$) we estimate the correlation coefficient over the frequency range 0 to 0.07 cycles/kyr .

For paleoclimate series younger than 249 Ma , both data and target series are obtained using periodograms of paleoclimate series and Laskar astronomical solutions, respectively. For paleoclimate series older than 249 Ma , a target series is constructed as the sum of harmonic functions whose frequencies are given by Berger and Loutre (1994) using an original MATLAB script *period2spectrum.m*.

2.2. Significance level

In this step, we adopt as a null hypothesis (H_0) the existence of no astronomical frequencies in the data series and all spectral peaks higher than an AR(1) background occur by chance. Since the periodogram is not Gaussian-distributed (it is Chi-Squared), standard parametric distributions for the correlation coefficient ρ are not valid. We instead use a non-parametric Monte Carlo approach to produce a null distribution and to test the null hypothesis of no significant astronomical frequencies, as follows:

- (1) The number of peaks of the periodogram higher than an AR(1) background for the paleoclimate data series is counted as n , and the sampling frequency (df) of data is

$$df = 1/(N * dt) \quad (2)$$

where N is number of data and dt is sampling rate of data. Here n is counted automatically and doesn't have to be the number of Milankovitch cycles that are present in the measured data.

- (2) The modeled data periodogram is constructed with n half sinewaves with randomly distributed frequencies (e.g., half sinewave peaks) and randomly distributed magnitudes (ranges between 0 and 1). Each half sinewave has a width of $2df$.
- (3) We use a Monte Carlo simulation to produce a distribution of values of ρ between the modeled random data periodogram and target periodogram at each tested sedimentation rate.
- (4) The values of ρ from the Monte Carlo simulations is used to construct a null distribution. The probability for the corresponding correlation coefficient at the sedimentation rate to have arisen due to random chance can be estimated from this null distribution.
- (5) The H_0 significance level indicates a specific correlation coefficient value can occur by chance. The H_0 significance level p is considered to be significant if $p < 0.01$, i.e., we would expect a correlation coefficient as large as is estimated to arise from change less than 1% of the time under the null hypothesis.

As an example, the resulting 2000 Monte Carlo surrogate values of ρ between the target periodogram of the La2004 Laskar solution (55–57 Ma) and modeled data periodograms for Synthetic Series #1 (Fig. 1, see section 3.1) yielded values less than the nominal value of 0.7566 (Fig. 2B). This indicates the null hypothesis of no astronomical signal can be rejected at a 0.05% ($p < 0.0005$) significance level at 4 cm/kyr sedimentation rate, i.e., the significance level of the presence of an astronomical signal is 99.95%.

2.3. Number of contributing astronomical parameters

A high, positive ρ and low H_0 significance level may fail to establish the true sedimentation rate. For example, a high positive ρ may occur when only a few astronomical frequencies are used to evaluate the correlation coefficient. To guard against this false positive problem, the total number of contributing astronomical frequencies defined in the target should be evaluated in the correlation coefficient. The number of contributing astronomical frequencies is influenced by two types of influences: Type A arises from the Fourier transform technique that is applied, and Type B derives from the data periodogram at the tested sedimentation rate.

2.3.1. Type A influence

An evenly spaced data series has a stratigraphic sampling interval of Δd ; the sampling time interval of the data series time calibrated to a sedimentation rate (sr) is Δt ($\Delta t = \Delta d/sr$). The Nyquist frequency (f_{nyq}) characterizes the maximum resolvable frequency of the periodogram in both stratigraphic and time domains, and the Rayleigh frequency (f_{ray}) characterizes the resolution of the periodogram in both stratigraphic and time domains. The f_{nyq} and f_{ray} of the periodogram in the time domain are defined as:

$$f_{nyq} = sr/(2 * \Delta d) \quad (3)$$

$$f_{ray} = sr/(N * \Delta d) \quad (4)$$

where N is the total number of samples for a given data series.

Meyers and Sageman (2007) note that for very high or very low sr , f_{nyq} and f_{ray} of the data periodogram may fall outside the range of the astronomical frequencies. For example, given a very high sr , f_{ray} can be higher than the frequency of the 405-kyr orbital eccentricity cycle and in some cases even of the shorter 100-kyr orbital eccentricity cycles. Thus fewer astronomical frequencies will contribute to the estimated ρ , and may lead to a

high ρ at a sedimentation rate that is unreasonably large. For very low sedimentation rates, f_{nyq} may be lower than the frequencies of the ~ 20 kyr precession index (or even lower), leading to fewer astronomical parameters used in ρ estimation.

2.3.2. Type B influence

The Type B influence depends on characteristics of the data periodogram, that is, the peaks of each astronomical frequency band may be detectable in the same band of the series periodogram. The process for estimating the Type B influence is as follows: (1) The data series is time calibrated with a test sedimentation rate; (2) the data periodogram is estimated, and the data AR(1) spectrum is estimated and “removed” as per the procedure described in section 2.1. If the spectral amplitude in a given astronomical frequency band (Fig. 2 and Supplementary Table 1) is 0 as per our procedure, the corresponding astronomical parameter may not be meaningful. For example, if the spectral amplitude (of age 56 Ma) after accounting for the AR(1) spectrum is zero within the obliquity band of 0.0149–0.0321 cycle/kyr (Supplementary Table 1), this suggests that obliquity forcing was not involved, and the number of contributing astronomical parameters can be reduced by 1.

Variable sedimentation rates lead to widened and/or split peaks in the periodogram (Weedon, 2003), therefore, wide frequency bands of the astronomical target frequencies are adopted in this study. For example, for Synthetic Series #1 (Figs. 1–2, with an age of 55–57 Ma, see below), astronomical target frequency bands are listed in Supplementary Table 1. Because relatively broad frequency bands are used, it is worthwhile to note that the number of specific Milankovitch cycles in the data can be overestimated. And it can be difficult to separate various precession cycles in the paleoclimatic series due to variable sedimentation rates, and sedimentary and climatic processes. However, the result of the number of contributing astronomical parameters is still useful as discussed below.

A result with a low number of contributing astronomical frequencies has two possible interpretations. The first interpretation is that the assigned sedimentation rate is not appropriate. The second interpretation is that one or more astronomical frequencies do not have a significant influence in the data series. The metric that records the number of astronomical frequencies is challenged in geological intervals that are dominated by one astronomical parameter or lack a specific astronomical forcing, such as the Pleistocene obliquity world from 1.2 Ma to 2.7 Ma (Ravelo et al., 2004), or the Early Triassic obliquity dominated intervals in Chinese cyclostratigraphy (Li et al., 2016a). However, even in the well-known Pleistocene obliquity world, 12% of the variance in the $\delta^{18}O$ record is in the precession band, whereas 43% is in the obliquity band (Ravelo et al., 2004). Other examples are data series with weak obliquity power from low latitude paleoclimates or hothouses without ice, e.g., the Late Triassic Newark basin (Olsen and Kent, 1996). Therefore, if a low significance level of the null hypothesis derives from the fact that only a few astronomical frequencies were used in the estimation, a high ρ in that case should be considered as suspicious. In other words, the number of Milankovitch cycles that are present in the measured data should be considered if the null hypothesis of no orbital forcing can be rejected.

2.4. Sliding window approach

In our approach, ρ , H_0 significance level and number of contributing astronomical frequencies are made not only for the entire time series, but also along a sliding window along the data series. That is, we begin with a series interval (window) from one end of the series and calculate ρ , H_0 significance level, and the number of contributing astronomical frequencies over a range of sedimentation rates. Then we slide this window for a given step and repeat

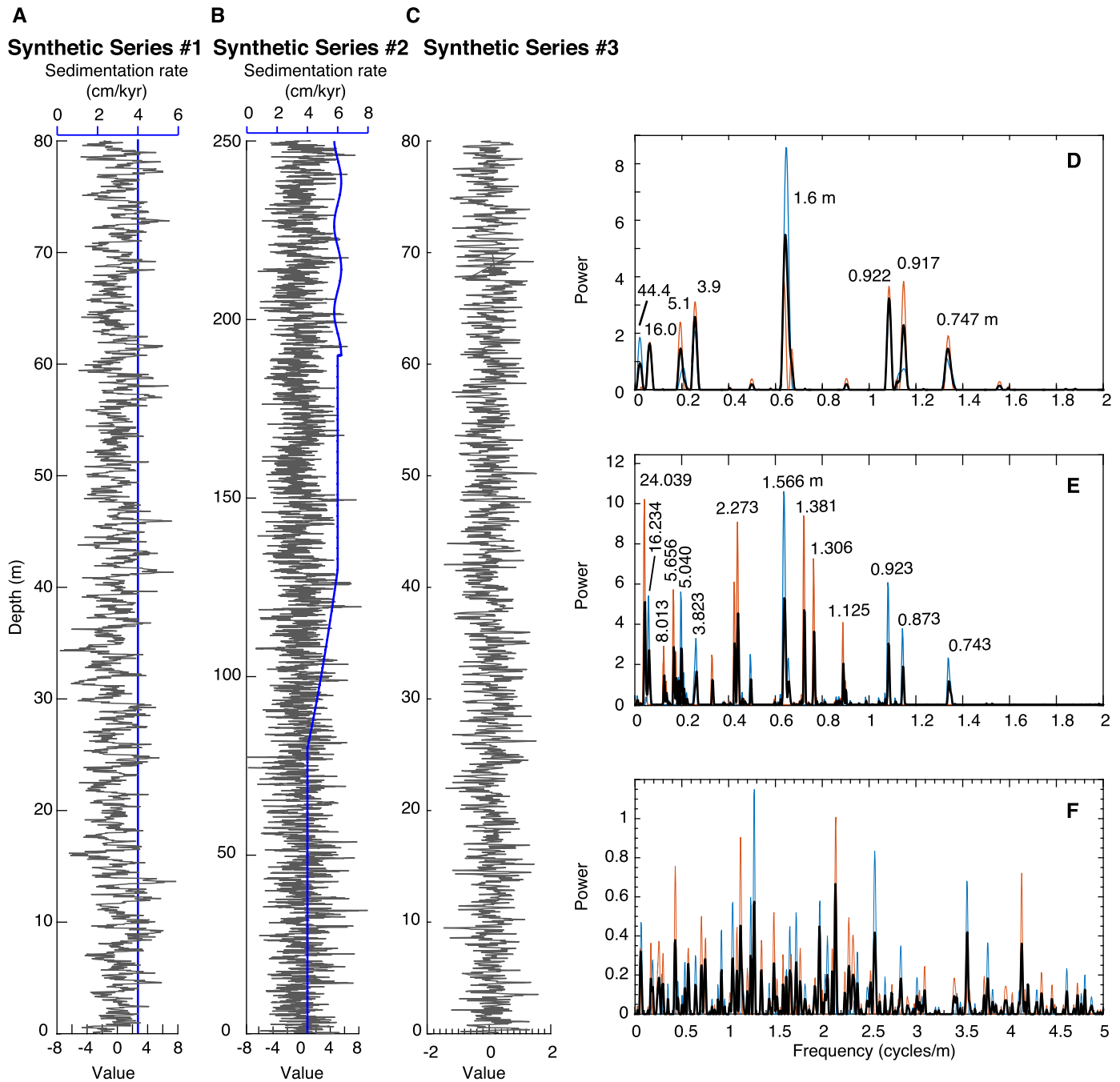


Fig. 1. Three synthetic series and their periodograms. (A) Synthetic Series #1 (black) with a 4 cm/kyr sedimentation rate (blue). (B) Synthetic Series (#2) with sedimentation rates (blue) from 4 to 6 cm/kyr followed by sine wave oscillations. (C) Synthetic Series #3. (D) Periodogram of Synthetic Series #1 after removing the AR(1) model. (E) Periodogram of Synthetic Series #2 after removing the AR(1) model. (F) Periodogram of Synthetic Series #3. (D–F) Thin blue and thin red lines are periodograms of first and second half slices of the synthetic series. The thick black line is the mean periodogram of the 2 slices. (For interpretation of the colors in the figure(s), the reader is referred to the web version of this article.)

the process until we reach another end of the series. This sliding procedure, termed evolutionary correlation coefficient (eCOCO) analysis detects changing sedimentation rates, as demonstrated in the following synthetic series and three Phanerozoic data series.

3. Forward modeling of the astronomical solutions

3.1. Constant sedimentation rate – Synthetic Series # 1

A 4 cm/kyr sedimentation rate is applied to the Laskar 2004 astronomical solutions of eccentricity, obliquity, and precession index from 55 to 57 Ma (Laskar et al., 2004). This series is added to white noise (normal distribution) and red noise (lag-1 autocorrela-

tion coefficient, $\rho_1 = 0.5$), both with a standard deviation of 1. The original sample rate of the La2004 solution is 1 kyr. We thus get a total of 80 m modeled “climate” series with a 0.04 m sampling rates (Fig. 1A).

To increase the degrees of freedom of the periodogram analysis, the whole series was divided into 2 equally sized slices (termed 2-slice COCO analysis). The mean periodogram of the two slices indicate dominant cycles at 44.4 m, 16.0 m, 5.1 m, 3.9 m, 1.6 m, 0.92 m, and 0.75 m (Fig. 1D). The correlation coefficient between the periodogram of Synthetic Series #1 and that of the target Laskar 2004 solution (55–57 Ma) is estimated for a range of sedimentation rates from 1 to 30 cm/kyr with a step of 0.2 cm/kyr.

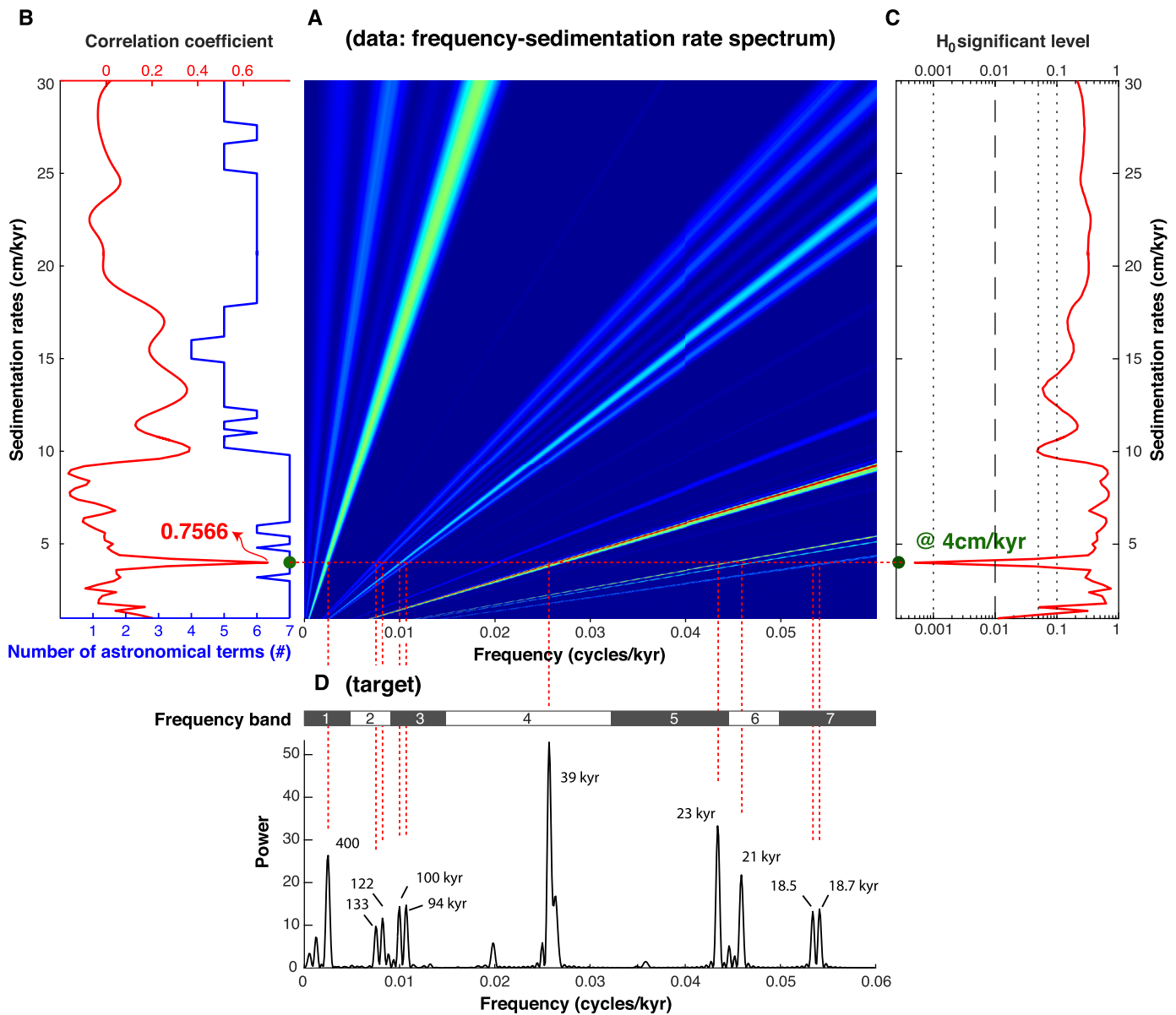


Fig. 2. The eCOCO method. (A) Periodograms of Synthetic Series #1 are shown for sedimentation rates ranging from 1 to 30 cm/kyr (vertical axis) and frequencies from 0 to 0.06 cycles/cm (horizontal axis); power is denoted by color (blue = low; red = high). (B) The correlation coefficient (black line) and the number of contributing astronomical parameters in the target in the tested sedimentation rate (blue line). (C) null hypothesis results. (D) Periodogram of the target La2004 astronomical solution (55–57 Ma) (Laskar et al., 2004). The correlation coefficient of the periodograms of Time Series #1 (A) and astronomical target periodogram (D) indicates a peak at 4 cm/kyr ($\rho = 0.7566$), which is the modeled 4 cm/kyr sedimentation rate. The null hypothesis significance level (H_0 -SL) is 0.0005 (0.05%). Seven astronomical parameters are included for the 4 cm/kyr sedimentation rate. Dashed red lines indicate potential locations for astronomical frequencies at a sedimentation rate of 4 cm/kyr. Synthetic Series #1 is calibrated to time over a sedimentation rate range from 1 to 30 cm/kyr and a step of 0.2 cm/kyr. Significance levels are estimated using Monte Carlo simulation with 2000 iterations, which takes 234 s wall clock time.

The evolutionary correlation coefficient curve shows only one peak at 4 cm/kyr where the correlation coefficient reaches a peak at 0.7566, for which the H_0 hypothesis indicates a 0.05% significance level (Fig. 2). The sedimentation rate is 4 cm/kyr and all seven astronomical frequencies in the target (i.e., 405 kyr long orbital eccentricity, 125 kyr and 95 kyr short orbital eccentricity, 39 kyr obliquity, and the 23 kyr, 22 kyr, and 19 kyr precession index) are involved (Fig. 2D). These results strongly support the hypothesis that Synthetic Series #1 has an astronomical signal (significance level at 99.95%).

3.2. Variable sedimentation rates – Synthetic Series #2

Variable sedimentation rates, if not accounted and corrected for, result in distortion of periodograms (Weedon, 2003). This hampers

the usefulness of the ratio method for cyclostratigraphy. Our sliding window technique obviates this problem.

To demonstrate the ability of eCOCO to identify time-varying sedimentation rates, we use the Laskar 2004 astronomical solution (Laskar et al., 2004) from 53 Ma to 59 Ma to construct a synthetic series. This series is added to a white noise (normal distribution) and a red noise ($\rho_1 = 0.5$) signal, both are with a standard deviation of 1. The modeled sedimentation rate is 4 cm/kyr for the first 2 Myr, then increases from 4 to 6 cm/kyr over the next 1 Myr. The sedimentation rate remains constant at 6 cm/kyr for 1 Myr and then experiences a sine-wave sedimentation rate oscillation for the final 1 Myr (blue line in Fig. 1B). The original sample rate of the La2004 solution is 1 kyr. We thus get a total of 250 m modeled “climate” series with an interpolated 0.04 m sampling rate (black curve in Fig. 1B).

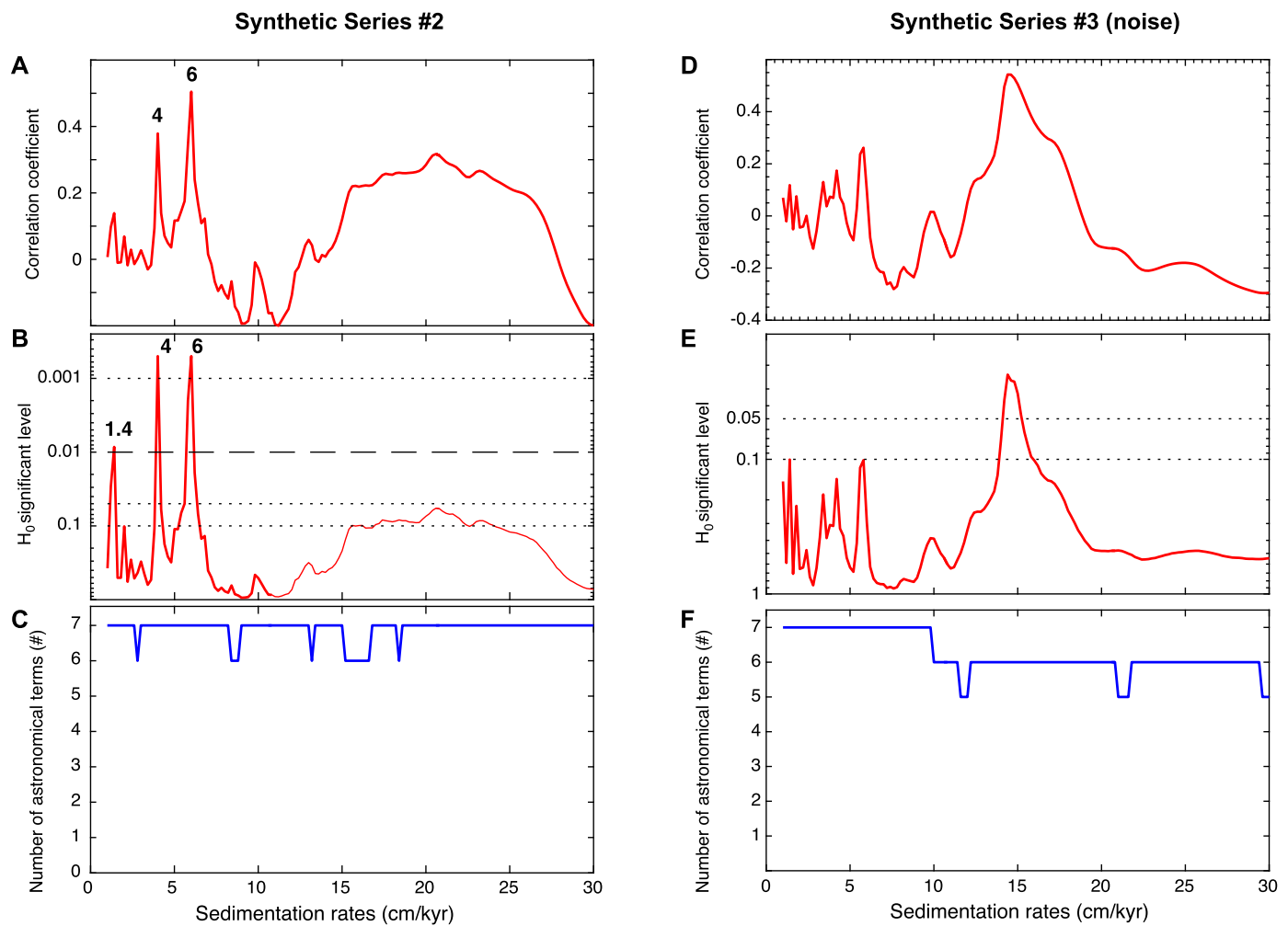


Fig. 3. COCO analysis of Synthetic Series #2 (A–C) and Synthetic Series #3 (D–F). (A and D) The 2-slice COCO analysis shown with labeled potential sedimentation rates. (B and E) Null hypothesis (H_0 , no astronomical forcing) tests indicate that only modeled 4 and 6 cm/kyr sedimentation rates have H_0 significance levels less than 0.001 for Synthetic Series #2 (B) and the null hypothesis cannot be rejected at the 1% significance level for the Synthetic Series #3 (E). Significance levels are estimated using Monte Carlo simulation of 2000 iterations. (C and F) The number of contributing astronomical parameters in tested sedimentation rate. Series #2: The astronomical target series is the La2004 astronomical solution from 55 Ma to 57 Ma (Laskar et al., 2004). Synthetic Series #3: The target series is the La2004 astronomical solution from 0–2 Ma. Sedimentation rates range from 1 to 30 cm/kyr with a step of 0.2 cm/kyr.

The two-slice periodogram of Synthetic Series #2 shows multiple peaks at 24.0 m, 16.2 m, 8.0 m, 6.1 m, 5.7 m, 5.0 m, 3.8 m, 2.3 m, 1.6 m, 1.4 m, 1.3 m, 1.1 m, 0.92 m, 0.87 m, and 0.74 m. This makes it hard to apply the astronomical cycle ratio method (Weedon, 2003) (Fig. 1E). In the 2-slice correlation coefficient graphs, three peaks are at 4.0 cm/kyr, 6.0 cm/kyr, and ~ 20 cm/kyr (Fig. 3A). The H_0 significance levels at the 4 cm/kyr and 6 cm/kyr are lower than 0.1%, and lower than 5.7% at 20.6 cm/kyr. Note that H_0 significance level is as low as 0.85% at 1.4 cm/kyr, however, the correlation coefficient is only 0.1426 (Fig. 3). All 7 astronomical frequencies are used at 4.0 and 6.0 cm/kyr sedimentation rates (Fig. 4E). This strongly suggests that astronomical forcing paced this “climate” series with sedimentation rates at 4.0 and 6.0 cm/kyr.

When we apply the eCOCO method to Synthetic Series #2, the intervals of constant and variable sedimentation rates can clearly be recognized. From a refined survey using a slightly narrowed sedimentation rate grid (from 2 to 10 cm/kyr with a 0.05 cm/kyr step, running window of 25 m) based on the results of the above COCO analysis, eCOCO is displayed as a sedimentation rate map with respect to stratigraphic position. The estimated sedimentation rate is constant from 0 m to 80 m, then increases from 80 to 130 m, stabilizes from 130 to 190 m, and then shows mi-

nor oscillations to the end of the series (Fig. 4). These estimated sedimentation rates match well with the original modeled sedimentation rate (blue lines in Fig. 4).

3.3. Red and white noise series – Synthetic Series #3

We apply the COCO method to Synthetic Series #3 (Fig. 1C). Synthetic Series #3 merges a red noise series ($\rho_1 = 0.5$, standard deviation = 1) and a white noise series (standard deviation = 0.2) simulating random measurement errors, from 0 to 80 m with a sample rate of 0.04 cm. The estimated ρ results display multiple peaks. However, H_0 significance levels of these peaks are never lower than 0.01, suggesting that the null hypothesis cannot be rejected at the 1% level. That, the Synthetic Series #3 is not influenced by astronomical forcing and no reliable sedimentation rate is available.

4. Application to Phanerozoic paleoclimate series

4.1. Cenozoic: iron series of the PETM-ETM2 interval at ODP Site 1262, Walvis Ridge

ODP Site 1262 from Leg 208 at Walvis Ridge provides a complete record for the Paleogene through the early Eocene from

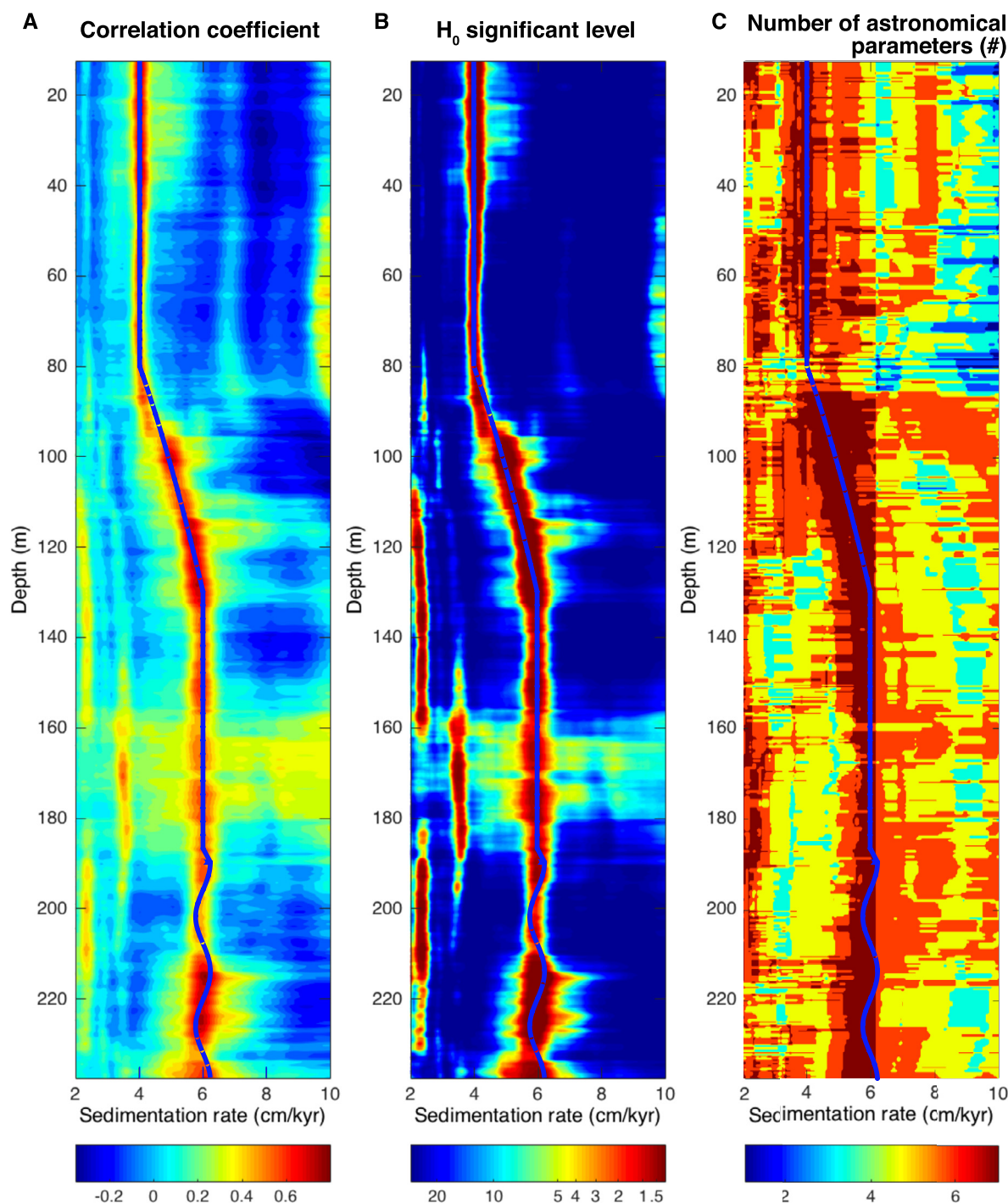


Fig. 4. Refined eCOCO sedimentation rate map of Synthetic Series #2 (Fig. 1B) shown with modeled sedimentation rates (blue lines in Fig. 1B). (A) Evolutionary correlation coefficient. (B) Evolutionary H_0 significance level. (C) Evolutionary map of the number of contributing astronomical parameters. The sliding window size is 25 m; the number of Monte Carlo simulations is 2000. Sedimentation rate from 2 to 10 cm/kyr with a step of 0.05 cm/kyr.

the South Atlantic. Study of this record has enabled an estimation of the duration of the magnetic polarity zones C24r and C25n, and the time of the most prominent Paleogene events, including the Early–Late Paleocene Biotic Event (ELPE), the PETM, and the ETM2. Cyclostratigraphic study by Lourens et al. (2005) on the magnetic susceptibility (MS) and color reflectance (L^* , black/white ratio) series at site 1262 indicated that both the PETM and ETM2 events occurred at the maxima in the 405-kyr and 100-kyr cycles that post-date 2.2 myr eccentricity cycle minima, thus, both events were likely astronomically paced. The subsequent cyclostratigraphic research was conducted by Westerhold et al.

(2007) on the XRF iron dataset and a* color reflectance (red/green ratio). Westerhold et al. (2007, 2012) further refined the chronology for the magnetostratigraphy and biostratigraphy and proposed that the potential astronomical forcing on the thermal maxima events was complex.

The reported sedimentation rates based on astrochronology, magnetostratigraphy, and biostratigraphy are generally consistent with each other. Paleogene pelagic sediments are characterized by moderate sedimentation rates (~ 0.6 – 1.5 cm/kyr), with sedimentation rates up to 1.2 cm/kyr at the PETM interval (Zachos et al., 2004). Assuming each recognized precession cycle lasts 21 kyr, the

resulting sedimentation rates show minor variations throughout the records with a mean value of 1.2 cm/kyr (Westerhold et al., 2007). Meyers (2015) revisited the a^* data from Site 1262, focusing on the interval between the PETM and ETM2 spanning 22.4 m. The independent technique “TimeOpt” suggested a mean sedimentation rate of 1.33 cm/kyr for this interval (Meyers, 2015). As shown below, all these estimates are strongly supported by COCO; the eCOCO sedimentation rate map generally matches with the sedimentation rate estimates of Westerhold et al. (2007, 2012).

The Fe series from 111 m to 170 m at Site 1262 was log-transformed and linearly interpolated to a sampling rate of 0.04 m. The series was detrended via removing a 10-m rloess (Cleveland, 1979; robust version of the local regression using weighted linear least squares and a 2nd degree polynomial model) trend. The AR(1) coefficient of the interpolated and detrended Fe series is 0.679. The AR(1) red noise spectrum was removed from the periodogram of the detrended Fe series. We carried out a COCO analysis using the resulting periodogram of the Fe series. Initial COCO analysis suggests a sedimentation rate of 1.4 cm/kyr with a lower than 1% significance level, with power at all 7 astronomical frequency bands (Fig. 6A and Supplementary Table 1). Then a refined COCO analysis with 2000 Monte Carlo simulations was performed on sedimentation rates from 0.5 to 3 cm/kyr. Three peaks at 0.73 cm/kyr, 0.98 cm/kyr and 1.21 cm/kyr emerge in this COCO analysis (Fig. 6B). All of these three sedimentation rates have significance levels lower than 1% and all 7 astronomical frequencies were used in the estimation.

The eCOCO analysis of ρ , H_0 and the number of contributing astronomical frequencies can be used to test the various sedimentation rate estimates of Westerhold et al. (2007, 2008) and mean sedimentation rate for the PETM-ETM 2 interval of Meyers (2015). Abrupt sedimentation rate shifts from 0.75 to 1.3 cm/kyr at 165 m, and from 1.3 to 1.1 cm/kyr at 163.5 m, are consistent with the two options of Westerhold et al. (2007, 2008). However, a slow increase in sedimentation rates from 1.0 to 1.6 cm/kyr at the 159 m to 156.5 m is not (Fig. 7A). The models of Westerhold et al. (2007, 2008) show a drop in the sedimentation rate from 1.6 to 1.2 cm/kyr at 154 m to 153 m. The sedimentation rates in Option 1 by Westerhold et al. (2008) for the 140 m to 155 m interval is supported by eCOCO.

The PETM interval at Site 1262 is characterized by an abruptly decreased sedimentation rate due to the effect of carbonate dissolution (Bralower et al., 2002; Zachos et al., 2005). The eCOCO results indicate a decrease from 1.1 to 0.6 cm/kyr from 141 m to 139 m at Site 1262. Then the sedimentation rate returned to a relatively constant mean sedimentation rate of 1.33 cm/kyr with minor fluctuations from 139 m to 129 m (Fig. 7). No reliable sedimentation rate from eCOCO is detected from 129 m to 122 m; in comparison, Westerhold et al. (2007, 2008) and Meyers (2015) suggest a relatively constant sedimentation rate at 1.3 cm/kyr. Sedimentation rates of 1.3 to 0.7 cm/kyr are indicated by eCOCO for 122 m to the top of the series. This strongly supports the result of the Option #1 presented by Westerhold et al. (2008).

eCOCO sedimentation rates can be applied for depth-to-time transformation of the Fe series. The time-calibrated Fe series indicates that ELMO (ETM-2) occurred ~ 2.0 Myr after the onset of PETM; this is consistent with the time model of Lourens et al. (2005) but slightly longer than those of Westerhold et al. (2007, 2008) and Meyers (2015). The Fe time series also indicates that both PETM and ELMO occurred during maxima in the 405-kyr and ~ 100 -kyr cycles that post-date very long eccentricity minima (Fig. 8; cf. Lourens et al., 2005), suggesting that, besides volcanism (Gutjahr et al., 2017), astronomical forcing was involved in these events: the extreme seasonal contrast during eccentricity maxima increased ocean temperatures, may have triggered the release of methane hydrates (Lourens et al., 2005).

4.2. Mesozoic: Late Triassic Newark depth-rank series, eastern USA

The continental Newark Basin in eastern North America formed during the breakup of the Pangaea Supercontinent in the Triassic. Over a period of more than 30 Myr, the fluvial and lacustrine Newark Supergroup was deposited in the Newark Basin (Kent et al., 2017). Long-period changes in monsoonal-type rainfall led to variations in water depth in the rifting basins. Consequently, the deposits display pronounced transgressive-regressive cycles as the paleolakes deepened or shallowed. The influence of lake level change on sedimentation rate, which is crucial for understanding the paleoclimate changes and the reconstruction of time scale, remains unclear.

Van Houten (1962) recognized a succession of lithologically distinct cycles in lake facies and estimated that these cycles occurred at 10^4 to 10^5 yr, therefore linked to astronomical cycles. These ‘Van Houten cycles’ have been coded as a depth-rank series of sedimentary facies (Olsen and Kent, 1996) (Fig. 5B). The depth-rank series (0–2000 m) in the Newark Basin is from composited records of the Rutgers, Somerset, Weston, and Martinsville drill cores. The sample rate of the depth-rank series is 0.85 m, this is sufficient to characterize precession cycles considering the mean sedimentation rate of 14–20 cm/kyr (Olsen and Kent, 1996). Power spectra of the depth rank series in the Newark Basin reveal significant wavelengths that correspond to 405 kyr, 125 kyr and 95 kyr eccentricity cycles, 23 kyr and 19 kyr precession cycles (Li et al., 2017; Olsen and Kent, 1996). These enable the astronomical tuning of the magnetic polarity stratigraphy of the Newark Supergroup, thereby forming the basis of the Newark-APTS for the Late Triassic magnetic polarity pattern (Kent et al., 2017). While some correlations to portions of marine magnetostratigraphy remain uncertain (Kent et al., 2017), the Newark-APTS is the fundamental basis for the Late Triassic time scale (Gradstein et al., 2012).

The COCO applied to the whole series indicates a mean sedimentation rate of 15.2 cm/kyr with $\rho = 0.4334$ (Fig. 6C). The null hypothesis (no astronomical forcing) can be rejected at a significance level of less than 0.05%. Other sedimentation rates with a significance level of less than 1% are 3.6 and 4.6 cm/kyr (Fig. 6C). Only at sedimentation rates within the range of 10–30 cm/kyr are all astronomical target frequencies used for the estimation of ρ and H_0 significance level. The COCO analysis strongly supports the view that the sedimentation rates of the Newark depth-rank series of 0–2000 m are generally slowly varying, and range from 13.6 to 15.6 cm/kyr (Fig. 6C). This result is consistent with the results of Olsen and Kent (1996), Kent et al. (2017), and Li et al. (2017).

We can test these previously estimated sedimentation rates for the Newark depth-rank series. eCOCO analysis of the whole Newark series indicates two possible sedimentation rates at 3–5 cm/kyr and 10–18 cm/kyr that yield ρ above 0.3 (Fig. 9B). A decrease in sedimentation rate from 25 to 10 cm/kyr occurs at 1900 m; the evolutionary H_0 significance level map indicates a similar trend of declining sedimentation rates at 1900 m. Two lines of potential sedimentation rate at 3–5 cm/kyr and 10–18 cm/kyr have H_0 significance levels at less than 1% (Fig. 9C). The evolution of contributing astronomical frequencies indicates that only 3 terms are involved for the 3–5 cm/kyr sedimentation rates. In comparison, more than 6 terms are involved at sedimentation rates of 10–18 cm/kyr (Fig. 9D). Considering all aspects together, sedimentation rates of the Newark depth-rank series most likely varied between 10 and 18 cm/kyr, and was probably 21–27 cm/kyr in the 1900 m to 2000 m interval. The evolutionary ρ is shown with published sedimentation rates by Kent et al. (2017) and Li et al. (2017) (Fig. 9A). Compared with the very coarse sedimentation rate curves of these previous studies, the eCOCO sedimentation rates are generally consistent and have a much higher resolution.

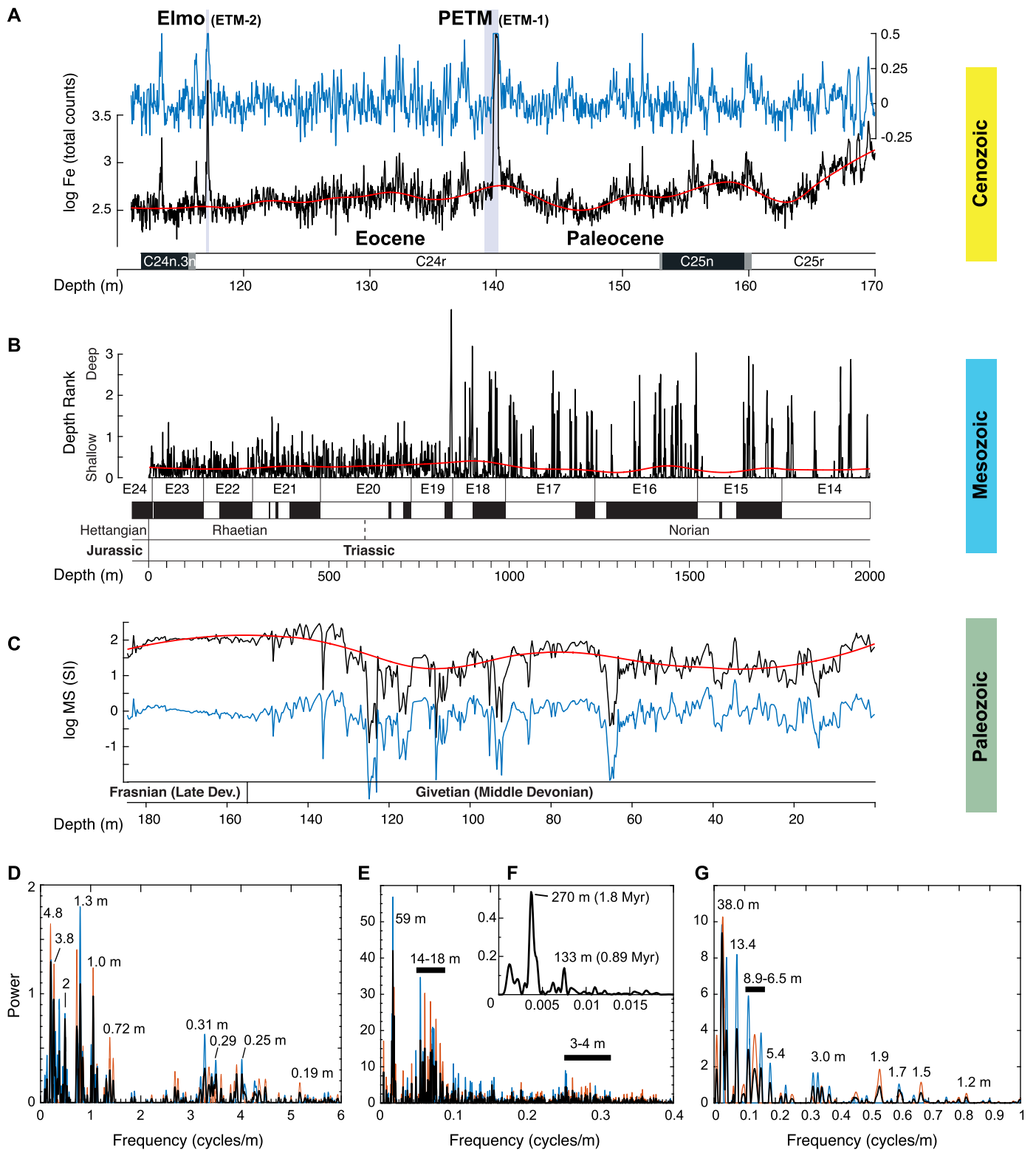


Fig. 5. Phanerozoic paleoclimate series. (A) Log-transformed Fe series of ODP site 1262 (black) with a 10-m “rloess” trend (red) and detrended series (blue). Data are from Westerhold et al. (2007, 2008). (B) Depth rank series (black) of the Newark Supergroup (Olsen and Kent, 1996) with a 500-m “rloess” trend computed with MATLAB’s *smooth.m* (red). Magnetic polarity zones are from Kent and Olsen (1999). (C) Log-transformed MS series (black) at the La Thure section (De Vleeschouwer et al., 2015) and detrended series (blue) after removing its 80 m “rloess” trend (red). (D) 2-slice periodograms of detrended Fe series in (A). (E) 2-slice periodograms of the detrended depth-rank series in (B). (F) Periodogram of the Gaussian low-pass filtered depth-rank series (Fig. 8A) after removing third order polynomial trend (cutoff frequency is 0.01 m^{-1}). (G) 2-slice periodograms of detrended MS series in (C). All detrended series have removed AR(1) models. Thin blue and red lines are periodograms of first and second half slices of the detrended MS series. The thick black line is the mean of periodograms of each slice.

The eCOCO results also reveal recurrent discontinuities in sedimentation rate that coincide with lake level falls with a periodicity of $\sim 270 \text{ m}$. This 270-m recurrence cycle also dominates the low-

pass filtered depth-rank series indicative of a long-term lake level cycle (Fig. 5F). Given a mean sedimentation rate of 15.2 cm/kyr (see above), the 270 m cycle represents a 1.78 Myr periodicity,

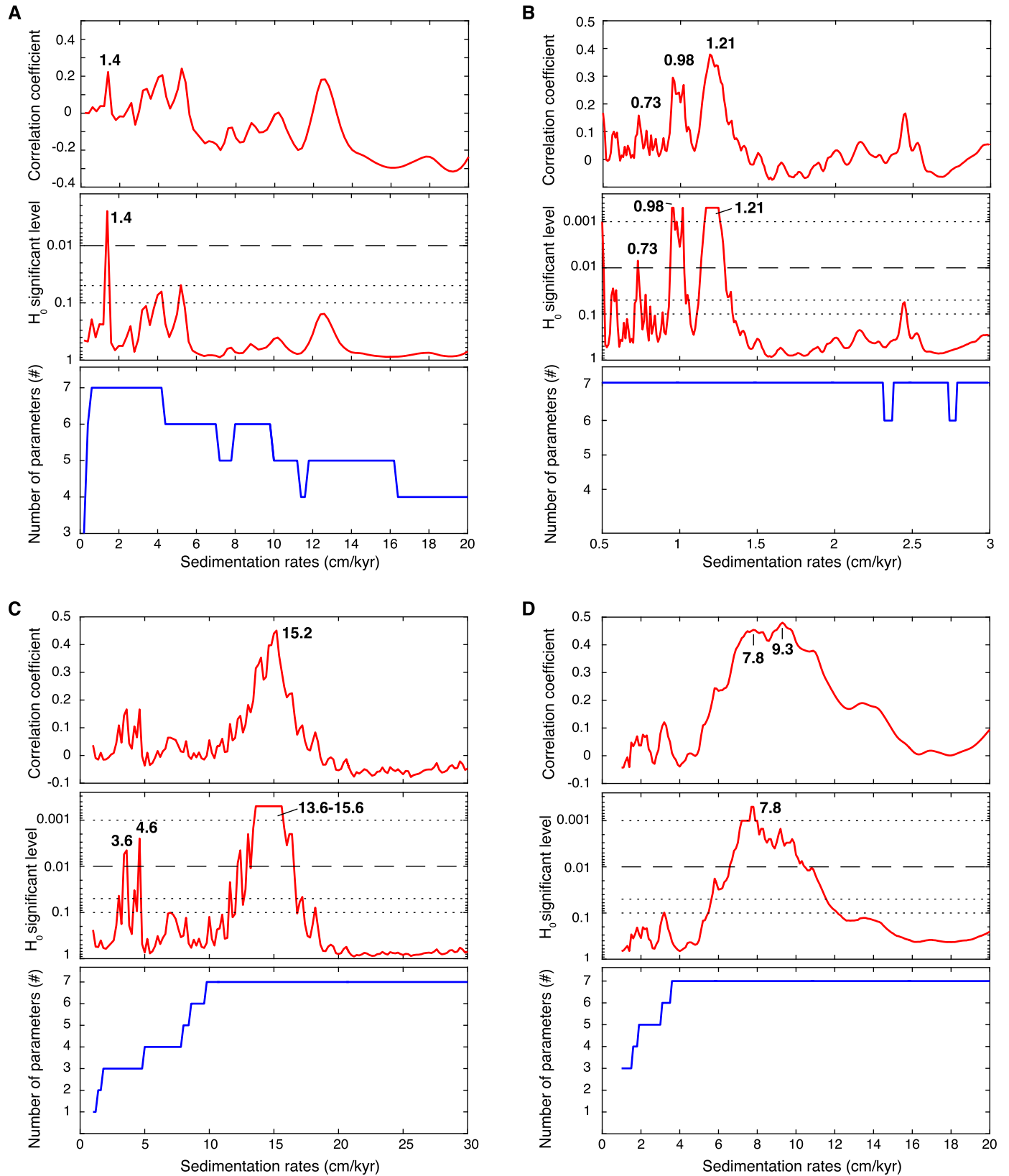


Fig. 6. COCO analysis of the Phanerozoic paleoclimate series. **(A–B)** The initial **(A)** and refined **(B)** COCO analysis of the Fe series at ODP Site 1262 and target series (La2004 solution from 55 Ma to 57 Ma). **(A)** is initial test of sedimentation rates ranging from 0.2 to 20 cm/kyr with a step of 0.2 cm/kyr; and **(B)** is refined test focusing on the sedimentation rates from 0.5 to 3 cm/kyr with a step of 0.01 cm/kyr. **(C)** The 2-slice COCO spectra of the Triassic Newark depth-rank series and astronomical target series (La2004 solution from 202 Ma to 204 Ma). Sedimentation rates range from 1 to 30 cm/kyr with a step of 0.2 cm/kyr. **(D)** The 2-slice COCO spectra of the Devonian MS series at the La Thure and target series using Berger94 solution at 384 Ma (Berger and Loutre, 1994). Sedimentation rates range from 1 to 20 cm/kyr with a step of 0.1 cm/kyr. From top to bottom in each panel: the correlation coefficient spectrum; null hypothesis test, and the number of contributing astronomical frequencies. The number of Monte Carlo simulations is 2000.

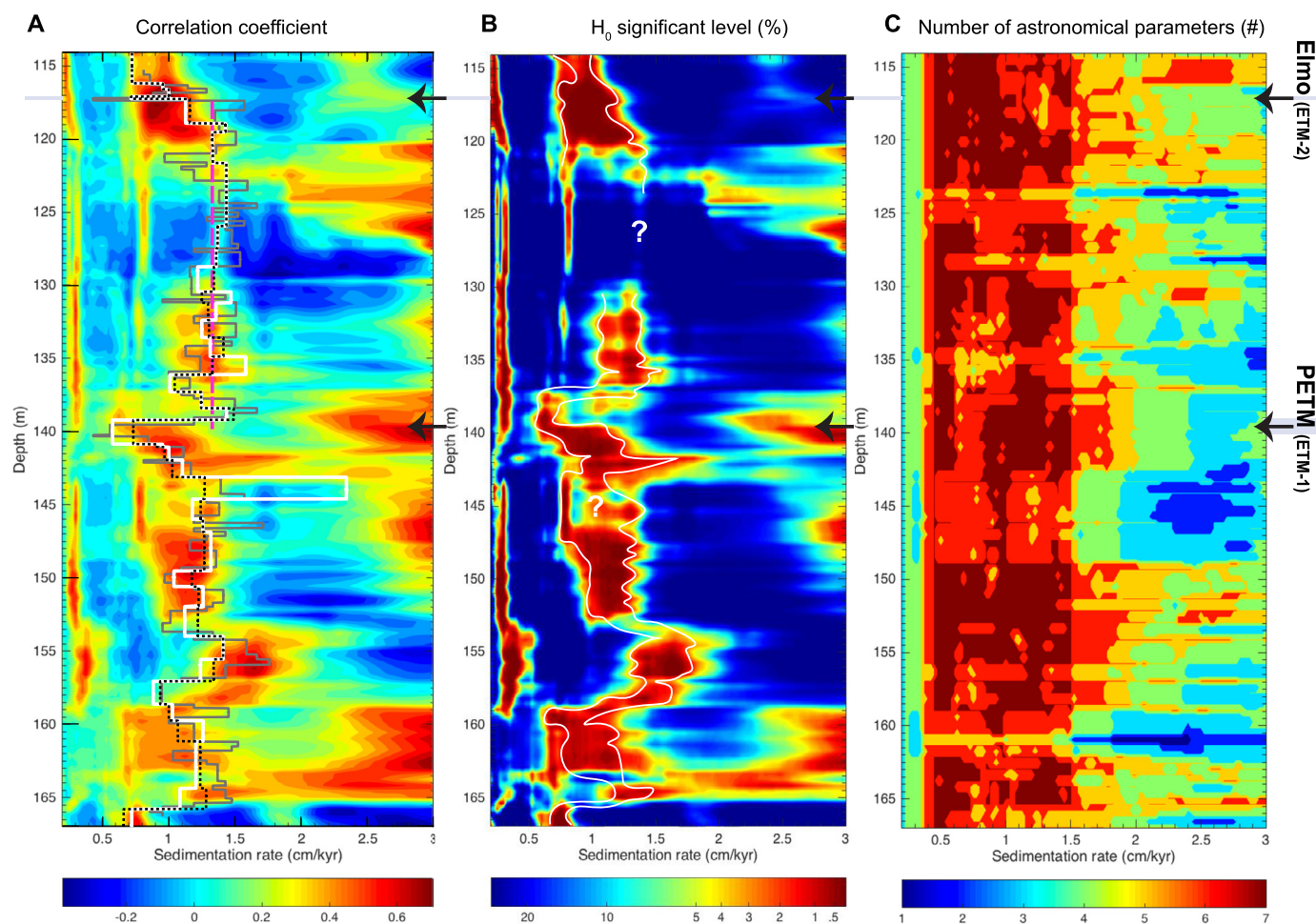


Fig. 7. eCOCO sedimentation rate map of the Fe series at ODP Leg 208 Site 1262. (A) Evolutionary ρ shown with published sedimentation rate curves of Westerhold et al. (2007) (grey line) and Westerhold et al. (2008) (dotted black – Option 1; white – Option 2), and Meyers (2015) (dashed pink line). (B) Evolutionary H_0 significance level. The area bounded by white lines shows potential sedimentation rates. 122 m to 129 m interval designated with a white “?” has no solution. (C) Evolution of the number of contributing astronomical frequencies. The sliding window size is 5 m; the sliding window step is 0.4 m. The number of Monte Carlo simulations is 2000. Sedimentation rates range from 0.2 to 3.0 cm/kyr with a step of 0.01 cm/kyr.

which is comparable to a previously estimated ~ 1.75 Myr lake level cycle in the Newark Basin (Kent et al., 2017, and references within). The repeated discontinuities in the eCOCO map (Fig. 9B–C) suggest decreased signal-to-noise ratios linked to increased depositional environmental instability and even short-lived erosion during these large lake level falls (cf. Li et al., 2018b). Newark basin lakes experienced a super monsoonal climate due to the Pangaea supercontinent, and the most intense rainy seasons and deepest lakes occurred when precession cycles are configured with perihelion in Northern Hemisphere summer during times of highest eccentricity. The weakest rainy seasons and shallowest lakes occurred when the precession cycle is configured with perihelion during Southern Hemisphere summer during times of lowest eccentricity (Olsen and Kent, 1996). Therefore, eCOCO analysis help understand the driving forcing of sedimentation rate and depositional environmental changes during the Late Triassic.

4.3. Paleozoic: Devonian magnetic susceptibility series from Belgium

Paleozoic cyclostratigraphy is the next frontier in astrochronology (Hinnov, 2013). Here we revisit a 184 m thick Givetian–early Frasnian (~ 384 Ma, Middle–Late Devonian) magnetic susceptibility (MS) series from the La Thure section, Dinant Synclinorium, southern Belgium (De Vleeschouwer et al., 2015; Martinez et al., 2016). The section is dominated by limestone and shales. The boundary

of the Givetian–Frasnian is defined by the first occurrence of conodont *Ancyrodella rotundiloba* and at $155 \text{ m} \pm 2 \text{ m}$ at the La Thure section (De Vleeschouwer et al., 2015). The MS series carries a primary depositional signal related to terrestrial input (Pas et al., 2017). De Vleeschouwer et al. (2015) presented a detailed study of the MS series using cyclostratigraphic methods, recognizing a total of 6.5 long orbital eccentricity cycles in the series, suggesting a mean sedimentation rate of 7.0 cm/kyr.

We apply COCO analysis on the MS series. The MS data were log-transformed and interpolated to a 0.3 m sampling rate, and an 80-m ‘loess’ trend was removed (Fig. 5C). The periodogram of this series is consistent with those of independent studies by De Vleeschouwer et al. (2015) and Martinez et al. (2016) (Fig. 5F). The La04 and La10 astronomical solutions are restricted to the last 250 Ma; instead the Berger94 solution (Berger and Loutre, 1994) for the new seven astronomical frequencies is used. Linear interpolation at 384 Ma of the Berger94 solution indicates seven astronomical terms: 413, 123, 95 kyr orbital eccentricity cycles, 39.3 and 31.9 kyr obliquity cycles and 19.8 and 16.8 kyr precession index cycles. Two-slice COCO analysis indicates a broad maximum in estimated ρ centered at 8 cm/kyr (Fig. 6D). 2000 Monte Carlo simulations of the null hypothesis test indicates that a wide range of sedimentation rates from 6.6–10.4 cm/kyr exhibits a lower than 1% significance level, and 7.8 cm/kyr lower than 0.1%; thus, the null hypothesis of no astronomical signal can be rejected at a 99.9%

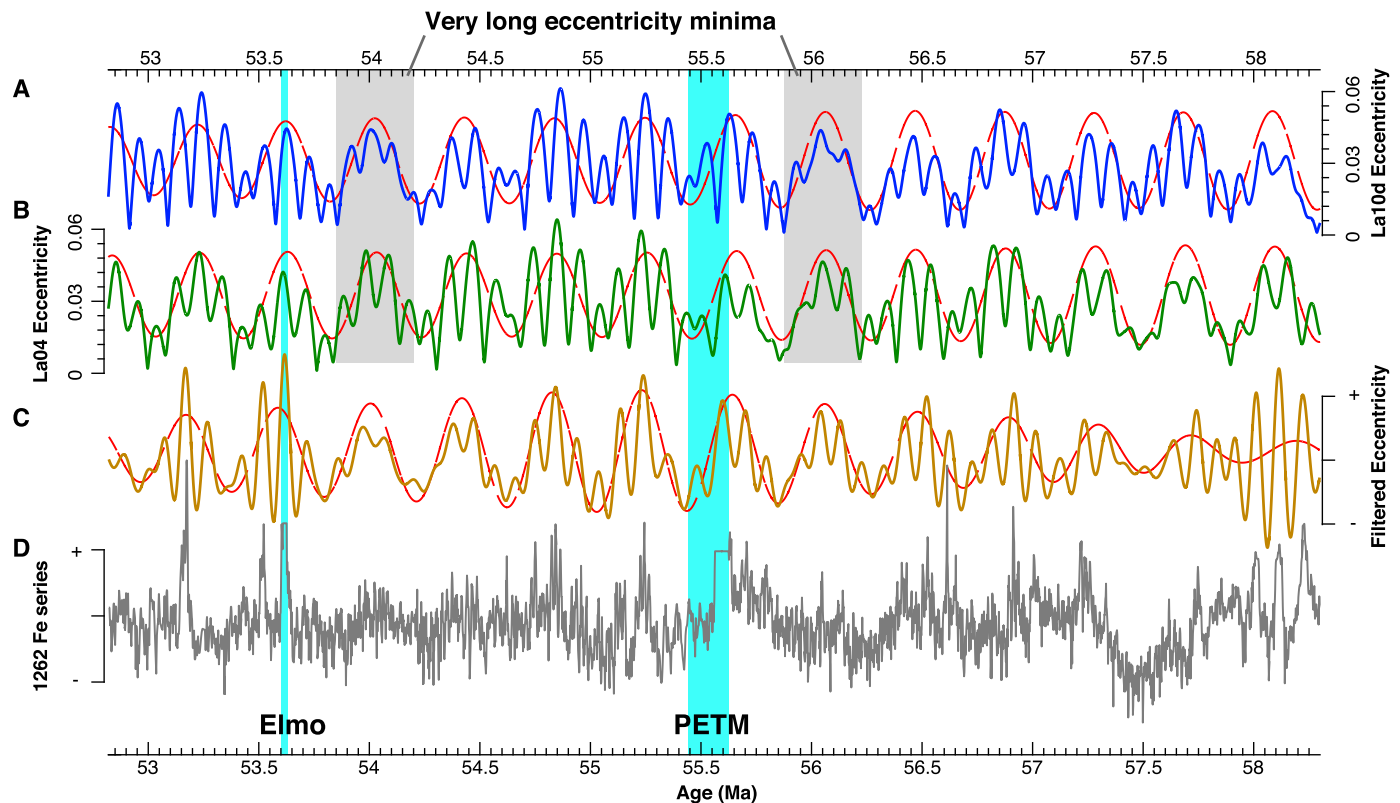


Fig. 8. Time-calibrated ODP Site 1262 Fe series and orbital eccentricity cycles. The Fe series is anchored to La10d solution (Option 1 in Westerhold et al., 2012). Orbital eccentricity solutions of (A) La10d (Laskar et al., 2011) and (B) La04 (Laskar et al., 2004) with filtered 405-kyr cycles (red dashed, Gaussian filter with a frequency of 0.00248 ± 0.0028 cycles/kyr). (C) 405 kyr cycles (red dashed line) and merged 405-kyr and ~ 100 kyr cycles (orange line, Gaussian filter with a frequency of 0.0098 ± 0.00266 cycles/kyr) of (D) the tuned Fe series at Site 1262.

confidence level at 7.8 cm/kyr, with all astronomical frequencies contributing (Fig. 6D).

eCOCO analysis of the La Thure MS series links sedimentation rate to depositional environment (Fig. 10). eCOCO indicates that sedimentation rates range from 6.5 to 10 cm/kyr for 0 m to 65 m, increases up to 13 cm/kyr for 70 m to 100 m, then 6 to 9 cm/kyr for 100 m to 150 m, and slightly increases at the top of the section. The highest sedimentation rate occurs close to the reef of the rimmed shelf, which produces carbonate (Fig. 10A; Pas et al., 2017). The change in sedimentation rate is discontinuous at ~ 100 m indicating a brief gap and a sea level fall; this is consistent with an abrupt facies shift recognized by Pas et al. (2017). The existence of the brief gap has been hinted: filtered 405 kyr cycles in Fig. 2 of De Vleeschouwer et al. (2015) within 66 m to 92 m contains only three 100 kyr cycles. The eCOCO results indicate that sedimentation rates were paced by 405-kyr orbital eccentricity cycles. Peaks in the filtered 405 kyr cycles indicate “ephemeral” (temporary) and sudden changes in sedimentation rate at ~ 50 m, 85 m, 140 m, and the top of the MS series.

5. Discussion

Numerous time-calibration techniques for cyclostratigraphy have been proposed in the literature (see e.g. Hinnov, 2013). The provisional time scale approach takes advantage of available radioisotope dating, magnetic polarity patterns, biostratigraphy and chemostratigraphy (Kuiper et al., 2008; Li et al., 2016b, 2018a; Zhang et al., 2015). The second type of time-calibration matches proxy data to the astronomical target series, i.e., dynamic optimization (Yu and Ding, 1998) and dynamic time warping (Lin et al., 2014; Lisiecki and Lisiecki, 2002). In the classical astronomical “minimal tuning” method (Li et al., 2016b; Muller and MacDonald,

2000; Zhang et al., 2015), appropriate Fourier approaches are applied to transfer data from the stratigraphic domain to the time domain by tracking single, dominating frequencies. The sedimentary wavelengths above a certain noise model level are multiplied by a sedimentation rate and matched with predicted astronomical periods via ratios among the frequencies. The best-matched sedimentation rate is selected to construct an astronomical time scale for the stratigraphic series. Tuning of the series to one astronomical frequency can be used to evaluate the success or failure of the tuning to realign other astronomical cycles (Muller and MacDonald, 2000). “Depth-derived” time scales, with additional age constraints, provide a direct test of the astronomical hypothesis (Huybers and Wunsch, 2004).

Without radioisotopic and other time constraints, three recent astronomical testing categories exist; all involve the problem of finding the variation in sedimentation rate that matches sedimentary cycle wavelengths to astronomical periodicities. The first category evaluates the frequency and amplitude modulations that are inherent in the precession index and obliquity cycles (Hinnov, 2000; Zeeden et al., 2015; Boulila et al., 2018). The second category of statistical astronomical testing takes advantage of the bedding hierarchies relationships (ratios of cycles), including the average spectral misfit (ASM) (Meyers and Sageman, 2007) and Bayesian Monte Carlo (Malinverno et al., 2010) approaches. The third category is the inverse approach of time scale optimization that evaluates eccentricity-related amplitude modulation and bundling combining both astronomical amplitude and frequency modulation and bedding hierarchies (Meyers, 2015).

Our technique falls into the second category of statistical astronomical testing that seeks to evaluate frequency ratios as predicted in astronomical solutions. Both ASM and Bayesian Monte Carlo approaches provide statistics on the evaluated sedimentation

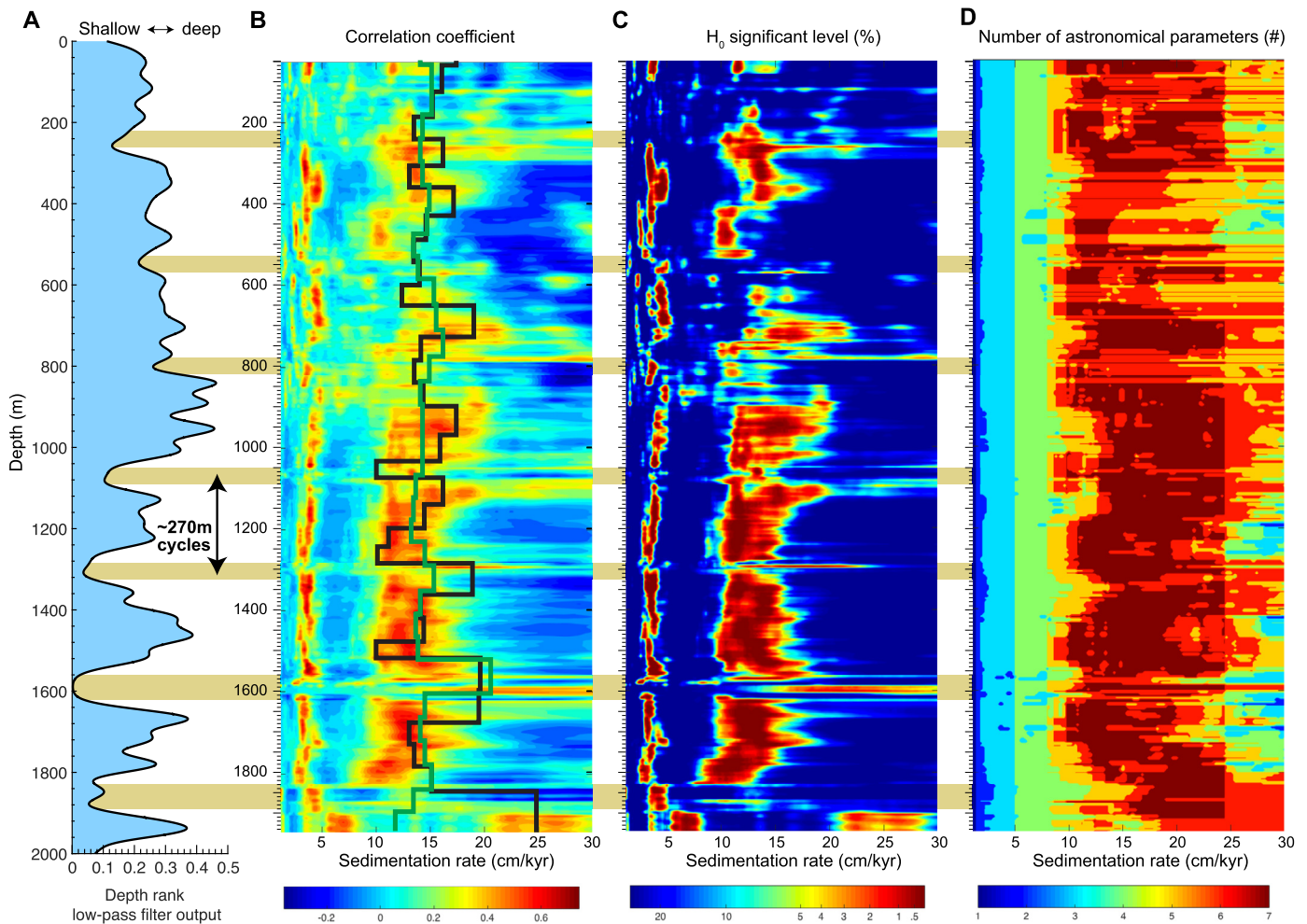


Fig. 9. eCOCO analysis of the Late Triassic Newark depth-rank series (0–2000 m). (A) Gaussian low-pass filter output of the depth rank series (cutoff frequency is 0.01 m^{-1}) indicative of latest Triassic lake levels in the Newark Basin shown with $\sim 270 \text{ m}$ cycles (gold horizontal bars). (B) Evolutionary ρ map shown with published sedimentation rate curves by Kent et al. (2017) (black line) and Li et al. (2017) (green line). (C) Evolutionary H_0 significance level map. (D) An evolutionary map of the number of contributing astronomical parameters. The sliding window size is 100 m; the step is 5.1 m. All periodograms were analyzed with AR(1) models removed. The number of Monte Carlo simulations is 2000. Sedimentation rates range from 1 to 30 cm/kyr with a step of 0.2 cm/kyr.

rates; the ASM approach also evaluates the null hypothesis of astronomical forcing. Therefore, both ASM and Bayesian Monte Carlo approaches address similar questions with the COCO technique.

These three measurements of fit are not identical. The ASM evaluates the difference between target astronomical frequencies and the frequencies of spectral peaks in the observed data (Meyers and Sageman, 2007); the Bayesian Monte Carlo approach is based on the likelihood of astronomical signals in the periodogram of the measured data (Malinverno et al., 2010); and the COCO method uses the correlation coefficient between the power spectra of a proxy series and an astronomical solution. Generally speaking, the appropriate sedimentation rate leads to low ASM value and lower H_0 significance level in the ASM estimation and higher likelihood in the Bayesian Monte Carlo approach. In comparison, it results in a high correlation coefficient, lower H_0 significance levels, and generally larger number of contributing orbital parameters in the COCO estimation.

Both the ASM and COCO methods yield H_0 significance level, but they are not identical. In the ASM, an indicator of the rejection or acceptance of the null hypothesis is called the critical significance level, which is the inverse of the number of tested sedimentation rates (Meyers and Sageman, 2007). By comparison, our H_0 significance level can be used directly, i.e., the null hypothesis (no orbital forcing) may be rejected if the H_0 significance level

in the COCO estimation is lower than 1%, which suggests the confidence level of astronomical forcing is higher than 99%.

6. Conclusions

We have presented a quantitative technique that involves estimating correlation coefficients (COCO) between the periodograms of an astronomical forcing target and paleoclimate series allowing for a variable relationship between time and sedimentation rate. The number of contributing orbital parameters in the estimation of the correlation coefficient is evaluated at each tested sedimentation rate. The hypothesis that astronomical forcing has an impact on the paleoclimate series is tested against a null hypothesis (H_0) of no astronomical forcing. The null distribution is established via a Monte Carlo approach that involves generating surrogate correlation coefficients between the power spectrum of the target and spectra constructed from random frequencies with random spectral amplitudes. The null hypothesis is rejected if the H_0 significance level is lower than 1% ($p < 0.01$) as estimated from the null distribution.

eCOCO analysis performs this procedure with a sliding window to track the variable sedimentation rate, yielding evolutionary (i.e. time-evolving) estimates of the correlation coefficient ρ , H_0 significance level, and the number of contributing astronomical frequencies. eCOCO analysis successfully tracks modeled sedimentation

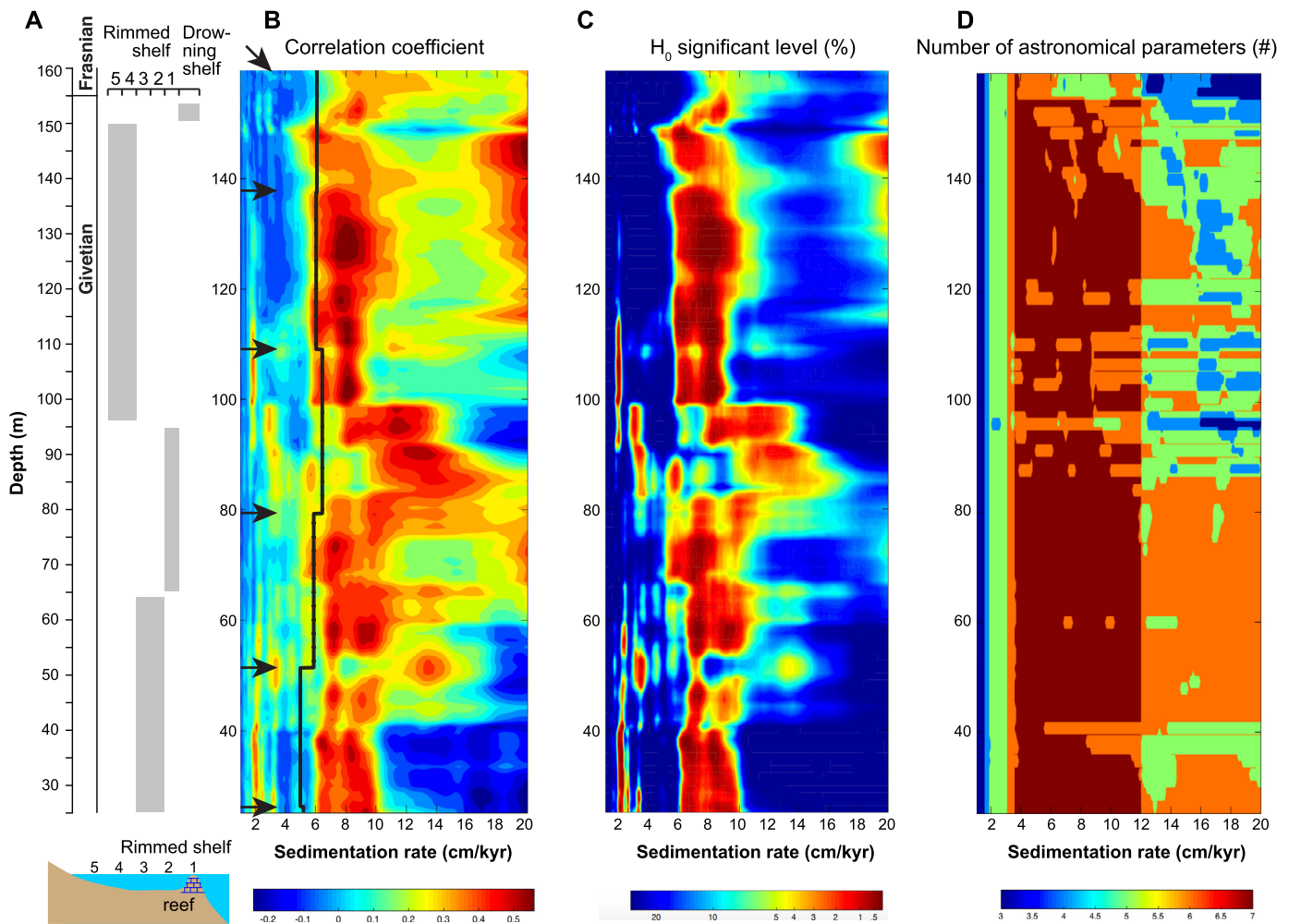


Fig. 10. eCOCO spectra of the log-transformed and detrended La Thure MS series shown with main facies at the La Thure section. **(A)** Main facies of the La Thure section indicative of depositional environments modified from Pas et al. (2017). **(B)** Evolutionary correlation coefficient sedimentation rate map estimated from filtered long-eccentricity peaks in De Vleeschouwer et al. (2015) (see their Fig. 2). Black arrows indicate long-eccentricity peaks in De Vleeschouwer et al. (2015) that interpret changes in sedimentation rates. **(C)** The evolutionary map of the H_0 significance level. **(D)** The evolutionary map of the number of contributing astronomical parameters. The sliding window size is 50 m; the sliding step is 1.2 m. The number of Monte Carlo simulations is 2000. Sedimentation rates range from 1 to 20 cm/kyr with a step of 0.1 cm/kyr.

rates in two synthetic series with constant and variable sedimentation rates. A representative synthetic noise series, by contrast, fails to detect an astronomical signal, with H_0 significance levels at each tested sedimentation rates larger than 1%.

COCO and eCOCO analysis is applied to three Phanerozoic paleoclimate series, including the Paleocene–Eocene Fe series at ODP Leg 208 Site 1262, the Late Triassic depth-rank series in the Newark basin of North America, and the Middle–Late Devonian MS series of the La Thure section, Belgium. The analysis verifies previously established sedimentation rate estimates, while providing new insights into depositional environment changes. In certain instances, our approach reveals previously unidentified changes in sedimentation rate. In summary, COCO and eCOCO analysis is a powerful tool for the evaluation of astronomical forcing of paleoclimate series and sedimentation rate variations. This approach offers new prospects for improving the reproducibility of cyclostratigraphic estimates and improving geological age models throughout the Phanerozoic.

Data availability

The Fe series at ODP Site 1262 is online at <https://doi.org/10.1594/PANGAEA.603177> and <https://doi.org/10.1594/PANGAEA.667122>. The Late Triassic Newark depth-rank series is online at

www.ldeo.columbia.edu/~polsen/nbcp/data.html. The Middle–Late Devonian magnetic susceptibility series at the La Thure section is available at <https://doi.pangaea.de/10.1594/PANGAEA.855764>.

Code availability

The code to generate correlation coefficient and evolutionary correlation coefficient spectra is available in the software *ACycle* v 0.1.3, available at <https://github.com/mingsongli/acycle>.

Acknowledgements

This research was funded by Heising-Simons Foundation (2016–11). We thank Mathieu Martinez and one anonymous reviewer for their constructive comments. We gratefully acknowledge suggestions from Richard Zeebe. The authors thank Thomas Westerhold, Ursula Röhl, Paul Olsen, David De Vleeschouwer, and Damien Pas for open-sourcing the paleoclimate series. This is a contribution to the IGCP Project 630 and 652.

Appendix A. Supplementary material

Supplementary material related to this article can be found online at <https://doi.org/10.1016/j.epsl.2018.08.041>.

References

- Berger, A., Loutre, M.-F., Laskar, J., 1992. Stability of the astronomical frequencies over the Earth's history for paleoclimate studies. *Science* 255, 560–566.
- Berger, A., Loutre, M.F., 1994. Astronomical forcing through geological time. In: De Boer, P.L., Smith, D.G. (Eds.), *Orbital Forcing and Cyclic Sequences*. In: IAS Spec. Publ., pp. 15–24.
- Bouhila, S., et al., 2018. Towards a robust and consistent middle Eocene astronomical timescale. *Earth Planet. Sci. Lett.* 486, 94–107.
- Bralower, T.J., Silva, I.P., Malone, M.J., 2002. New evidence for abrupt climate change in the Cretaceous and Paleogene: an Ocean Drilling Program expedition to Shatsky Rise, northwest Pacific. *GSA Today* 12, 4–10.
- Cleveland, W.S., 1979. Robust locally weighted regression and smoothing scatterplots. *J. Am. Stat. Assoc.* 74, 829–836.
- De Vleeschouwer, D., Boulvain, F., Da Silva, A.-C., Pas, D., Labaye, C., Claeys, P., 2015. The astronomical calibration of the Givetian (Middle Devonian) timescale (Dinant Synclinorium, Belgium). *Geol. Soc. (Lond.) Spec. Publ.* 414, 245–256.
- Gradstein, F., Ogg, J., Schmitz, M., Ogg, G., 2012. *The Geological Time Scale 2012*. Elsevier, 1144 p.
- Gutjahr, M., Ridgwell, A., Sexton, P.F., Anagnostou, E., Pearson, P.N., Pälike, H., Norris, R.D., Thomas, E., Foster, G.L., 2017. Very large release of mostly volcanic carbon during the Palaeocene–Eocene Thermal Maximum. *Nature* 548, 573–577.
- Hinnov, L., 2000. New perspectives on orbitally forced stratigraphy. *Annu. Rev. Earth Planet. Sci.* 28, 419–475.
- Hinnov, L., Hilgen, F.J., 2012. Cyclostratigraphy and astrochronology. In: Gradstein, F., Ogg, J., Schmitz, M., Ogg, G. (Eds.), *The Geologic Time Scale 2012*. Elsevier, pp. 63–83.
- Hinnov, L.A., 2013. Cyclostratigraphy and its revolutionizing applications in the Earth and planetary sciences. *Geol. Soc. Am. Bull.* 125, 1703–1734.
- Husson, D., 2014. MathWorks file exchange: RedNoise_ConfidenceLevels. http://www.mathworks.com/matlabcentral/fileexchange/45539-rednoise-confidencelevels/content/RedNoise_ConfidenceLevels/RedConf.m.
- Huybers, P., Wunsch, C., 2004. A depth-derived Pleistocene age model: uncertainty estimates, sedimentation variability, and nonlinear climate change. *Paleoceanography* 19, PA1028. <https://doi.org/10.1029/2002PA000857>.
- Kemp, D.B., 2016. Optimizing significance testing of astronomical forcing in cyclostratigraphy. *Paleoceanography* 31, 1516–1531.
- Kent, D.V., Olsen, P.E., 1999. Astronomically tuned geomagnetic polarity timescale for the Late Triassic. *J. Geophys. Res.* 104, 12831–12841.
- Kent, D.V., Olsen, P.E., Muttoni, G., 2017. Astrochronostratigraphic Polarity Time Scale (APTS) for the Late Triassic and Early Jurassic from continental sediments and correlation with standard marine stages. *Earth-Sci. Rev.* 166, 153–180.
- Kuiper, K.F., Deino, A., Hilgen, F.J., Krijgsman, W., Renne, P.R., Wijbrans, J.R., 2008. Synchronizing rock clocks of Earth history. *Science* 320, 500–504.
- Laskar, J., Fienga, A., Gastineau, M., Manche, H., 2011. La2010: a new orbital solution for the long-term motion of the Earth. *Astron. Astrophys.* 532, A89. <https://doi.org/10.1051/0004-6361/201116836>.
- Laskar, J., Robutel, P., Joutel, F., Gastineau, M., Correia, A.C.M., Levrard, B., 2004. A long-term numerical solution for the insolation quantities of the Earth. *Astron. Astrophys.* 428, 261–285.
- Li, M., Huang, C., Hinnov, L., Chen, W., Ogg, J., Tian, W., 2018a. Astrochronology of the Anisian stage (Middle Triassic) at the Guandao reference section, South China. *Earth Planet. Sci. Lett.* 482, 591–606.
- Li, M., Huang, C., Hinnov, L., Ogg, J., Chen, Z.-Q., Zhang, Y., 2016a. Obliquity-forced climate during the Early Triassic hothouse in China. *Geology* 44, 623–626.
- Li, M., Hinnov, L.A., Huang, C., Ogg, J.G., 2018b. Sedimentary noise and sea levels linked to land–ocean water exchange and obliquity forcing. *Nat. Commun.* 9, 1004. <https://doi.org/10.1038/s41467-018-03454-y>.
- Li, M., Ogg, J., Zhang, Y., Huang, C., Hinnov, L., Chen, Z.-Q., Zou, Z., 2016b. Astronomical-cycle scaling of the end-Permian extinction and the Early Triassic Epoch of South China and Germany. *Earth Planet. Sci. Lett.* 441, 10–25.
- Li, M., Zhang, Y., Huang, C., Ogg, J., Hinnov, L., Wang, Y., Zou, Z., Li, L., 2017. Astronomical tuning and magnetostratigraphy of the Upper Triassic Xujiahe Formation of South China and Newark Supergroup of North America: implications for the Late Triassic time scale. *Earth Planet. Sci. Lett.* 475, 207–223.
- Lin, L., Khider, D., Lisiecki, L.E., Lawrence, C.E., 2014. Probabilistic sequence alignment of stratigraphic records. *Paleoceanography* 29, 976–989.
- Lisiecki, L.E., Lisiecki, P.A., 2002. Application of dynamic programming to the correlation of paleoclimate records. *Paleoceanography* 17, 1–12.
- Lourens, L.J., Sluijs, A., Kroon, D., Zachos, J.C., Thomas, E., Rohl, U., Bowles, J., Raffi, I., 2005. Astronomical pacing of late Palaeocene to early Eocene global warming events. *Nature* 435, 1083–1087.
- Malinverno, A., Erba, E., Herbert, T.D., 2010. Orbital tuning as an inverse problem: chronology of the early Aptian oceanic anoxic event 1a (Selli Level) in the Cismont APFICORE. *Paleoceanography* 25, PA2203. <https://doi.org/10.1029/2009PA001769>.
- Mann, M.E., Lees, J.M., 1996. Robust estimation of background noise and signal detection in climatic time series. *Clim. Change* 33, 409–445.
- Martinez, M., Kotov, S., De Vleeschouwer, D., Pas, D., Pälike, H., 2016. Testing the impact of stratigraphic uncertainty on spectral analyses of sedimentary series. *Clim. Past* 12, 1765–1783.
- Meyers, S.R., 2015. The evaluation of eccentricity-related amplitude modulation and bundling in paleoclimate data: an inverse approach for astrochronologic testing and time scale optimization. *Paleoceanography* 30. <https://doi.org/10.1002/2015PA002850>.
- Meyers, S.R., 2012. Seeing red in cyclic stratigraphy: spectral noise estimation for astrochronology. *Paleoceanography* 27, PA3228. <https://doi.org/10.1029/2012PA002307>.
- Meyers, S.R., Sageman, B.B., 2007. Quantification of deep-time orbital forcing by average spectral misfit. *Am. J. Sci.* 307, 773–792.
- Mudelsee, M., 2014. *Climate Time Series Analysis—Classical Statistical and Bootstrap Methods*. Springer Verlag, Cham, 454 p.
- Muller, R.A., MacDonald, G.J., 2000. *Ice Ages and Astronomical Causes: Data, Spectral Analysis, and Mechanisms*. Springer-Praxis, London, 318 p.
- Olsen, P.E., Kent, D.V., 1996. Milankovitch climate forcing in the tropics of Pangaea during the Late Triassic. *Palaeogeogr. Palaeoclimatol. Palaeoecol.* 122, 1–26.
- Pas, D., Da Silva, A.-C., Devleeschouwer, X., De Vleeschouwer, D., Cornet, P., Labaye, C., Boulvain, F., 2017. Insights into a million-year-scale Rhenohercynian carbonate platform evolution through a multi-disciplinary approach: example of a Givetian carbonate record from Belgium. *Geol. Mag.* 154, 707–739.
- Ravelo, A.C., Andreasen, D.H., Lyle, M., Olivarez Lyle, A., Wara, M.W., 2004. Regional climate shifts caused by gradual global cooling in the Pliocene epoch. *Nature* 429, 263–267.
- Sinnaesael, M., et al., 2016. Astronomical component estimation (ACE v.1) by time-variant sinusoidal modeling. *Geosci. Model Dev.* 9, 3517–3531.
- Thomson, D.J., 1982. Spectrum estimation and harmonic analysis. *Proc. IEEE* 70, 1055–1096.
- Van Houten, F.B., 1962. Cyclic sedimentation and the origin of analcime-rich Upper Triassic Lockatong Formation, west-central New Jersey and adjacent Pennsylvania. *Am. J. Sci.* 260, 561–576.
- Weedon, G.P., 2003. *Time Series Analysis and Cyclostratigraphy: Examining Stratigraphic Records of Environmental Cycles*. Cambridge University Press.
- Westerhold, T., Röhl, U., Laskar, J., 2012. Time scale controversy: accurate orbital calibration of the early Paleogene. *Geochem. Geophys. Geosyst.* 13, Q06015. <https://doi.org/10.1029/2012GC004096>.
- Westerhold, T., Röhl, U., Laskar, J., Raffi, I., Bowles, J., Lourens, L.J., Zachos, J.C., 2007. On the duration of magnetochrons C24r and C25n and the timing of early Eocene global warming events: implications for the Ocean Drilling Program Leg 208 Walvis Ridge depth transect. *Paleoceanography* 22, PA2201. <https://doi.org/10.1029/2006PA001322>.
- Westerhold, T., Röhl, U., Raffi, I., Fornaciari, E., Monechi, S., Reale, V., Bowles, J., Evans, H.F., 2008. Astronomical calibration of the Paleocene time. *Palaeogeogr. Palaeoclimatol. Palaeoecol.* 257, 377–403.
- Yu, Z.W., Ding, Z.L., 1998. An automatic orbital tuning method for paleoclimate records. *Geophys. Res. Lett.* 25, 4525–4528.
- Zachos, J.C., Kroon, D., Blum, P., et al., 2004. Proc. ODP, Init. Repts. 208. College Station, TX (Ocean Drilling Program). <https://doi.org/10.2973/odp.proc.ir.208.2004>.
- Zachos, J.C., Röhl, U., Schellenberg, S.A., Sluijs, A., Hodell, D.A., Kelly, D.C., Thomas, E., Nicolo, M., Raffi, I., Lourens, L.J., 2005. Rapid acidification of the ocean during the Paleocene–Eocene thermal maximum. *Science* 308, 1611–1615.
- Zeeden, C., Meyers, S.R., Lourens, L.J., Hilgen, F.J., 2015. Testing astronomically tuned age models. *Paleoceanography* 30, 369–383. <https://doi.org/10.1002/2014PA002762>.
- Zhang, Y., Li, M., Ogg, J.G., Montgomery, P., Huang, C., Chen, Z.-Q., Shi, Z., Enos, P., Lehmann, D.J., 2015. Cycle-calibrated magnetostratigraphy of middle Carnian from South China: implications for Late Triassic time scale and termination of the Yangtze Platform. *Palaeogeogr. Palaeoclimatol. Palaeoecol.* 436, 135–166.